2019

Optical Sensing of Structural Dynamics in Complex Media

Jose Rafael Guzman Sepulveda
University of Central Florida

OPTICAL SENSING OF STRUCTURAL DYNAMICS IN COMPLEX MEDIA

by

JOSE RAFAEL GUZMAN SEPULVEDA

B. Sc. University of Guanajuato, 2010
M.Sc. Autonomous University of Tamaulipas, 2013
M.Sc. University of Central Florida, 2016

A dissertation submitted in partial fulfillment of the requirements

for the degree of Doctor of Philosophy

in the College of Optics and Photonics

at the University of Central Florida

Orlando, Florida

Fall Term

2019

Major Professor: Aristide Dogariu

ABSTRACT

Quantifying the structural dynamics of complex media is challenging because of the multiple temporal and spatial scales involved. Thanks to the ability to retrieve collective dynamics noninvasively, light scattering-based approaches are often the methods of choice. This dissertation discusses specific features of dynamic light scattering that utilizes spatio-temporal coherence gating. It is demonstrated that this optical fiber-based approach can operate over a large range of optical regimes and it has a number of unique capabilities such as an effective isolation of single scattering, a large sensitivity, and a high collection efficiency. Moreover, the approach also provides means for proper ensemble averaging, which is necessary when characterizing multi-scale dynamics. A number of applications are reviewed in which these specific characteristics permit recovering dynamic information of complex fluids beyond the capabilities of traditional light scattering-based techniques.

TABLE OF CONTENTS

LIST OF FIGURES

CHAPTER I: INFORMATION ENCODED IN TEMPORAL FLUCTUATIONS OF LIGHT

Optical techniques are often the methods of choice for monitoring the structural dynamics of complex media such as colloidal suspensions, polymer solutions, and biological fluids. In particular, their experimental flexibility and potential noninvasiveness are critical for the passive assessment of dynamic processes which is relevant in a number of fields including colloidal physics and surface chemistry, materials science and manufacturing, and biomedical applications.

More specifically, light scattering-based approaches have proved robust thanks to their capability to retrieve collective dynamic information through the intensity fluctuations of the light scattered. In particular, there are two main techniques namely Dynamic Light Scattering (DLS) [1], also known as Photon Correlation Spectroscopy (PCS) or Quasi-elastic Light Scattering (QELS) [2], and the so-called Diffusing Wave Spectroscopy (DWS) [3]. These two techniques – DLS and DWS – are complementary in the sense that they operate in opposite optical regimes.

Briefly, DLS is geometry-independent, it is restricted to singly-scattered light, and the characteristic correlation time of the light intensity fluctuations is associated to displacements of the scattering centers over one wavelength. Conversely, DWS is suitable for situations of strong multiple scattered i.e., optically dense systems, it is limited to transmission measurements, and the characteristic correlation time of the light intensity fluctuations is associated to a change of one wavelength in length over the entire light path. Additionally, the analysis of DWS data requires knowledge of the path length distribution of photons traveling through the sample, which can be

measured or assumed [3]. Therefore, DWS can access faster dynamics than DLS, but only if one knows the functional form of the distribution of path lengths throughout the scattering medium.

The optical sensing approach presented here, a spatio-temporal coherence-gated DLS, provides information about the dynamics of media with optical densities between these two extremes. This is possible because of an effective isolation of single scattering events, which is realized solely by optical means.

1.1 Fluctuations of light intensity

In its most general form, the total electric field scattered by a collection of N particles illuminated with a plane wave along the direction of the scattering vector $\bar{q}$ can be written as

$$E(\bar{q},t) = \sum_i^N p_i(\bar{q},t) exp[-i\bar{q}\cdot\bar{r_i}(t)] \quad (1)$$

where $p_i(\bar{q},t)$ is an amplitude factor depending on the instantaneous 'scattering configuration' of the i-th particle which in turn is determined by the particle's orientation and/or its (rapidly time-varying) scattering cross-section. A case where the scattering cross section varies at optical frequencies is unlikely. However, the particle's polarizability can lead to fast variations in its orientation. In the case of spherically symmetric particles with slowly-varying or constant scattering cross-section, the amplitude factor p_i is independent of time such that:

$$E(\bar{q},t) = \sum_i^N p_i(\bar{q}) exp[-i\bar{q}\cdot\bar{r_i}(t)] \quad (2)$$

If the particles are assumed to have identical scattering cross-section:

$$E(\bar{q},t) \cong p(\bar{q}) \sum_i^N exp[-i\bar{q}\cdot\bar{r_i}(t)] \quad (3)$$

This is a simplified expression for the total electric field scattered by a collection of N identical spherically symmetric particles illuminated by a plane wave. Nevertheless, in Optics we never measure the electric field directly, but field-field correlations.

Assuming the stationarity of the process (at least during the time of the measurement) the electric field autocorrelation function (ACF), can be written as:

$$\langle E(\bar{q},t)E^*(\bar{q},t+\tau)\rangle = |p(\bar{q})|^2 \left\langle \sum_{i,j} exp\left[-i\bar{q}\cdot\left(\bar{r_i}(t)-\bar{r_j}(t+\tau)\right)\right]\right\rangle \quad (4)$$

The ij cross terms included in this equation describe correlated motion of the particles. If the particles are assumed to be statistically independent i.e., non-interacting, as it would be the case of a dilute system, these cross terms vanish and the ACF can be expressed only in terms of self-interactions:

$$\langle E(\bar{q},t)E^*(\bar{q},t+\tau)\rangle = \begin{cases} |p(\bar{q})|^2 \sum_{i\neq j} \left\langle exp\left[-i\bar{q}\cdot\left(\bar{r_i}(t)-\bar{r_j}(t+\tau)\right)\right]\right\rangle \equiv 0 \\ |p(\bar{q})|^2 \sum_i \left\langle exp\left[-i\bar{q}\cdot\left(\bar{r_i}(t)-\bar{r_i}(t+\tau)\right)\right]\right\rangle \neq 0 \end{cases} \quad (5)$$

But, since the particles were assumed to be identical, the sum would be performed N times such that the ACF can be written as:

$$\langle E(\bar{q},t)E^*(\bar{q},t+\tau)\rangle = N|p(\bar{q})|^2 \left\langle exp\left[-i\bar{q}\cdot\left(\bar{r_i}(t)-\bar{r_i}(t+\tau)\right)\right]\right\rangle \quad (6)$$

The term $N|p(\bar{q})|^2$ is the total amplitude of scattering signal and can be taken as a normalization factor for the ACF. In this way, by normalizing with respect to the average total scattering, the electric field ACF can be written in terms only of the fluctuating quantities:

$$g^{(1)}(\bar{q},\tau) = \frac{\langle E(\bar{q},t)E^*(\bar{q},t+\tau)\rangle}{\langle |E(\bar{q},t)|^2\rangle} = \left\langle exp\left[-i\bar{q}\cdot\left(\bar{r_i}(t)-\bar{r_i}(t+\tau)\right)\right]\right\rangle \quad (7)$$

This expression for the normalized ACF can be found in the literature and it is typically written in the form [4, 5]:

$$g^{(1)}(\bar{q},\tau) = \langle exp[iq\Delta r(\tau)]\rangle \tag{8}$$

where $\Delta r(\tau) = r_i(t+\tau) - r_i(t)$ is the separation distance between the positions of the i-th particle at times t and t+τ, and $q = [4\pi n sin(\theta/2)]/\lambda_0$ is the magnitude of the scattering vector.

It is important to note that up to here no assumption has been made on the nature of the particle's displacement (only uncorrelated motion was assumed). In other words, we have not imply anything about the probability distribution of the particles' velocity. It is exactly this aspect of the system's dynamics what comes into play for the calculation of the ensemble average in Eq. (8).

For instance, it can be shown (by expanding the exponential term in Eq. (8)) that when the particle velocity has a symmetric probability distribution i.e., mean value and odd higher order moments are all zero, Eq. (8) can be written in terms of a generalized mean-square displacement (MSD) [6]:

$$g^{(1)}(\bar{q},\tau) = exp\left[-\frac{1}{6}q^2\langle\Delta r^2(\tau)\rangle\right] \tag{9}$$

If this symmetric particle velocity probability distribution is taken to be isotropic i.e., Maxell-Boltzmann distribution; that is a zero mean, Gaussian probability distribution of the particles' displacements, one would obtain the traditional expression of the ACF for a dilute, monodisperse collection of particles executing Brownian motion [1]:

$$g^{(1)}(\bar{q},\tau) = exp[-Dq^2\tau] \tag{10}$$

where the MSD is defined as $\langle \Delta r^2(\tau) \rangle \equiv 6D\tau$ with $D = k_B T / 6\pi\mu a$ the translational diffusion coefficient.

Regardless of the details discussed previously on the specific nature of the particles' velocity probability distribution, if the central limit theorem is satisfied, then the Siegert relation, $g^{(2)}(\tau) = 1 + \beta \left| g^{(1)}(\tau) \right|^2$ is valid [1, 7]. Thus, the intensity ACF function can be directly linked to the electric field ACF. In this way, the thermodynamic and hydrodynamic properties of the system can be connected directly to measurable optical quantities. In other words, transport properties of the scattering centers in the system can be inferred from the analysis of the light intensity fluctuations.

Fig. 1 summarizes this process where the dynamic information is encoded into light intensity fluctuations. The far-field speckle pattern formed by the interference of the field scattered from the scattering centers has regions of high and low intensity due to constructive and destructive interference. At a single speckle location, the well-defined temporal correlation properties of the light intensity fluctuations contain information of the transport properties of the scattering centers.

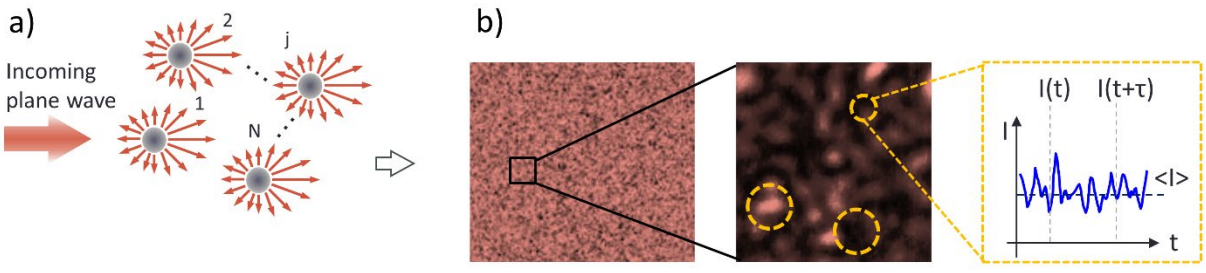

Figure 1. a) The total electric field scattered by a collection of N identical, non-interacting particles illuminated by a plane wave produces a speckle pattern as the result of the interference between the field scattered from all the particles. b) The speckle pattern shows regions of high and low intensity due to constructive and destructive interference. At a single spatial point of the speckle strong temporal fluctuations of the intensity, with a certain well defined temporal correlation, are observed.

Eq. (8)-(9) encloses the most fundamental aspects of the system's dynamics. The interpretation of the general MSD can take several forms depending upon the nature of the situation described. For instance, the time-varying MSD can be interpreted as the result of the diffusion of particles with time-varying size, or particles diffusing in a suspending medium with time-varying viscosity, or as a time-varying diffusion constant, or simply, by the definition of the MSD itself, as the time-dependent evolution of the extent explored by the random walkers. All these interpretations can be incorporated into the Langevin equation through the velocity autocorrelation function in order to infer the forces acting on the particles [8]. The usefulness of this generalization of the MSD will be shown in the following sections in the context of the hydrodynamic coupling and caging effects typically encountered in complex systems consisting of polymer networks.

1.2 Dynamic light scattering

In DLS the autocorrelation function for Brownian particles (Eq. (10)) is extended to the general case of a polydisperse system such that it is expressed as a sum of the exponential decays corresponding to each of the species in the population [1]:

$$\left|g^{(1)}(q;\tau)\right| = \int_0^\infty G(\Gamma)exp(-\Gamma\tau)d\Gamma = \sum_{i=1}^{N} G(\Gamma_i)exp(-\Gamma_i\tau) \tag{11}$$

where $\Gamma_i = D_i q^2$ is the characteristic decay rate of the i-th population and $G(\Gamma_i)$ is the distribution of these decay rates.

Fig. 2 shows a schematic of the DLS experimental setup. As general features, DLS is independent of the experimental geometry i.e., can be performed at various angles, and it is restricted to singly-scattered light i.e., transparent samples. As an example, for silica particles ($n \approx 1.5$) suspended in

water, multiple scattering effects can be neglected for concentrations $< 1\ wt\%$. The characteristic correlation time in DLS is associated to particles diffusing over one wavelength. Due to the experimental flexibility, the translational diffusion coefficient can be retrieved at a single or multiple angles depending on the wave vector q.

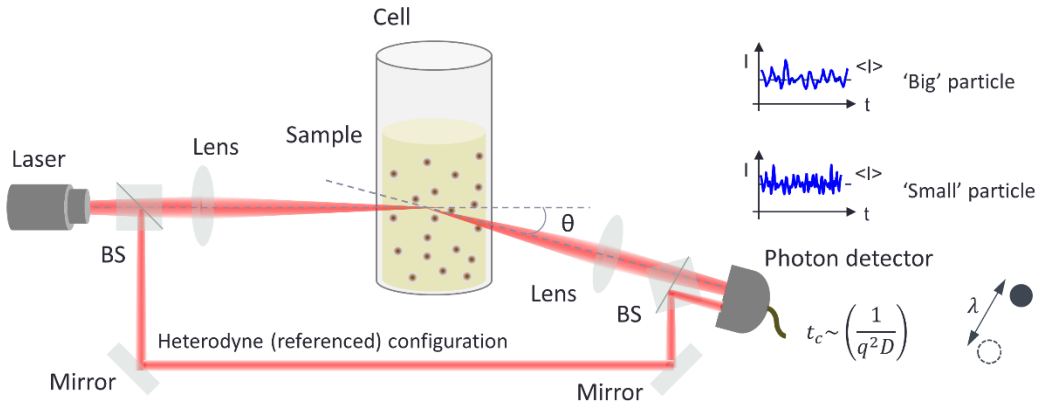

Figure 2. Schematic of a DLS experiment with the option of having a referenced (heterodyne) configuration. The characteristic correlation time in DLS is associated to particles diffusing over one wavelength.

In DLS, the intensity ACF is typically analyzed by the cumulants method first proposed by Koppel [9]. This analysis is justified because the electric field ACF (Eq. (11)) happens to have the form of the moment-generating function of Γ. This approach is overall less affected by experimental noise but one should exert care in that this method is valid for small τ and sufficiently narrow G(Γ) [10]. Also, despite the generality of this approach, in practice the analysis is truncated up to the second or third order moment due to the loss of accuracy of higher-order terms of the power-series [11].

An alternative method, which was first proposed by Provencher, is based on the numerical inversion of Eq. (11) via Laplace transform using the well-known CONTIN algorithm [12, 13]. This approach is ideal for polydisperse systems with particle populations close in size (down to a factor of 5 between the populations) that cannot be resolved with the cumulants method.

1.3 Diffusing-wave spectroscopy

DWS is derived from DLS in the limit of strong multiple scattering [3]. In this case, it has been demonstrated that the electric field ACF takes the form [14]:

$$g^{(1)}(\tau) \propto \int_0^\infty p(s) exp\left[-\left(\frac{2\tau}{\tau_0}\right)\left(\frac{s}{l^*}\right)\right] ds \tag{12}$$

where τ is the delay time, $\tau_0 = 1/\Gamma = 1/(D^2 q)$ is the characteristic diffusion time, l^* is the transport mean free path, and $p(s)$ is the probability that the light travels the path s.

Details in the derivation of Eq. (12) can be found elsewhere [15, 16]. It is important to notice that the analysis of DWS data is based on the theory of diffusion of light, which implies knowing the probability density of the distribution of photon paths through the medium, $p(s)$, and the associated parameters such as the photon transport mean free path, l^*, and the photon absorption length, l_a. This path lengths can be measured for the specific system under study but, for practical purposes, it is typically assumed to be Gaussian [3].

Fig. 3 shows a schematic of the DWS experimental setup. As general features, DWS is restricted to situations of strong multiple scattering i.e., optically dense systems such as highly-concentrated samples, and is limited to transmission measurements. The characteristic correlation time in DWS is associated to a change of a wavelength over the entire path length. This means that in DWS, the scattering particles need to diffuse less, and therefore over shorter time scales, in order to cumulatively induce the path length difference required for the scattered field to decorrelate. Therefore, DWS can access much faster dynamics than DLS.

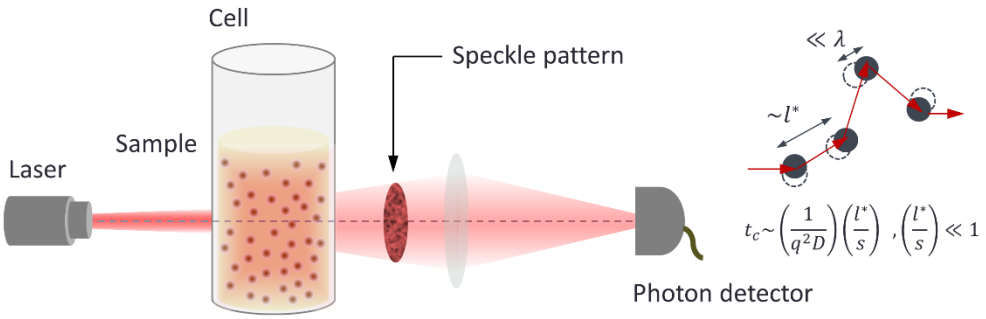

Figure 3. Schematic of a DWS experiment. The characteristic correlation time in DWS is associated to a change of one wavelength over the entire path length.

Short after its creation, the use of DWS was extended to large variety of applications in condensed matter sciences. For instance, in homogeneous colloidal systems, DWS has been used to study fast hydrodynamics, interparticle correlations, phase transitions, and convective motion [17, 18]. One of its most popular uses is in microrheology for the quantitative measurement of the viscoelastic properties of complex fluids [19, 20]. More recently, its use has been extended to biomedical applications for clinical diagnosis [21].

The main drawback of this technique is its strong geometry dependence. Besides the assumptions on the distribution of path lengths that have to be made (which does not always apply) in the limit of diffusive transport, it is important to realize that $p(s)$ can take certain analytical forms only for samples with flat boundaries i.e., flat sample cells. It has been until very recently that that the information retrieval in DWS was extended for measurements in cylindrical sample cells [22].

A brief review on DWS, including both a detailed discussion on its limitations as well as some approaches that have been developed to mitigate them, are summarized in the Appendix D.

CHAPTER II: COHERENCE-GATED DYNAMIC LIGHT SCATTERING

2.1 General concept

In general terms, the underlying principle of operation of our spatio-temporal coherence-gated DLS technique can be understood as the (temporal) partially coherent interference of two (spatial partially coherent) speckle fields. More specifically, in our optical fiber-based implementation, those two interfering fields correspond to that generated after reflection at the end facet of a multimode fiber (MMF), $E^{(r)}(t)$ (reference field), and the portion of the field scattered by the system under study, $E^{(s)}(t)$, that is coupled back to the MMF, as schematically shown in Fig. 4.

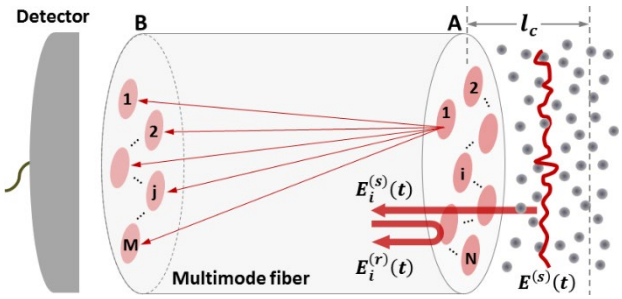

Figure 4. Fiber-based implementation of the spatio-temporal coherence-gated dynamic light scattering. The reference field, $E^{(r)}(t)$, generated from the Fresnel reflection at the distal end facet A of a multimode fiber (MMF), interferes with the portion of the scattered field, $E^{(s)}(t)$, that is coupled back to the MMF. The depth from where coherent scattering is collected is determined by the coherent length of the light source, l_c. The heterodyne amplification of $E^{(s)}(t)$, which results from its interference with the local oscillator located at the fiber-medium interface, permits measuring the dynamics of the complex medium at the detector side B.

The interaction between the reference and scattered fields is gated three-dimensionally by i) the spatial partially coherent speckle field distribution used for illumination, which across the facet of the fiber is coherent only within the extent of each speckle, and ii) the spectral properties of the

incident radiation, which leads to a finite depth in which the two fields maintain a phase relation, as illustrated in Fig. 4.

This situation is similar to the addition of correlated speckle fields for the particular case where their correlation is limited to take place only within the extent of the coherence length [23] or, equivalently, as the heterodyne amplification of a scattered field, with a local oscillator of the same frequency, at multiple, independent spatial locations in parallel [24, 25].

Since $E^{(r)}(t)$ and $E^{(s)}(t)$ can interfere only at each location of independent illumination i.e., at each speckle, the total field at the end facet of the fiber (location A) can be written as the coherent addition i.e., on an amplitude basis, of the reference and scattered field in the form:

$$E^A(t) = \sum_i^N E_i^{(r)}(t) + E_i^{(s)}(t) \tag{13}$$

It is well known that the coherent addition of speckle fields does not reduce the contrast of speckles and has no effect on the signal-to-noise ratio. In other words, the addition of two random fields on an amplitude basis results simply on a third random field distribution with statistics indistinguishable from the original ones [26, 27].

Based on this idea, the MMF can be thought to be a black box that transfers the field distribution $E^A(t)$ into a new field distribution $E^B(t)$ on the other end. Thus, for a loss-less system and without any special cross-channel interaction between the two ends A and B, the inter-channel communication will lead to a uniform contribution from all the i-th locations on the A-side onto all the j-th locations on the B-side such that the total field at a single j location on the B-side is:

$$E_j^B(t) = \frac{1}{\sqrt{N}} \sum_i^N E_i^{(r)}(t) + E_i^{(s)}(t) \tag{14}$$

In their more general form, the reference and scattered fields at the i-th location can be written as:

$$E_i^{(r)}(t) = \varepsilon_i^{(r)}(t)e^{-j\left[\omega_r t - \phi_i^{(r)}(t)\right]} \tag{15a}$$

$$E_i^{(s)}(t) = \varepsilon_i^{(s)}(t)e^{-j\left[\omega_s t - \phi_i^{(s)}(t)\right]} \tag{15b}$$

In this general form one can recognize the notation typically used for the heterodyne technique in radar applications where, in general, the local oscillator has different frequency than the signal that is to be amplified [24, 25]. In our particular conditions of quasi-elastic scattering the optical frequency of both the local oscillator and the scattered field are the same i.e. $\omega_r \approx \omega_s = \omega$.

The electric field cannot be measured at optical frequencies and only the slowly-varying envelope can be followed. Moreover, since it is only the relative phases what contain the information of the relation between the two fields, the rapidly-varying oscillations can be removed from the previous expressions. Furthermore, if the field amplitudes are assumed to be approximately constant over time and only the time-varying phase $\phi_i(t)$ is considered, the previous definitions of the fields simplify to:

$$E_i^{(r)}(t) = E_i^{(r)} = \varepsilon_i^{(r)} \tag{16a}$$

$$E_i^{(s)}(t) = \varepsilon_i^{(s)}e^{-j\phi_i(t)} \tag{16b}$$

The total intensity right behind the end facet of the fiber on the A-side is the (incoherent) addition of the intensity contributions from at all i-locations. However, within each of these locations, the local intensity results from the coherent addition $E_i^{(r)}(t)$ and $E_i^{(s)}(t)$ such that:

$$I^A(t) = \sum_i^N \left| \varepsilon_i^{(r)} + \varepsilon_i^{(s)} e^{-j\phi_i(t)} \right|^2 \quad (17)$$

On the B-side the situation is similar in the sense that the total intensity associated to that spatially partially coherent field distribution is given by the contribution from all j locations, with the difference that now the local intensity at the j-th location contains contributions from all the i-locations on the A-side:

$$I^B(t) = \sum_j^M I_j^B(t) = \sum_j^M \left| \frac{1}{\sqrt{N}} \sum_i^N \varepsilon_i^{(r)} + \varepsilon_i^{(r)} e^{-j\phi_i(t)} \right|^2 \quad (18)$$

The above-mentioned energy conservation argument (the total intensity at both ands A and B is the same) i.e., $I^A(t) = I^B(t)$, can be verified by expanding Eq. (6), while assuming that i) the amplitude of the electric fields involved is roughly the same at all locations i.e., $\varepsilon_i^{(r)} = \varepsilon^{(r)}$ and $\varepsilon_i^{(s)} = \varepsilon^{(s)}$, ii) the self-interaction of the reference field at two different spatial locations if forbidden (due to the spatial partially coherent nature of the reference field), iii) the interaction between the reference field at certain location and the scattered field at a different location is forbidden (due to the scattered field is locked to interact only with its corresponding reference field at the same location), iv) the self-interaction of the scattered field at two different spatial locations if forbidden, and v) the scattered field $E^{(s)}(t)$ completely fills the acceptance cone of the MMF (the number of speckles remains the same at any location along the multimode fiber i.e., M=N).

The conservation of energy has deeper implications since it results in that the field distributions at both ends are connected only by a phase relation, which means that the intensity statistics are conserved. In other words, the intensity autocorrelation function, which encodes the dynamic

information of the complex medium, gives the same result regardless of the location at which it is calculated along the fiber.

2.2 Optical modes interpretation

Interestingly, one can get to the same conclusion by following a different yet equivalent reasoning in terms of the modal coupling in the multimode fiber.

Irrespectively of the initial input field distribution before reflection at the end facet of the fiber, a strong mode coupling occurs between the input and all the modes supported by the MMF due to the abrupt change of the propagation angle after the Fresnel reflection. The reference field can therefore be considered as the superposition of all the eigenmodes of the MMF. More importantly, at the fiber-medium interface all the mode are excited in phase.

Strong inter-mode coupling in MMF occurs mainly due to the modal dispersion and the non-uniformity of the fiber along the propagation direction [28, 29]. Due to the nature of their origin, these effects are naturally more significant in long fibers (hundreds of meters or longer). For short MMFs in the weakly-guiding regime both the modal dispersion and the non-uniformity of the optical fiber can be neglected such that the modes in the optical fiber are weakly coupled [30-33]. These are both reasonable assumptions for the short, standard MMFs used in our experiments.

Having a weak modal coupling is equivalent to neglecting the cross-interactions at different spatial locations in the speckle fields. Moreover, if besides the in-phase excitation one assumes that all the modes are also equally excited in amplitude, one can easily picture the independent back-propagation of all the modes in the MMF. In this way, one can see that the field distributions at

both ends A and B contain the contribution from all the modes and only a phase difference after propagation connects the two.

2.3 Dynamic information retrieval

From the same definitions of the reference, scattered, and total fields used before (Eq. (15)-(16)) i.e., $E_i^{(r)}(t) = \varepsilon_i^{(r)}$, $E_i^{(s)}(t) = \varepsilon_i^{(s)} e^{-j\phi_i(t)}$, and $E_i(t) = E_i^{(r)}(t) + E_i^{(s)}(t) = \varepsilon_i^{(r)} + \varepsilon_i^{(s)} e^{-j\phi_i(t)}$, one can write the normalized electric field autocorrelation function (E-ACF) of the scattered field, $G^{1\,(s)}(\tau) = \langle E^{(s)}(t) E^{*(s)}(t+\tau) \rangle$, as:

$$g^{1\,(s)}(\tau) = \frac{\langle E^{(s)}(t) E^{*(s)}(t+\tau) \rangle}{\langle E^{(s)}(t) \rangle \langle E^{(s)}(t+\tau) \rangle} = \sum_i^N \langle e^{-j[\phi_i(t) - \phi_i(t+\tau)]} \rangle \tag{19}$$

after neglecting cross-interactions at different locations, and assuming that the amplitude of the electric fields is roughly the same at all locations i.e. $\varepsilon_i^{(s)} = \varepsilon^{(s)}$. From this expression, it can be seen that $\left| g^{1\,(s)}(\tau) \right|^2 = 1$.

Similarly, the E-ACF of the total field, $G^1(\tau) = \langle E(t) E^*(t+\tau) \rangle$, can be calculated as:

$$G^1(\tau) = N \varepsilon^{2\,(r)} + \varepsilon^{2\,(s)} g^{1\,(s)}(\tau) \tag{20}$$

In this case, both cross-interactions have been neglected and the amplitude of the electric fields has been assumed to be roughly constant, but also the random process has been assumed to be statistically stationary i.e., $\langle e^{-j\phi_i(t)} \rangle = \langle e^{+j\phi_i(t+\tau)} \rangle$, and the random variable, ϕ_i, to be uniformly distributed over all possible angles i.e., the quantity $e^{-j\phi_i(t)}$ is assumed to be uniformly distributed over the complex plane with zero average.

By following similar guidelines, the intensity autocorrelation function (I-ACF) of the total intensity, $G^2(\tau) = \langle I(t)I(t+\tau)\rangle$, where $I(t) = \sum_i^N \left|\varepsilon_i^{(r)} + \varepsilon_i^{(s)} e^{-j\phi_i(t)}\right|^2$, is given by:

$$G^2(\tau) = N\left(\varepsilon^{2\,(r)} + \varepsilon^{2\,(s)}\right)^2 + 4\varepsilon^{2\,(r)}\varepsilon^{2\,(s)} Re\left\{g^{1\,(s)}(\tau)\right\} \tag{21}$$

Note that the term $\varepsilon^{4\,(s)}$implicitly contains the contribution $\left|g^{1\,(s)}(\tau)\right|^2 = 1$. The normalized I-ACF, $g^2(\tau) = \frac{\langle I(t)I(t+\tau)\rangle}{\langle I(t)\rangle\langle I(t+\tau)\rangle} = \frac{G^2(\tau)}{\langle I(t)\rangle\langle I(t+\tau)\rangle}$, can then be written as:

$$g^2(\tau) = \frac{G^2(\tau)}{\langle I(t)\rangle\langle I(t+\tau)\rangle} = \frac{N\left(\varepsilon^{2\,(r)} + \varepsilon^{2\,(s)}\right)^2 + 4\varepsilon^{2\,(r)}\varepsilon^{2\,(s)} Re\left\{g^{1\,(s)}(\tau)\right\}}{N^2(\varepsilon^{2\,(r)} + \varepsilon^{2\,(s)})^2}$$

$$= \frac{1}{N} + \left(\frac{2\varepsilon^{(r)}\varepsilon^{(s)}}{N\left(\varepsilon^{2\,(r)} + \varepsilon^{2\,(s)}\right)}\right)^2 Re\left\{g^{1\,(s)}(\tau)\right\} \tag{22}$$

by using the expression of the total intensity $I(t) = \sum_i^N \left|\varepsilon_i^{(r)} + \varepsilon_i^{(s)} e^{-j\phi_i(t)}\right|^2$ and noting that $\langle I(t)\rangle = \langle I(t+\tau)\rangle = N\left(\varepsilon^{2\,(r)} + \varepsilon^{2\,(s)}\right)$.

An expression of the normalized I-ACF can also be written as

$$g^2(\tau) = \frac{1}{N} + \left(\frac{2\alpha}{N(\alpha^2+1)}\right)^2 Re\left\{g^{1\,(s)}(\tau)\right\} \tag{23}$$

where the relation $\varepsilon^{(r)} = \alpha\varepsilon^{(s)}$ has been used. A detailed derivation of the expressions above can be found in the Appendix A. From this expression it follows that $\lim_{N\to\infty} g^2(\tau) = 0$ and $\lim_{\alpha\to\infty} g^2(\tau) = \frac{1}{N}$, which is consistent with the fact that for a very large number of speckles i.e., large N, all correlations vanish while, on the other hand, a very large amplitude of the reference field i.e., large α, the dynamic information is screened due to the decrease of the contrast of the fluctuations.

It can also be seen that the best condition for recovering $g^{1\,(s)}(\tau)$, which contains the information about the motion of the scattering centers, is for a single point of illumination (N = 1), similarly to the case in which a single-mode receiver is used in DLS [34]. However, it can also be noted that, at the expense of a sacrifice in the amplitude of the I-ACF, the dynamic information of the system contained in $g^{1\,(s)}(\tau)$ can be recovered from the experimental observable $g^{2}(\tau)$ regardless of the number of speckles.

Using single-mode fibers is the best option if the noise at the detection system is low or if the scattering signal is strong enough. Unfortunately, these conditions are unlikely in reality and that is why multimode fibers exhibit a better performance. This becomes even more evident when a temporal gate is implemented since the signals involved are weaker. Rigorously, the optimization of the signal-to-noise ratio (optimal number of speckles N, of certain size, per unit area) can be achieved by dynamically controlling both the number of spots (spatial coherence), the spectral properties of the source (temporal coherence), and the finite size of the detector [35].

Finally, using a speckle field as the illumination gives an additional advantage. Due to the multiple, independent illumination locations that simultaneously sample the volume of observation at different spatial locations, non-ergodicity within the volume of observation can be mitigated since a much larger range of the system's phase-space can be explored by this parallelized arrangement. A similar approach could be implemented with N single-mode fibers. Here, we are performing a parallel sampling with single optical fiber. Further details, including a detailed discussion on non-ergodic manifestations in light scattering-based measurements, can be found in Ref. [36], and in the Appendix B.

In terms of the information retrieval, it is worth emphasizing that in a traditional DLS experiment the only parameter of interest is the characteristic correlation time of the light intensity fluctuations, τ, which provides the hydrodynamic information of the diffusing scattering centers. Specifically, in a DLS experiment τ is retrieved from the characteristic decay of the (time-domain) intensity correlation function; τ can also be retrieved in the frequency domain, as in our case, from the so-called corner frequency of the power spectrum of the intensity fluctuations, $P(f)$, with f being the frequency. Importantly, τ does not depend on the actual magnitude of the signal measured, but on its temporal statistical characteristics. Additionally, in our approach, on the other hand, two additional optical parameters can be followed. The first one is the time-averaged total power, which is mainly determined by the local oscillator and therefore it provides information on the Fresnel reflection at the fiber-medium interface i.e., $\langle I \rangle_t \approx \langle |E_r|^2 \rangle_t \propto |r|^2$. The second parameter is the total energy in the power spectrum of the light intensity fluctuations, which provides information on the scattering density due to the optical isolation of single scattering: $\beta = \int_0^{+\infty} P(f) df \propto (\sigma N)^2$.

The capability to retrieve information on the effective optical properties of the medium is a unique feature that was not available in traditional DLS until now. It opens the possibility to fully characterize, mechanically and optically, inhomogeneous media in conditions of weak scattering, noisy backgrounds, and anisotropic scattering. These are circumstances commonly encountered in biological systems or gel-like materials [37].

On the basis of single-scattering dominance, the power spectrum of the intensity fluctuations measured can be decomposed into a collection of discrete representative contributions, $P(f) =$

$(2/\pi)\sum_{i=1}^{N}(a_i/\tau_i)[f^2+(1/\tau_i)^2]^{-1}$ with a_i being the relative amplitude, $\sum_{i=1}^{N} a_i = 1$, and τ_i the representative relaxation time of the i-th population, respectively [38, 39]. From here, the Stokes-Einstein formulation can be followed to calculate the diffusion properties of the scattering centers i.e., effective diffusion coefficient, $D_{eff,i} = \frac{k_B T}{3\pi\upsilon d_{eff,i}} = \left(\frac{2\pi}{q^2}\right)\left(\frac{1}{\tau_i}\right)$, where k_B, T, υ, and d_{eff} are the Boltzmann constant, the absolute temperature, the (effective) viscosity of the solvent, and the hydrodynamic size, respectively, and $q = 2k_0 n sin(\theta/2)$ is the magnitude of the scattering vector, with $k_0 = \frac{2\pi}{\lambda_0}$ and $\theta = \pi\, rad$, in our reflection geometry [1].

The spectral decomposition of $P(f)$ can be directly incorporated into the calculation of the MSD, $\langle \Delta r^2(t)\rangle = -\frac{6}{q^2} ln\left[\sum_{i=1}^{N} a_i exp\left(-\frac{2\pi t}{\tau_i}\right)\right]$, and for the estimation of the viscoelastic properties of the suspending medium (for tracers of known size) [40, 41], $|G^*(\omega)| \approx \frac{k_B T}{\pi a \langle \Delta r^2(1/\omega)\rangle \Gamma[1+\alpha(\omega)]}$ where $\alpha(\omega) = \frac{\partial ln\langle \Delta r^2(t)\rangle}{\partial ln(t)}\Big]_{t=1/\omega}$, from where the elastic component, $G'(\omega) = |G^*(\omega)| cos(\pi\alpha(\omega)/2)$, and the viscous component, $G''(\omega) = |G^*(\omega)| sin(\pi\alpha(\omega)/2)$, of the local complex viscoelastic moduli can be readily calculated.

The parameter $\alpha(\omega)$, which is calculated from the time-dependent logarithmic slope of the MSD, lies between the limits of elastic confinement ($\alpha = 0$) and viscous diffusion ($\alpha = 1$), and describes the transport properties in the intermediate viscoelastic regimes of complex media.

Additionally, the ratio between the viscous and the elastic component i.e., the so-called frequency-dependent loss tangent, $\gamma(\omega) = G''(\omega)/G'(\omega)$, contains information on the material's energy dissipation. In other words, on the elasticity i.e., solid-like behavior, or plasticity i.e., liquid-like

behavior, of the medium. In our particular case, the frequency-dependent local viscoelasticity should not be strictly interpreted as the macroscopic rheological properties due to the inherent structural discontinuity around the particles which, additionally, could also be hydrodynamically coupled to the complex medium [42, 43]. Nevertheless, a measure of local stiffness of the material can still be obtained by following the frequency-averaged loss tangent $\bar{\gamma} = \langle G''(\omega)/G'(\omega)\rangle_\omega$ [40, 44]. Interestingly, although it is determined by the scattering particles, this quantity does not require knowledge of the size of the tracer in order to be retrieved, which means that qualitative rheological properties of the medium can be retrieved by simply following the characteristic correlation times of the scattering events.

In the following we review a number of different applications where the unique features of our technique – the effective isolation of single scattering, the large sensitivity and high collection efficiency, and the capability to operate over a wide range of optical regimes while providing means for proper ensemble averaging – can be clearly identified and used from a practical standpoint in situations that are beyond the capabilities of traditional light scattering-based techniques.

2.4 Optical fiber-based experimental implementation

The experimental setup, which is shown schematically in Fig. 5, consists of a robust implementation of a fiber-based, common path interferometer built around MMFs. Light from a low-coherence source (Superlum BLM-S-670-G-I-4, super luminescent diode of 7 nm bandwidth centered at 670 nm; coherence length of about 30 μm in aqueous media), is launched into the MMF and then coupled into a 50/50 multimode splitter. The fibers used in the experiments are

commercially available 62.5/125 MMF, whose core and cladding diameter is 62.5 μm and 125 μm, respectively. The fluctuations of the electrical signal are digitized using specialized DAQ hardware and further analyzed in the frequency domain. Effectively, the optical signals measured come from a picolitter-sized volume, as determined by the core size of the MMF and the spectral properties of the light source.

The inset illustrates the depth-limited, heterodyne amplification of $E^{(s)}(t)$ through its self-referenced interference with $E^{(r)}$ when the complex medium is illuminated with a spatially partially coherent field through a partially-transmitting interface [45, 46].

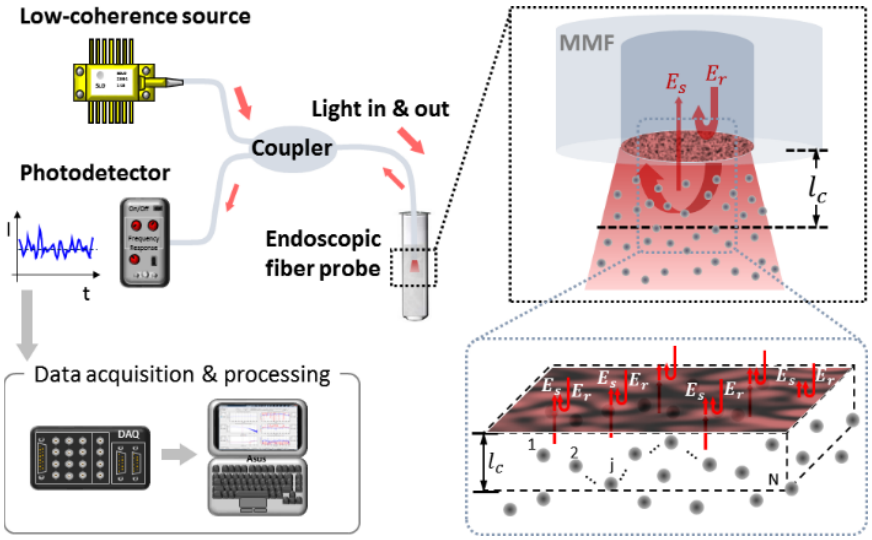

Figure 5. Schematic of the experimental implementation of the spatio-temporal coherence-gated dynamic light scattering.

2.5 Illumination in the experiments

Fig. 6 shows part of the experimental setup shown in Fig. 5 – the output of the low-coherence light source (single-mode fiber, SMF) coupled into a multimode coupler with standard 62.5/125 MMF. The output ports of the coupler going to the sample and the detection system are indicated.

Fig. 6(a)-(b) show pictures of the intensity distribution at the end facet of the MMF before and after the coupler, respectively. Note the logarithmic vertical scale in both histograms. It can be seen that a negative exponential distribution of intensities before the coupler (Fig. 6(a)), which is expected for a fully-developed speckle resulting after propagation through a sufficiently long section of MMF [23], transforms into a Gaussian distribution at the output port of the coupler that goes to the sample (Fig. 6(b)). The latter constitutes the actual illumination used in the experiments. From this Gaussian intensity distribution, it can be seen that the speckles have certain average intensity. This probes valid the above-explained assumption on the approximately constant amplitude of the electric field at all locations (See details in the Appendix A, around Eq. (A5)).

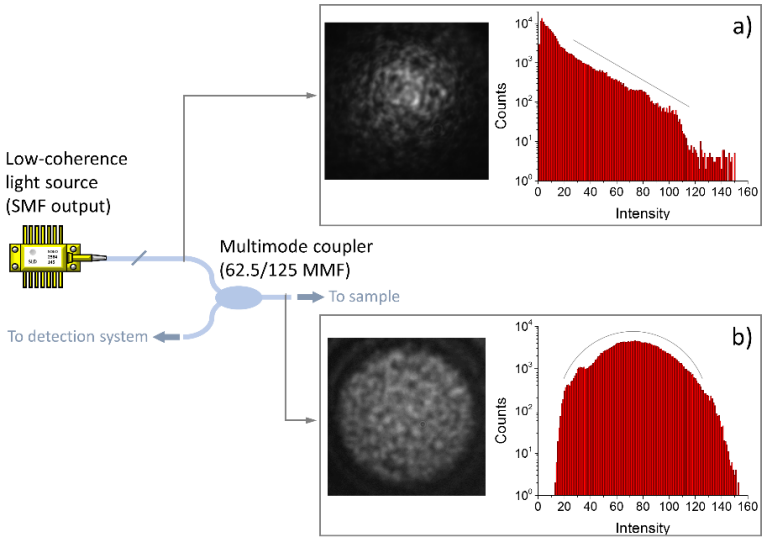

Figure 6. Characteristics of the illumination used in the experiments. Pictures of the intensity distribution at the end facet of the MMF a) before, and b) after the coupler, and its corresponding histogram, are shown for comparison. Panel b) shows the actual illumination used in the experiments. The Gaussian distribution of intensities allows having speckles with certain average intensity such that most of them contribute roughly equally to the optical signal.

Moreover, from the standpoint of the implementation and the information retrieval, having such a Gaussian distribution of intensities allows having a larger amount of independent, self-referenced signals contributing more or less equally to the optical signal as compared to the negative exponential distribution. This translates into an effective suppression of non-ergodicity since the system's dynamics is measured at a large number of independent spatial locations.

2.6 Other fiber-based approaches

Regarding optical fiber-based DLS, which was first proposed by Wiese and Horn [47], and then used by a number of other researchers [48, 49], we note that both the principle of operation of our spatio-temporal coherence-gated DLS technique and the information content are different.

Traditional fiber-based DLS operates in a homodyne configuration and the light intensity fluctuations are measured non-interferometrically along a single wave vector by means of spatially filtering the signal with single mode fibers. In this context, it was proved that Brownian dynamics can be reliably retrieved, after correcting for both multiple scattering and particle interactions, only when (i) the acceptance angle is small and (ii) the core of the optical fiber is much smaller than the scattering mean-free path. As a result, this fiber-based DLS is limited due the low level signals associated to the reduction of the scattering mean free path in highly scattering environments [50].

Additionally, those implementations there is no selection of path lengths due to the use of coherent light. Thus, if the issues related to multiple scattering could be solved for multimode operation, this approach would be preferred due to the higher collection, which would be favorable in situations where weak scattering is generated by 'inefficient' scatterers, or by low particle number densities, which, additionally, limits the applicability of the traditional statistical tools for signal analysis, e.g., the central limit theorem [50]. Here, we solve the problem of multiple scattering for multimode operation by means of a temporal coherence gating together with the heterodyne amplification in our self-referenced common-path interferometer. This effectively isolates a picolitter-sized optical volume where the single scattering contribution collected amply dominates.

Finally, from a more fundamental point of view, our three-dimensional spatio-temporal coherence shaping permits sampling simultaneously at multiple spatial locations within the coherence volume. This is extremely important because ensemble dynamics can then be measured in situations where long-term time averaging is not practical by accessing to an extended system's phase space instead. In other words, the parallel sampling allows for averaging over a

representative number of the system's configurations such that one can account for the non-ergodic dynamics, typically encountered in dense soft systems, even in non-stationary processes [51].

CHAPTER III: CHARACTERIZATION OF DYNAMICS OF COMPLEX MEDIA

3.1 Optically dense media

First, we illustrate the impact of implementing a temporal coherence gate for the effective isolation of singly-scattered light over a wide range of optical regimes. This directly results, for instance, in the capability to perform particle sizing in optically dense colloids, in which strong scattering arises due to the large concentration of particulates. In other words, if single scattering is effectively isolated then the correlation time of the intensity fluctuations can be used to reliably retrieve hydrodynamic information irrespectively of the macroscopic scattering properties of the sample.

3.1.1 Particle sizing in highly-concentrated colloids

We demonstrate this by measuring the particle size of known tracers in highly concentrated colloidal suspensions. Fig. 7 shows the raw measurements of the hydrodynamic size measured in polystyrene colloidal suspensions over three decades of concentration, for beads with nominal size of 100 nm and 330 nm, respectively. The dashed lines on the plot show the nominal size and the manufacturer tolerances (standard deviation of ±10% of the nominal size). The inset shows a digital photograph of the samples measured.

In a particle size measurement, multiple scattering manifests as a decreasing hydrodynamic size with increasing concentration due to faster decorrelation, as can be appreciated for the case of the

smaller particles. On the other hand, hydrodynamic interactions manifest as an increasing hydrodynamic size with increasing concentration due to correlated particle displacements, as in the case of larger particles. Despite both of these effects start taking place mainly at larger concentrations, and can be corrected, we show the raw measurements to emphasize that the contribution from multiple scattering is minimal, which indicates an efficient isolation of singly scattered light, as can be verified from the fact that the hydrodynamic size recovered lies within the boundaries of the manufacturer's tolerances.

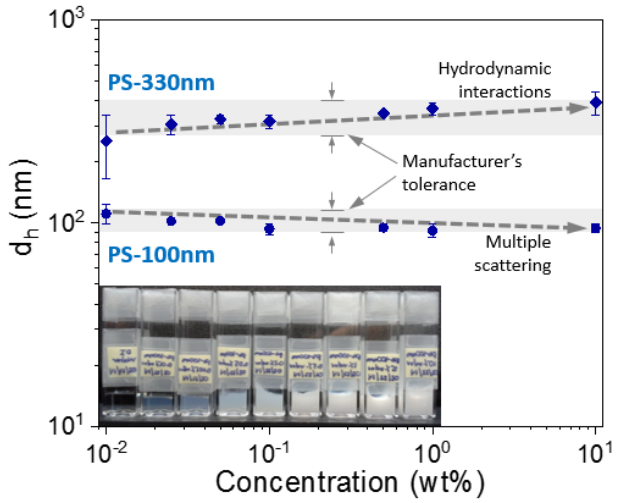

Figure 7. Particle size measurements with LC-DLS in optically dense media. Polystyrene monodisperse colloidal suspension measured over three decades of concentration.

3.1.2 Micro-rheology of gels

As seen in the previous example, the fact that the measurement is performed over a small, optically-isolated volume allows collecting singly scattered light regardless of the macroscopic scattering characteristics of the complex medium. In other words, in the small coherence volume, the medium is optically transparent and single-scattering can be collected from the particles.

With this picture in mind, one can think of situations where the strong scattering is induced by the medium itself where the tracers are embedded, even though the concentration of particles remains low. In these situations, other light scattering-based techniques cannot operate or require a large concentration of particles to overcome the inherent background, which sometimes results in significant alterations of the structure of the medium.

A good example of such complex media are gels and biological fluids. The micro-rheological characterization of such media, additionally, requires i) proper ensemble averaging due to the inhomogeneous nature of their structure and ii) low particles-doping levels in order to perform a passive measurement. In this context, the use of spatially partially coherent light and the larger collection area of a MMF allows avoiding non-ergodic manifestations while being sensitive enough to collect strong signals, as it will be seen in detail in upcoming sections.

In these experiments, we show the characterization of the structural and rheological properties of a hydrogel [52]. Polystyrene spherical particles with a diameter of 100 nm were loaded into a hydrogel formed by the self-assembly of sodium deoxycholate (NaDC) in aqueous solution with sodium chloride. The NaDC hydrogel consists of a three-dimensional network of nanofibers and the polystyrene particles loaded into this network are used as light scattering probes to passively measure the local viscoelastic response of the hydrogel.

The local viscoelastic properties of the medium around the particles influence their diffusion behavior. As mentioned before, this can be characterized by means of the temporal evolution of their MSD. The calculated MSD of the probe particles is presented in Fig. 8(a). The MSD clearly exhibits three different regimes. At short times, the MSD is governed by the normal diffusion of

the particles in the solvent and therefore grows linearly with time. At intermediate times the MSD increase slows down considerably while at longer times the normal linear increase is reached again. This is a typical behavior of complex fluids consisting of micellar solutions and particle probes embedded in worm-like structures.

A quantitative description of the structure of the hydrogel can be pursued in terms of particles confined to cages formed by the polymer network [53], as indicated schematically in Fig. 8(a). Such caging effect is reflected in the transition of the MSD between two time scales in which the system diffuses normally with different diffusion constants i.e., asymptotic limits at short and long times, which are connected by a region of sub-diffusive motion i.e., temporarily, partial trapping, of the particles.

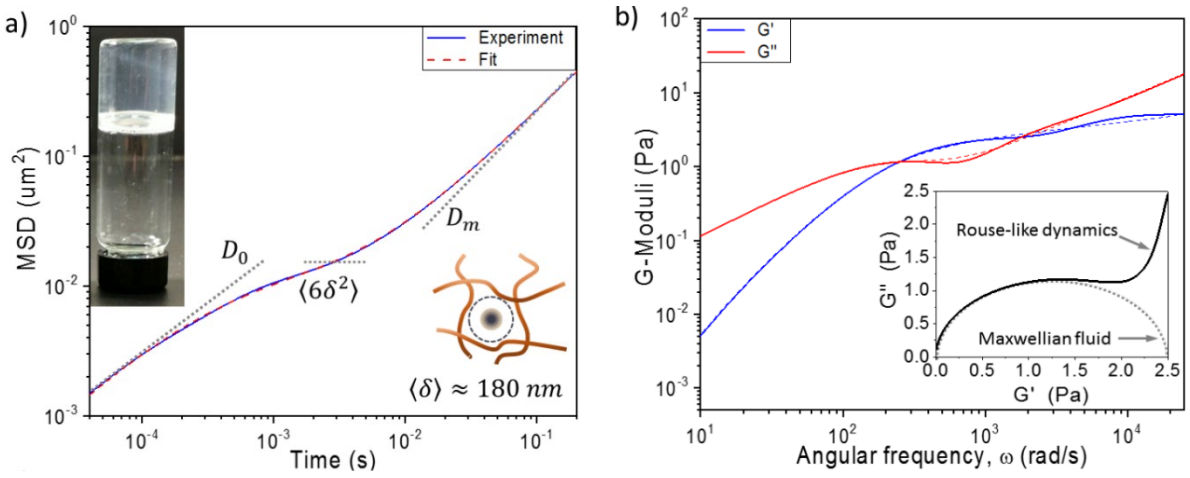

Figure 8. a) Temporal evolution of the MSD of the particles loaded into the hydrogel, calculated from the power spectra of intensity fluctuations. The inset shows a photography of NaDC hydrogel formed at pH ~7.0 in an upturned glass vial. b) Viscoelastic moduli of the hydrogel.

Fig. 8(b) shows the local viscoelastic properties of the hydrogel. As expected from the well-defined regions exhibited by the time evolution of the MSD, the viscous component dominates at both low and high frequency, $G''(\omega) > G'(\omega)$, i.e. at long and short times, respectively, while the elastic

component, which characterizes the probe's confinement, dominates in the intermediate range, $G'(\omega) > G''(\omega)$.

Important aspects to highlight are the following. First, in the present experiment the embedded probes are much smaller than tracers traditionally used in DWS-based microrheology. This is rather beneficial since the small particles will have only marginal influence on the naturally-forming structures i.e., cages of the polymer network. Also, from the frequency-dependent viscoelastic moduli (Fig. 8(b)), one can readily obtain characteristic values that are commonly used to describe gel-like dynamics i.e., crossing points at which $G'(\omega) = G''(\omega)$. Moreover, one can also identify the presence of more complex dynamics, as can be seen Cole-Cole representation in the inset of Fig. 8(b). In this representation, a purely Maxwellian fluid would be described as a semicircle. However, this system deviates from the semicircular behavior predicted by the single exponential stress relaxation decay typical of Maxwellian fluids, which is the fingerprint of Rouse-like dynamics related to the presence of both reptation and breaking of worm-like structures. Further details on the experiments and the interpretation of the results in the context of caging effects can be found in Ref. [52].

3.1.3 Dynamics of light-absorbing media

As mentioned before, an effective collection of singly-scattered light in the optically-isolated coherence volume allows measuring dynamics of complex media which are optically dense at macroscopic scales. We demonstrated this in two different situations of strong scattering – in the first case (highly concentrated colloids) the strong scattering results from the large concentration

of particulates; in the second case (gels), on the other hand, the macroscopic strong scattering results from the inherent structure of the medium itself, not from the tracer particles.

Nevertheless, besides scattering, absorption can also result in a large optical density due to the strong attenuation of light at macroscopic scales i.e., in the examples studied, the attenuation of light is perceived due to the photons are directed away from the direction in which the measurement is performed; in this case, due to they are absorbed. In practical applications, far-field-based measurements are severely limited by absorption; only some free-space low-coherence interferometers have been demonstrated to be suitable when both absorption and scattering are present [54-56]. However, if the small coherence volume is optically transparent, as demonstrated in the previous examples for the case of scattering, the absorption of light would also be negligible at the microscopic scales tested, as it will be demonstrated in this section.

Fig. 9 shows the hydrodynamic size measured in polystyrene colloidal suspensions (nominal size of 100 nm and 1 μm, respectively) of particles suspended in absorbing solvents consisting of liquid binary mixtures of water and commercial black ink. In this case, the samples were prepared with a constant concentration of particulates while the absorption in the solvent was varied with the concentration of the ink. No detectable particles were identified in the absorbing solvents alone.

The macroscopic situation is amply dominated by absorption, as verified by independent measurements of the absorption and extinction coefficients of aqueous solutions of ink and aqueous suspensions of particles in the absorbing solvents, respectively (Appendix C). In those measurements, it was found that the dependence of the absorption coefficient of the solvent, μ_a, as a function of concentration i.e., the molecular absorption function, is linear with the

concentration of ink. Therefore, a molecular absorption coefficient can be defined as $\mu_a(C) = 1.55\ mm^{-1}/wt\%$,. The meaning of this value is that, for instance, at a concentration of ink of C=10wt% the characteristic attenuation length is only of $l_a = \mu_a^{-1} \approx 60\ \mu m$, which is comparable to the coherence length of the broadband light sources used in our experiments. At larger concentrations of black ink (>10wt%), the measurement can still be performed regardless of the decrease in the fluctuating signal in the range $l_c \lesssim l_a$, however, a larger hydrodynamic size is retrieved due to a significant increase of the solvent's viscosity, as shown in Fig. 9.

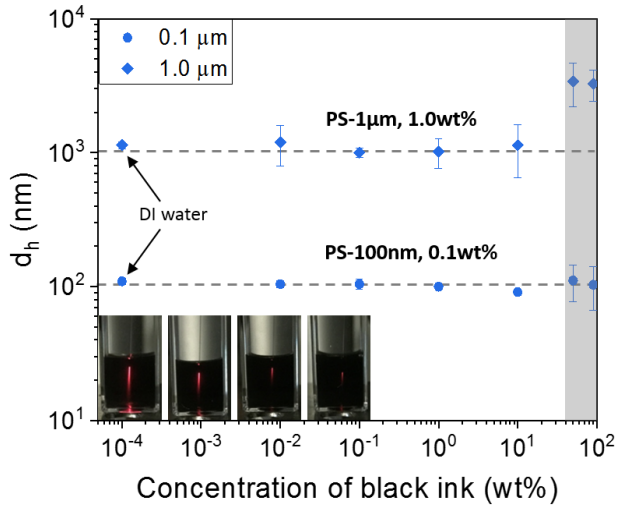

Figure 9. Hydrodynamic size measurements of particles suspended in absorbing solvent (aqueous solutions of black ink) with different levels of absorption. The shaded region indicates the concentration range for which the viscosity of the solvent is altered significantly.

We would like to note that with our coherence-gated DLS technique it can be possible to discriminate between whether the absorption comes from the medium or from the particles by means of a measurement based on a variable coherence length. As the coherence length is systematically increased, the amplitude of the power spectrum will decay in a linear fashion

(proportionally with the number of particles with the coherence volume) for absorbing particles or exponentially (Beer's law) for absorbing medium.

In this Section, we have shown that our coherence-gated DLS technique allows examining the complex fluids in a consistent manner with the same instrument, at the same irradiation power and, most importantly, regardless of the macroscopic optical properties of the sample. In the following sections, we will demonstrate the use of our technique in more challenging scenarios, which are more relevant to practical situations involving non-stationary dynamics and non-ergodic materials.

3.2 Time-evolving structural dynamics

An important aspect of our spatio-temporal coherence-gated DLS is its stability thanks to the fact that the phase noise between the reference and the scattered field is eliminated as a result of the common path configuration.

For dynamic systems slowly evolving in time, a description of the long-term dynamics can be pursued by a generalized time-frequency i.e., spectrogram, representation of the system's structural dynamics,

$$P(f,t) = \frac{2}{\pi}\sum_{i=1}^{N} \frac{a_i(t)/\tau_i(t)}{f^2+(1/\tau_i(t))^2}, \text{ with } \quad \sum_{i=1}^{N} a_i(t) = 1 \tag{24}$$

where a_i and τ_i are the relative amplitude and the characteristic relaxation time, respectively, of each Lorentzian component used in the decomposition of the power spectrum measured.

The collection of spectra in Eq. (12) can be used to describe the time-evolution of the spectral content of the light intensity fluctuations over time scales t much larger than the characteristic times associated with the power spectrum itself, as shown schematically in Fig. 10. In this way, our measurement can provide, simultaneously, both slow and fast dynamics which, in turn, allows accessing multi-scale dynamics with the same instrument.

The changes in the spectral content experienced over time can be readily associated to the evolution of the transport properties, $\langle \Delta r^2(t',t)\rangle = -\frac{6}{q^2} ln[\sum_{i=1}^{N} a_i(t) exp(-2\pi t'/\tau_i(t))]$, and these, in turn, to the time-evolving mechanical properties of the medium surrounding the probe particles, $|G^*(\omega,t)| \approx \frac{k_B T}{\pi a \langle \Delta r^2(1/\omega,t)\rangle \Gamma[1+\alpha(\omega,t)]}$ with $\alpha(\omega) = \frac{\partial ln\langle \Delta r^2(t',t)\rangle}{\partial ln(t')}\Big|_{t'=1/\omega}$.

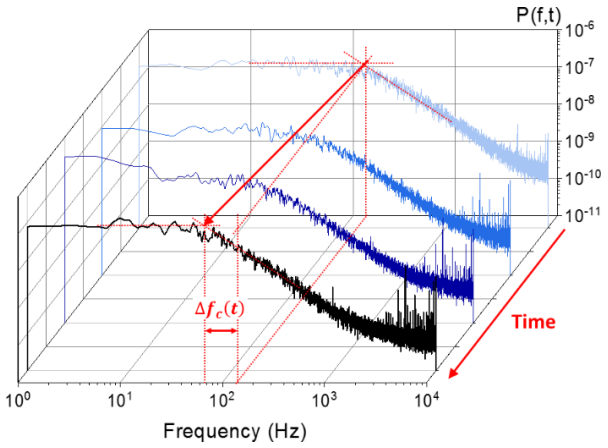

Figure 10. The time-evolving spectral content in the LC-DLS spectra relates to the evolution of the transport properties and changes in the mechanical properties of the complex medium.

In the following, we show that our technique can be used for the continuous monitoring structural dynamics in non-stationary, long-term processes. More specifically, we show measurements of i) colloidal dynamics in situations where both advection and diffusion are present e.g., biased diffusion due to sedimentation, ii) colloidal dynamics where in non-stationary solvents e.g., time-

dependent diffusion during solvent mixing, and iii) the time-evolving structural dynamics and viscoelastic properties of gels e.g., characterization of pH-driven, viscoelastic modulations of bio-compatible hydrogels.

3.2.1 Diffusive and advective dynamics

In this example, we highlight the spatially-resolved nature of our measurement and make use of one of the optical parameters that our technique allows accessing: the total energy in the power spectrum of the light intensity fluctuations, β, which provides information on the scattering density, $\beta \propto (\sigma N)^2$. More specifically, we show that one can perform spatially-resolved measurements of Brownian dynamics e.g., at different depths within the sample, while using β to visualize the sedimentation wave front [57].

In general, the particle dynamics in colloidal suspensions is a combination of Brownian, thermally activated motion, and additional advective components of motion due to external fields. A typical case is a colloidal system under the influence of gravity.

The specific dynamical regime of a colloidal system is characterized by the Péclet number (*Pe*), which quantifies the ratio between the diffusive and advective components with respect to the size of the suspended particles, $Pe = \frac{t_b}{t_s} = \frac{a v_g}{D_0}$, where v_g is in general the advective velocity and $D_0 = k_B T / 6\pi\mu_f a$ is the (Stokes-Einstein) diffusion constant for a particle with characteristic dimension a. For the specific case of gravity-driven colloids, v_g is the so-called free-settling (Stokes) velocity, $v_g = 2g(\rho_p - \rho_f)a^2/9\mu_f$. In these expressions, g is the gravity, ρ is the mass density of the

particle and fluid, respectively, a is the radius of the colloidal particle, μ_f is the dynamic viscosity of the fluid, k_B is the Boltzmann constant, and T is the absolute temperature.

Colloidal dynamics has been studied experimentally in detail in extreme regimes of primarily diffusive dynamics or advective transport i.e., $Pe \ll 1$ and $Pe \gg 1$, respectively. Intermediate regimes, however, are less well understood despite their relevance in applications where the phase behavior and the equilibrium density profiles play a major role for the colloidal stability. The challenges in these intermediate regimes, $Pe \approx 1$, are primarily experimental due to the time scales for diffusive and advective transport are comparable. Thus, neither of these contributions can be neglected and the colloidal dynamics is intrinsically non-stationary.

The complete characterization of colloidal dynamics at $Pe \approx 1$ requires measuring both the diffusive and the advective contributions. In the example of gravity-driven colloids, this implies knowing both the diffusivity and the sedimentation velocity.

Proof-of-concept experiments were performed on two different sedimenting colloidal systems consisting of 1 %wt concentrated aqueous suspensions of melamine and silica particles with nominal diameters of 1.0 μm ($Pe \approx 0.35$) and 0.7 μm ($Pe \approx 0.15$), respectively. At that concentration, the effect of hydrodynamic interactions is not considerable.

Fig. 11(a) shows the hydrodynamic size retrieved as sedimentation progresses, at a fixed depth of 3 mm below the air-liquid interface. The inset illustrates a typical example of an experimental spectrum and the corresponding fit to the multi-Lorentzian model (Eq. (12)). The averaged hydrodynamic sizes recovered over the entire duration of the measurement are indicated by the

dashed lines and are 1032.8 nm ± 13.7 nm and 675.6 nm ± 12.6 nm for melamine and silica, respectively.

It can also be seen that the hydrodynamic size decreases by the end of the measurement. This is the signature of the sedimentation wavefront, where the smaller particles are left behind the bigger ones. In other words, this feature could be used as an indication of how mono-disperse the population of particles is.

As mentioned before, $\beta \propto (\sigma N)^2$. In this case, the scattering cross-section, σ, remains invariant throughout the experiment since neither the refractive index contrast between the medium and the particles nor the size of the particles changes in time. Thus, $\beta(t)$ can be used as a direct measurement of the time-evolution of the number of particles in the coherence volume i.e., $\sqrt{\beta(t)} \propto N(t)$. At a fixed depth the number of particles is expected to remain invariant during certain time, due to the replenishing of the layers above, and then to progressively drop as the last layer of sedimenting particles leaves the coherence volume.

In Fig. 11(b) we show $\beta(t)$ for the melamine colloidal system when placing the fiber at different depths below the surface, as indicated. The inset shows the fit of $\beta(t)$ to general analytic expressions of the time-evolving particle number density profile [58], from where the mean free-settling velocity can be extracted given that the diffusion coefficient is measured independently (the sedimentation velocity is the only fitting parameter).

It should also be noticed that the fit shown in the inset of Fig. 11(b) for the evolution of the particle number density needs to include a narrow size distribution in order to relax the step-like behavior

of a monodisperse population that is characterized by a single sedimentation speed (dashed line in the inset of Fig. 11(b)).

We measured $\beta(t)$ at different depths, as indicated in Fig. 11(b). The retrieved mean free-settling velocities averaged over the different depths at which the measurements were performed (1-5 mm) are 0.29 µm/s ± 0.021 µm/s and 0.27 µm/s ± 0.026 µm/s for melamine and silica, respectively. The values retrieved are in good agreement with the theoretical estimates of 0.31 µm/s and 0.26 µm/s, respectively.

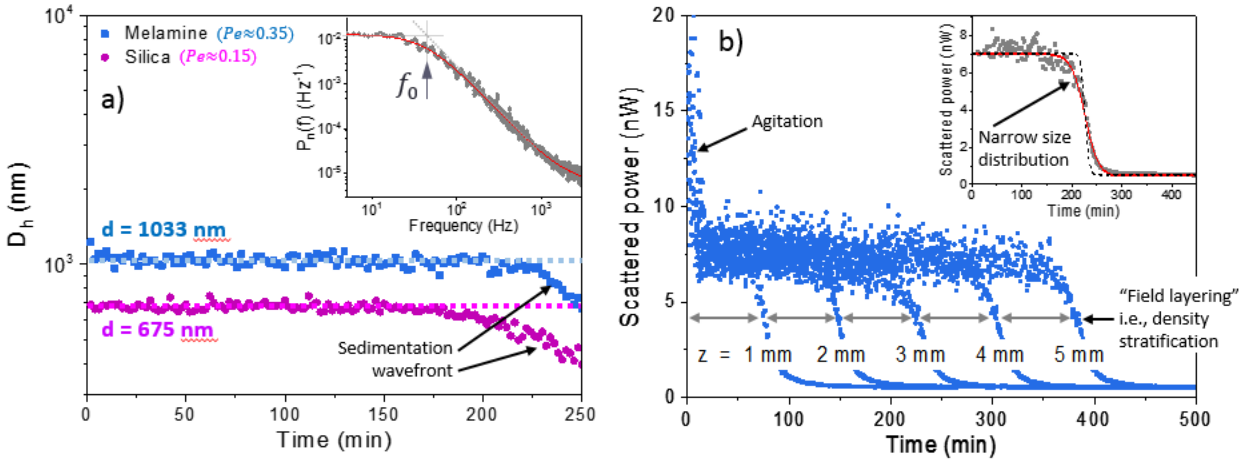

Figure 11. a) Hydrodynamic sizes retrieved for melamine and silica colloidal systems during the sedimentation process at a fixed depth of 3 mm below the air-liquid interface. The inset shows a typical multi-Lorentzian fit of experimental spectra. b) Total scattered power, β, measured during sedimentation at different depths, as indicated. $\beta(t)$ describes the temporal evolution of the particle number density within the coherence volume

Up to here, it is clear that a complete description of the dynamics of gravity-driven colloids in the presence of both advection and diffusion can be achieved thanks to the fact that those two components of motion are measured independently. More specifically, the particles' diffusion is measured from the characteristic correlation time of the intensity fluctuations while the sedimentation speed is measured from the time-evolution of the total scattered power.

However, one can do more by further exploiting the spatial resolution of our measurement. For instance, by performing spatially-resolved measurements of the sedimentation speed one can verify the linearity of the sedimentation process. In other words, one can verify whether or not the sedimentation speed varies with depth, which would be an indication of the 'layering' of the external field. In our particular examples, the sedimentation speed is independent of depth, as verified from the equal spacing between the curves in Fig. 10(b). However, in situations where the sedimenting particles are strongly coupled hydrodynamically [59-61], or when the solvent is inhomogeneous or structured e.g., stratified [62, 63], this is not the case. In those cases, the actual spatial distribution of the sedimentation speed can be retrieved with our technique thanks to the spatially-resolved nature of our measurement. In more general words, such a measurement could be used to verify the homogeneity of the advective action induced by an external field. Further details can be found in Ref. [57].

3.2.2 Diffusion at dissolving interfaces

In this experiment we take advantage of the stability of our coherence-gated DLS technique over long-term periods of time to continuously measure the diffusive transport properties of Brownian particles in the proximity to a liquid-liquid interface that progressively dissolves during a passive mixing process. As the liquid molecules diffuse during mixing, the system changes its local properties such as viscosity, density, and refractive index.

Our experiments are performed on model systems consisting of a binary mixture of fully miscible liquids in which an initially sharp liquid/liquid interface smears over time and eventually dissolves completely. The two liquids are pre-loaded with the same concentration of particles, such that the

nonstationarity arises only from the variations in the properties of the solvent. This is an extreme case of dynamics of a soft interface, which exhibits practically all possible configurations, from a sharp, well-defined interface at initial times to an extended, diffuse interface in advanced stages of the process. From a practical perspective, assessing the diffusive mass transport in a context like this is complicated due to the difference in the time scales of the dynamic processes that take place: the slow process of interface dissolution (hours) resulting from the fast diffusion of liquid molecules at the interface (nanoseconds).

We prepared our samples by first loading two different liquids, DI water and an aqueous solution of glycerol 50wt% concentrated, with the same concentration of silica beads (0.25 %vol; nominal diameter of 200 nm). This low concentration of tracers ensures a good signal-to-noise ratio in the scattering signal without affecting the natural inter diffusion of the liquids at the interface. After being loaded with particles, the liquids were carefully put in contact in a rectangular cuvette of 10 mm x 10 mm. The same amount (0.5 cm^3) of both fluids was added. Once in contact, the liquids were left to naturally mix without perturbations.

Two complementary experiments were performed. In the first experiment, the time evolution of the depth profile of the diffusion coefficient was measured. More specifically, $P(f, z; t)$ was recorded at different depths by vertically scanning the optical fiber across the column of liquid. This was done with a single optical fiber, and this profiling was performed at different moments during the mixing process. At each sample point two power spectra were recorded. From their average spectrum, the effective diffusion constant at that particular depth, $D_{eff}(z; t)$, was calculated.

Fig. 12(a) shows the time-evolution of the $D_{eff}(z;t)$ profile at different moments during the mixing process. The horizontal axis specifies the depth with respect to the air/liquid interface for a total height of the column of 10 mm. The dashed line indicates the step-like profile at the beginning of the process (t=0) for values of the diffusion coefficient of 200 nm particles in pure water (1.91 $\mu m^2/s$) and glycerol 50wt% (0.96 $\mu m^2/s$), respectively, at room temperature (20°C), which were calculated using the values of viscosity of similar binary mixtures reported in the literature [64].

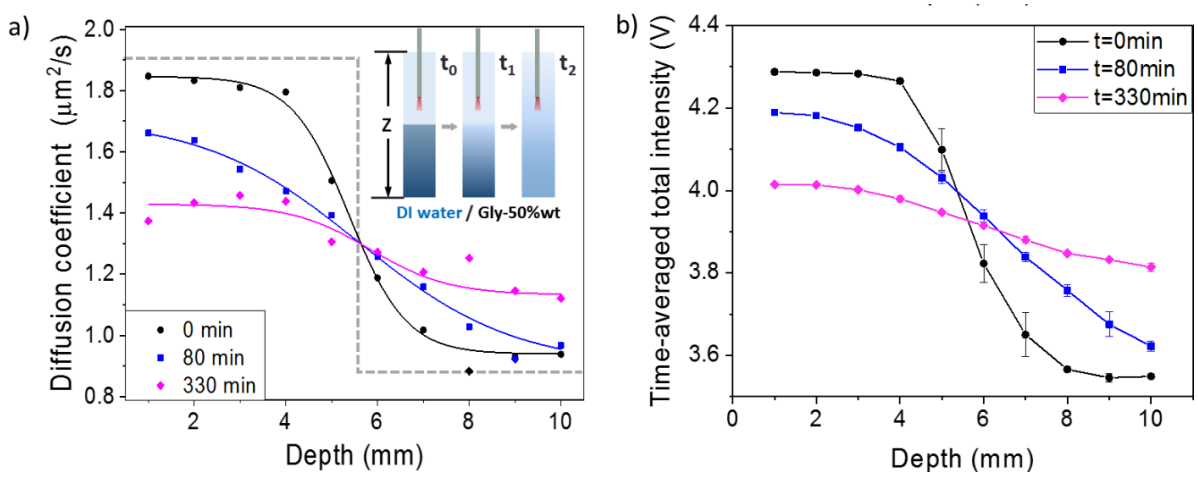

Figure 12. Depth-resolved profile of a) the diffusion constant of the probe tracers along the column of liquid as the liquid/liquid interface dissolves over time, and b) the total power measured, which encodes the Fresnel reflectivity at the fiber-medium interface.

Fig. 12(b) shows the total intensity detected which, as mentioned before, is mainly determined by the reference field and encodes information from the Fresnel reflectivity at the fiber-medium interface. It is important to note that, even though the trace of the curves in Fig. 12(a) and 12(b) is similar, they refer to two different aspects of the process and they were measured from two independent experimental parameters. More specifically, Fig. 12(a) provides a mechanical description i.e., viscosity of the solvent, while Fig. 12(b) provides an optical description i.e.,

effective refractive index of the solvent. In our particular example, the close resemblance simply verifies that the viscosity and the refractive index of the solvent vary together.

In the previous experiment, one could argue that the system is significantly perturbed due to scanning the fiber. In order to correct for this, one can alternatively perform a measurement in which the fiber is kept fixed at certain depth and the acquisition is done continuously throughout the entire process.

Fig. 13 shows the time evolution of the raw power spectra $P(f,t)$ recorded at two positions simultaneously. The fibers are located symmetrically 2 mm above and below the position of the interface, respectively. The system is similar than before i.e., DI water and an aqueous solution of glycerol 75wt% concentrated, with the same concentration of silica beads (0.25vol%) with a nominal diameter of 200 nm.

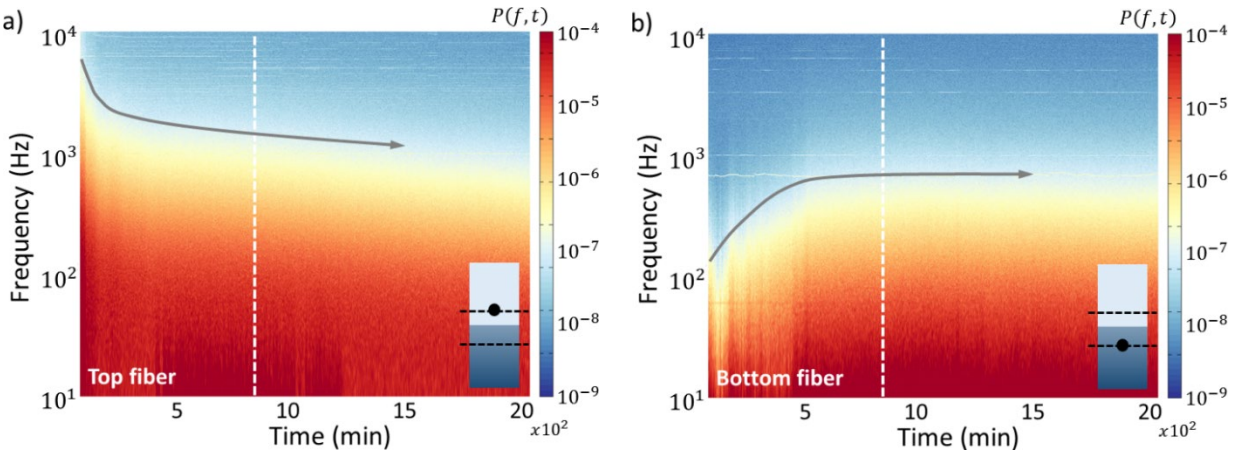

Figure 13. Temporal evolution of the power spectra recorded at fixed positions of 2 mm above and below the interface, respectively.

Fig. 14 shows the temporal evolution of $D_{eff}(t; z_0)$ at those particular depths. In our case, since the two liquids are fully miscible, the initial non-equilibrium configuration evolves to a single homogeneous state of thermodynamic equilibrium that is intermediate with respect to those of the two bulk fluids. Thus, the measurements at the two different locations to converge to the same final condition, as shown in Fig. 14. Given that the particle size is known, once can construct the evolution of the local effective viscosity from $D_{eff}(t; z_0)$ by following the Stokes-Einstein formulation, $D_{eff}(z,t) \propto \nu_{eff}^{-1}(z,t)$. At equilibrium, the diffusion profile reaches a constant value corresponding to the uniform fluid mixture. Notably, the measurements agree well with the theoretical predictions for isothermal mass transport in binary liquid mixtures driven solely by diffusion [65], which are indicated by the continuous lines in Fig. 14.

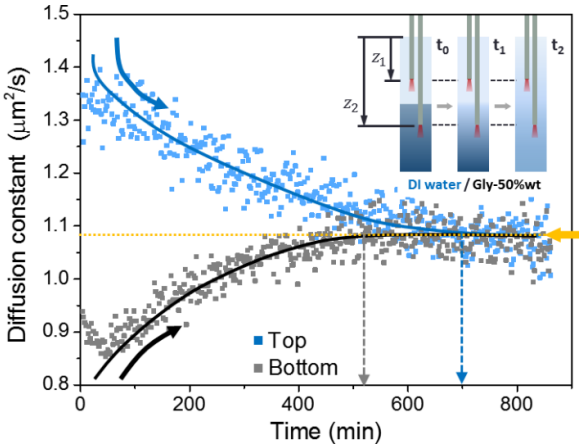

Figure 14. Temporal evolution of the effective diffusion constant at fixed positions of 2 mm above and below the interface, respectively.

The importance of this measurement relies in that the system's dynamics can be measured quantitatively at multiple time scales by imposing the existence of an intermediate time scale that connects the others. This is done by loading known Brownian tracers and following the evolution of their thermally-activated diffusion. In this way, the slow dynamic of the interface is followed

continuously over hours while the fast transport of the liquid molecules can be inferred from the instantaneous, effective viscosity experienced by the probe particles at each moment in time.

Additionally, one can notice that the final state of equilibrium above and below the interface is reached at different times, as indicated by the dashed arrows in Fig. 14.

The mixing process is due to the diffusion of the molecules in the bulk fluids across an initially well-defined interface. This scenario can be examined in close analogy to the diffusive carrier transport across a p-n junction. In that case, the associated diffusion constant of the carriers depends on their mobility, $D \sim \mu$, which, in turn, is inversely proportional to the effective mass, $\mu \sim m_{eff}^{-1}$ [66]. In our particular case, one can simply think of the bulk fluids to be composed of diffusing molecules with different mobility. The ratio of the molecular diffusion coefficients or, equivalently, the ratio of the particles' mobility, can be determined by the ratio of the effective masses which, in our case, is equivalent to the ratio of the bulk densities. In our measurement, this ratio can be estimated as the time is takes to reach equilibrium above and below the interface. From Fig. 14, the ratio of those times (~ 1.3) is close to the ratio of the densities of the bulk fluids ($\rho_{gly,75wt\%} / \rho_{water} \approx 1.2$) [64]. The variability can be due to a small error in positioning the fibers with the respect to the interface.

3.2.3 Dynamics in confined geometries: drying colloidal droplets

In the previous examples, we measured the non-stationary dynamics of time-evolving colloids. In the first example, the colloidal suspension evolves due to the sedimentation of the particles i.e., due to particle density fluctuations, while the solvent remains unaltered. Conversely, in the second

example, the evolution of the system results from the mixing process in the suspending medium i.e., due to solvent viscosity fluctuations, while the particles density remains unaffected. Nevertheless, in both cases the systems are open in the sense that, for the purpose of our measurement, they are boundary-less.

In this Section, we demonstrate the use of spatiotemporal coherence-gated DLS in situations where the boundaries of a finite size complex medium actually influence the dynamics measured at the microscopic scales tested. Specifically, we focus on the non-stationary internal dynamics of drying colloidal droplets, where practically all the elements of the system (the particle number density, the viscosity of the solvent, and the extent and influence of the boundaries) change over time.

In this context, we would like to spend more time to contextualize our work properly because our implementation actually alleviates some of the technical challenges of the current technology as it allows for a measurement that is non-contact, non-invasive, and label-free, and permits real-time observations of both optical and mechanical changes in the measurement volume.

Colloidal droplets are essential to a wide range of applications such as, for instance, forensics and diagnostics based on biological fluids [67, 68]; micro-organisms and cellular separation [69]; the development of new materials like three-dimensional photonic crystals [70], hierarchically porous films and scaffolds [71, 72], or energy-sustainable devices with enhanced thermal transport properties [73]; chemical and biological assays using so-called droplet reactors [74, 75]. In spite of that, the vast majority of characterization techniques are applicable only during the preparation stages of the bulk nanofluids [76]. One possible reason for this can be that measuring the internal dynamics of these systems is not an easy task because all the cohesive and adhesive interactions

involved i.e., substrate-fluid, substrate-particle, particle-fluid, and particle-particle, play a major role for both the process and the outcome.

Being essentially a mass-transfer phenomenon, droplet evaporation could be described by a simple differential weighting approach or, alternatively, by following the temporal evolution of some feature of the droplet morphology [77]. However, there are many other aspects associated to this phenomenon which are of interest. For instance, the study of the dynamics particularly at the droplet-substrate interface during evaporation is commonly approached by spectroscopic measurements of electrical impedance, by laying the colloidal droplet on a surface containing electrodes while the conductance and capacitance is continuously monitored [78]. Conversely, if the interest is on studying the evaporation of the droplet alone, without the influence of the substrate, one can perform evaporation experiments on acoustically-levitated droplets [79, 80].

In situations where the evaporation process is to be studied under more 'natural' conditions, optical measurements are preferred due to their potential noninvasiveness. For instance, the temperature distribution across the droplet during evaporation has been assessed by means of infrared thermometry [81], infrared time-resolved spectroscopy [82], Raman spectroscopy [83, 84], and so-called laser-induced fluorescence thermometry [85, 86], where the droplet is loaded with temperature-sensitive fluorescent dyes and the temperature is indirectly monitored through the intensity of the fluorescence light.

Other optical techniques monitor the evolution of the droplet size as evaporation progresses. For this purpose, approaches such as interferometric imaging [87] or the so-called phase rainbow refractometry [88] are used, where the size is inferred from the changes in the angular spreading

of quasi-monochromatic light due to the variations in the droplet's curvature. Sometimes, several of these techniques are combined together for a more detailed characterization [89].

In some other cases, one could be interested in the internal dynamics of the droplet. Unfortunately, there exist only a few reports addressing this issue, especially regarding the movement of the particulate components inside the droplet. For such purpose, particle tracking-based approaches i.e., particle image velocimetry [90, 91], can be used but are limited to situations where the colloidal droplet is dilute (transparent) and the suspended particles are sufficiently large. Some implementations have been improved to construct, for instance, both the particles' velocity and concentration fields, by using particles of different sizes that can fluoresce in different channels [92, 93]. The tracking resolution can be further enhanced using variants of dark field microscopy [94]. The main drawback of all these approaches is that they are limited to examine colloidal droplets in which the suspended particles serve only the purpose measurement beacons. In other words, the characteristics of the particles embedded into the droplets, e.g., size, concentration, or fluorescence emission, have to be carefully chosen such that the measurement can be optimally performed. This limits severely the composition of the droplets that can be examined [92, 93]. As a result the information about the micro-scale dynamics during nanoparticles evaporation is still limited and it has to be either simulated numerically [77, 95, 96] or inferred from dry deposition patterns at the end of the drying process [67-75].

We use a similar implementation to that explained in detail in Chapter II. Similarly, the portion of the dynamic field that is scattered by the complex system, which in this case is the colloidal droplet, $E^{(s)}(t)$, can be measured through the heterodyne amplification resulting from its interference with

a (static) reference field, $E^{(r)}$ [45, 46]. In usual circumstances, as explained in the previous sections, the local oscillator results from the inherent Fresnel reflection at the end-facet of the fiber. Here, by using a refractive index matching layer, we axially displace the coherence volume away from the facet of the MMF into the droplet. The new interface from where $E^{(r)}$ is generated is that between the colloidal droplet and the substrate on which the droplet sits i.e., the picolitter-sized coherence volume is located at the droplet-substrate interface.. This allows a contact-less measurement of the internal dynamics of the colloidal droplet by examining the signal collected from a coherence volume that is located at the base of the droplet, as illustrated in Fig. 15.

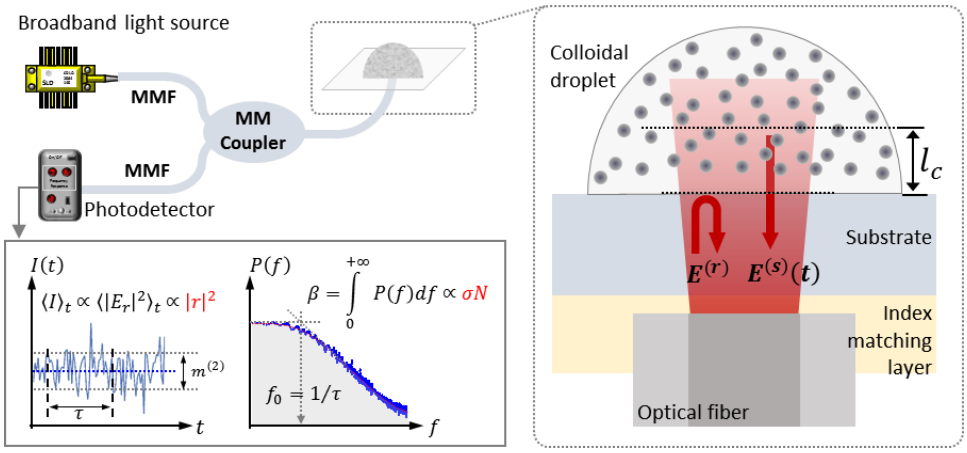

Figure 15. Schematic of the fiber-based, multimode common-path interferometer used to measure the internal dynamics of colloidal droplets

In all cases we used colloidal droplets of 50 µL consisting of aqueous suspensions of polystyrene particles (ThermoFisher; nominal size of 330 nm and deviation ≤ 3%). The particle concentration of the colloidal suspensions was adjusted by diluting a small sample of the original batch with de-ionized water. The diluted samples were gently agitated by hand and then sonicated with ultrasound for 2 min to achieve complete homogenization. The colloidal droplets were deposited on standard square cover glasses (Fisher Scientific 12-540-B; 200 µm thickness), which were

previously cleaned sequentially with acetone, methanol, and isopropanol; then, they were rinsed with de-ionized water and, finally, dried slowly with compressed air. No further surface treatment was implemented to modify the inherent wetting properties of the glass surface.

The droplets were let to evaporate naturally on an uncovered cover glass that was open to the ambient of the laboratory, at room temperature (21-22°C). In our evaporation experiments, the only free parameter was the particle concentration; both the particle size and material were kept invariant. The concentration range (<0.2wt%) considered in our experiments was chosen to work with diluted colloids that exhibit negligible hydrodynamic interactions in bulk, thus allowing us to assess the confinement effects in comparison to conditions where inter-particle interactions are practically absent. In all cases, the fiber was positioned at the center of the droplet and the process was followed during its entire duration i.e., until the droplet dried completely. Once in place, the optical fiber was kept fixed throughout the entire duration of the measurement.

In a series of proof-of-concept experiments, the power spectra of light intensity fluctuations, $P(f)$, were recorded in the frequency range from 1 Hz to 10 kHz with a resolution of 1 Hz and integration time of 60 s (one sample spectrum per minute). Fig. 16 shows all the parameters followed in our measurement for the particular case of a colloidal droplet with an initial concentration of 0.1wt%. Fig. 16(a) shows the collection of raw spectra recorded, $P(f,t)$; each vertical line in the color map represents one power spectrum, $P(f;t_0)$. Fig. 16(b)-(d) show the total intensity detected, the total scattered power, $\beta = \int P(f)df$, and the effective hydrodynamic size (diameter) of the diffusing particles, respectively.

Importantly, in our measurements the drying process is slow and the influence of the internal flows is not captured, at least in the time scales of our measurement. More specifically, we verified that in all cases $P(f,t)$ has essentially a single-Lorentzian shape, which indicates the diffusive motion of a monodisperse population of particles in a Newtonian solvent with an increased effective viscosity.

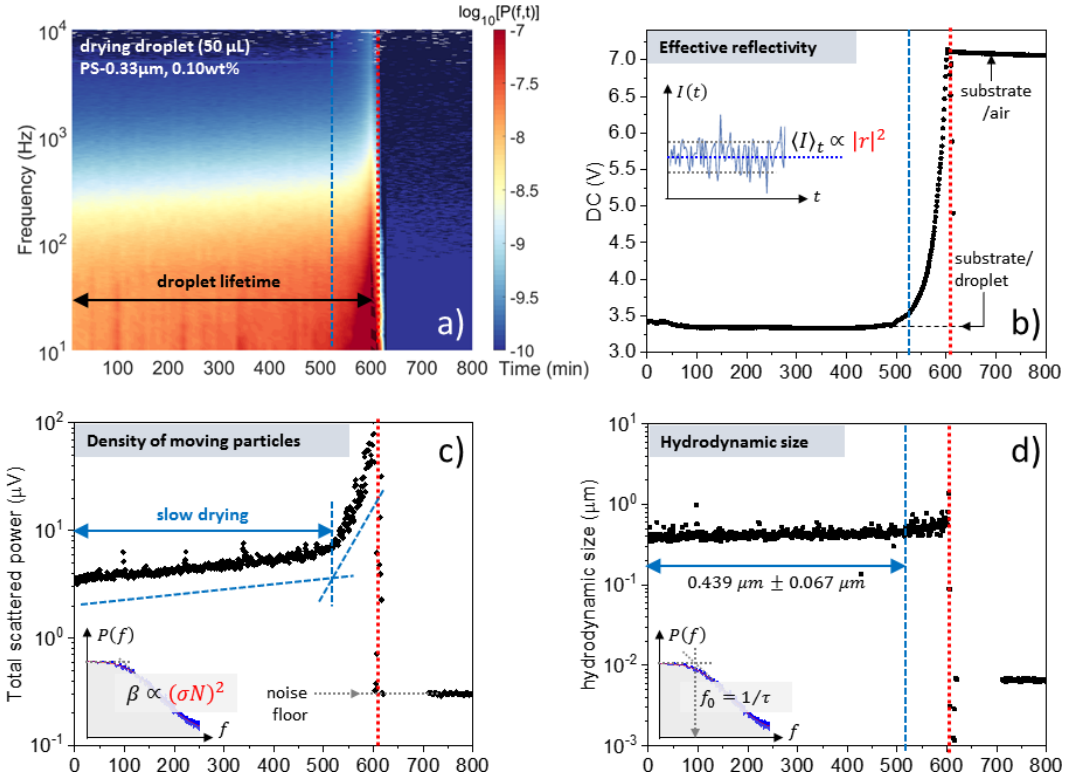

Figure 16. Temporal evolution of the a) raw power spectra, b) the total intensity, c) the total power scattered (total power in the power spectrum, β), and d) the hydrodynamic size of the suspended particles, for a drying colloidal droplet (50uL) of PS particles (nominal size of 330 nm, 0.10wt%). The schematics in the insets illustrate the different aspects of the signal measured, from where the information is retrieved

As can be seen in Fig. 16(b), the total intensity measured remains almost invariant for most of the measurement until a sharp transition occurs close to complete drying. This transition takes place when the boundaries of the droplet i.e., droplet-air interface, are 'seen' and they contribute to

increase the refractive index mismatch between the fiber and the complex medium thus reflecting more light. In other words, for most of the experiments the fiber 'sees' mostly water with suspended particles and by the end of the measurement, when the maximum reflectivity is reached, the fiber 'sees' air with a layer of particles deposited on the substrate.

The total drying time can be clearly identified in all the parameters followed. Importantly, in the absence of moving particles only the spectrum of the noise in the detection system can be recorded (Fig. 16(a)) and, consequently, the total scattered power drastically reduces to the noise level, as seen in Fig. 16(c). Since the scattering cross-section, σ, of the particles remains constant throughout the evaporation process, the time evolution of $\beta \propto (\sigma N)^2$ reflects the slow growing of the number of particles within the observation volume ($N \propto \sqrt{\beta}$) which, at least in the region of 'slow' drying, can be used as an estimate of the rate of volume reduction of the droplet i.e., $\dot{V} \propto -\dot{N}$. In this measurement, one can also identify a region of 'fast' drying towards the end of the process. Finally, the total power in the dynamical signal drops to the noise level once the colloidal system has dried (Fig. 16(c)).

It is also important to note that the effective hydrodynamic diameter measured (Fig. 16(d)) is significantly larger than the nominal size of the particles (by a factor of 1.3 for a concentration of 0.1wt% (Fig. 16(d)). Recall that, in the concentration range of our experiments, those colloids exhibit negligible hydrodynamic interactions in bulk. Thus, the fact that an effectively increased hydrodynamic size is measured with respect to that expected for free-diffusion is indicative of the interactions in such conditions of confinement that overall result in a reduced diffusion coefficient.

We emphasize that our measurement is microscopic in nature, and consequently the information retrieved is local, since the optical signal is collected from an optically isolated, picolitter-sized volume much smaller than the droplet's volume.

We further examined these effects in experiments where the concentration was varied. The lifetime of 50 μL droplets with different concentration of particulates is shown in Fig 17(a). From the known initial droplet volume, V, and the measured droplet lifetime, t_d, one can estimate the pressure rate (the average rate of evaporative mass transfer of the solvent), $(-\dot{m}) \approx \rho V/t_d$, as indicated in Fig. 17(a), where ρ and V are the effective density of the droplet and its initial volume, respectively [97].

Furthermore, by knowing the initial droplet radius, r, one can also estimate the initial drying speed, $U_i \sim r/t_d$, and also the average evaporative mass loss per unit area of substrate surface (evaporative mass flux), $J_{avg} \approx (-\dot{m})/(\pi r^2)$ [97]. In our case, the droplets have a diameter of ~5 mm (5.2 mm at a concentration of 0.05wt%, which corresponds to the intermediate concentration of the range explored). The diameter was measured by rapidly scanning the optical fiber across the droplet at the beginning of the experiment. The boundaries of the droplet's base can be clearly identified by the increase in the reflected power due to the larger refractive index mismatch at glass/air interface (similar to that observed in Fig. 17(b)). Since we used polystyrene particles, the suspensions can be assumed to be density-matched i.e., $\rho \approx 1 mg/mL$. This leads to characteristic initial drying speed and evaporative mass flux in the range $U_i \approx 4 - 5\ \mu m/min$ and $J_{avg} \approx 3.6 - 4.6\ (\mu g/min)/mm^2$, respectively. We note that V and r can also provide additional initial macroscopic quantities of the droplet such as the contact angle, the drop surface (liquid-vapor

surface area), and the drop profile e.g., by assuming a spherical cap-shaped droplet and neglecting gravitational flattening [98, 99].

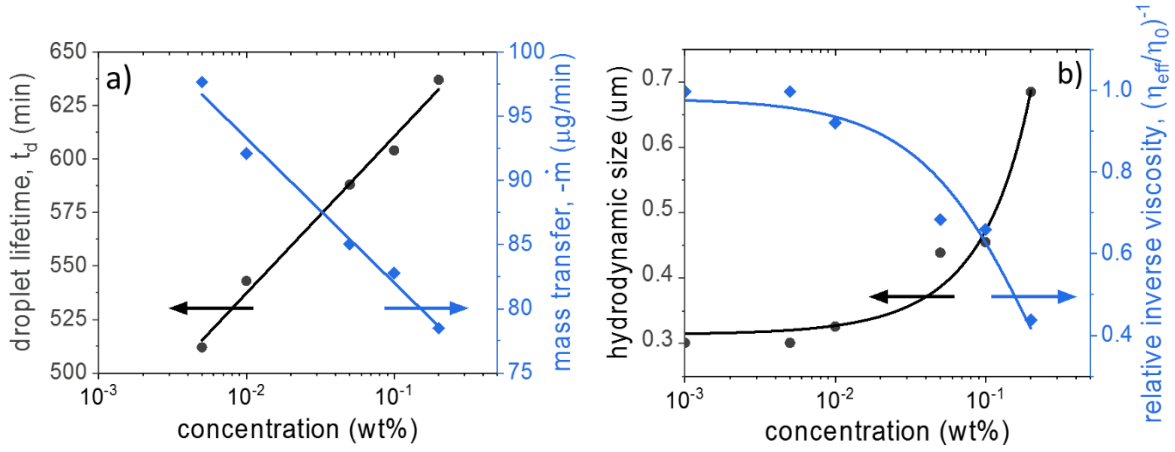

Figure 17. a) Drying time and b) effective hydrodynamic size for colloidal droplets (50uL in all cases) of PS particles (nominal size of 330 nm) with different concentrations.

A summary of the hydrodynamic size retrieved at the beginning of the drying process is shown in Fig 17(b). At this early stage, the system is in quasi-thermodynamic equilibrium but evolves in a confined geometry where an increased hydrodynamic drag at the boundaries slow down the particles diffusion as compared to the estimates based on Stokes-Einstein relation [100-102]. Importantly, as we mentioned before, if the same colloids were measured in boundary-less conditions, these hydrodynamic interactions would be negligible, as the particles are more than ten diameters apart even at the largest concentration [103].

The progressive increase of the droplet lifetime or, equivalently, the decrease of the evaporative mass transfer, $(-\dot{m})^{-1}$, relates to the so-called self-pinning capabilities, which basically describe the reduction of the average speed at which the triple line recedes by the inclusion of nanoparticles in the solvent [98, 104-107]. This process can also be regarded as an increase of the effective liquid viscosity [98, 108]. In fact, this apparent increased in viscosity, which is a macroscopic descriptor

of the entire droplet, can be estimated from the measured values of the diffusion coefficient. The relative effective viscosity can be calculated as the ratio of the diffusion coefficient measured inside the droplet and the theoretical one in the solvent alone (water), $\eta_{eff}/\eta_0 = D_{eff}/D_0$, as indicated in the secondary axis of Fig. 17(b).

We note that the macroscopic parameters retrieved, which are 1) the average rate of evaporative mass transfer of the solvent, $-\dot{m}$ (Fig. 17(a)), and 2) the relative inverse effective viscosity, $\left(\eta_{eff}\right)^{-1}$ (Fig. 17(b)), were retrieved directly from our microscopic measurements and did not require an assumption on a specific morphological model. Specifically, $-\dot{m}$ is retrieved from the droplet lifetime, while $\left(\eta_{eff}\right)^{-1}$ is retrieved from the effective diffusion coefficient measured.

By using the inverse of the effective viscosity one can also estimate the drying speed as $\frac{dr}{dt} = \dot{r_{eff}} \propto \frac{\gamma\theta(t)}{6\eta}[cos\theta_0 - cos\theta(t)] \sim \left(\eta_{eff}\right)^{-1}$ [98, 108]. Moreover, using the same pieces of information, one can also evaluate the relative rate of radius evolution of the droplet (average speed of triple line recession) with respect to that of the solvent alone, $\eta_{eff}/\eta_0 = \left(\frac{\dot{r_{eff}}}{\dot{r_0}}\right)^{-1}$ [98, 108].

The fact that D_{eff} measured is larger than D_0 is indicative of the interactions that overall result in a reduced diffusion coefficient. In its more general form, the diffusion coefficient can be connected to the chemical potential [109, 110], or, alternatively, to the osmotic pressure [111] or the static structure factor [112]. Nevertheless, an interpretation of D_{eff} in terms of specific type of potentials is pertinent to a particular situation, and it requires imposing both the structure of the individual particles (hard or soft spheres) and the necessary boundary conditions at the surface of the spheres e.g., sticky [109], mixed slip-stick [111], or charged boundaries [113].

In closing this section, we would like to emphasize the versatility and practicality of our approach as well as to highlight some unique features. First, the coherent scattering interrogation is performed at the distal end of an endoscopic-like probe from a picolitter-sized volume that is optically isolated by using optical fibers in conjuncture with low-coherence radiation. This coherence volume can be optically transferred, by means of a proper refractive index-matching, from the end facet of the fiber to the inside of colloidal droplets thus allowing to measure the droplet internal dynamics. Additionally, our implementation in a common-path interferometer configuration allows performing noninvasive, contactless, label-free measurements continuously over the entire duration of the long-term process.

Regarding the information retrieval, one can measure, simultaneously, two different physical properties namely the internal diffusion dynamics and the effective optical parameters, which are not available in traditional approaches. When all of these parameters are followed in time, a description of the evolution of the particles' dynamics and accumulation can be pursued including the overall resultant of the adhesive and cohesive interactions that take place in such conditions of confinement. Moreover, we have also demonstrated that some important macroscopic descriptors of the drying process, which include, for instance, the average drying speed, the rate of evaporative mass transfer, and the time evolution of the droplet volume, can be estimated from the continuous measurement of these microscopic properties.

Finally, our fiber-based implementation can be incorporated into existing characterization platforms such as drop profiling setups, including the ones based on the tracking florescent particles [92, 93], dark field microscopy [94], or approaches where droplets are pinned on pillars in order to speed up reaction assays [74, 75]. The spatially-resolved nature of an optical fiber-

based instrumentation makes it possible to characterize even more complex situations where the solvent is either viscoelastic and/or heterogeneous [114], or to study other dynamical aspects such as internal flows in conditions of quasi-stabilized evaporation [96].

3.3 Non-ergodic structural evolution

3.3.1 Overcoming non-ergodicity

The non-equivalence between time and ensemble averages i.e., non-ergodicity, in the context of a DLS experiment means that the intensity correlation function (ICF) measured cannot be interpreted in terms of ensemble-averaged properties of the medium [115]. In the measurements, typical manifestations of non-ergodic phenomena take place when a sufficient range of possible system's configurations is not explored. Common situations occur in glassy colloids and polymer gels [116-122], and heterogeneous, dense soft systems in general [123-130]. Prominent examples in biology include the intracellular transport in the cytoplasm, cellular transport in the extracellular matrix and plasma membranes, and dynamics of blood [131-139]. In such complex media, the non-ergodicity is due to temporary localization of diffusion about mean positions and the globally slow structural dynamics.

Non-ergodicity is even more critical when dealing with non-stationary processes when the time window available for measurements is limited by the process itself. In some cases, where long-

term time averaging is not possible but the process is spatially stationary, one can still achieve a proper ensemble average by simultaneously measuring at multiple spatial locations.

Nevertheless, the experimental difficulty for ensuring the operation in an ergodic regime relies in that there is not a clear and sharp threshold for when these effects start affecting the measurement. In fact, both the time scales for integration and the number of different spatial locations required to mitigate non-ergodicity largely differs depending not only on the dynamic characteristics of the sample but also on the specific mechanism implemented e.g., static light scattering (SLS) plus DLS [115], direct averaging (translational/rotational motion of the sample) [140], monitoring the temporal evolution of multiple speckles [141-143], or a 'non-ergodic to ergodic conversion' by cascading additional dynamic media [144].

In our case, where long-term, non-stationary dynamic process are to be followed, sufficiently long observations of temporal changes are not practical since the integration time must be kept short in order to properly describe the global evolution of the system from its microscopic characteristics. Thus, the only option for proper ensemble-averaging is the evaluation of the system's dynamics at multiple locations.

It was explained before that our technique can be described as a parallel heterodyne detection, at multiple independent and self-referenced locations, of the scattered field $E_s(t)$ using the local oscillator provided by E_r [23-25]. This parallel sampling of the system allows measuring the structural dynamics averaged over a large number of spatial configurations of the complex medium and, therefore, to effectively mitigate its possibly non-ergodic behavior.

We tested this on a standard system that typically exhibits non-ergodic dynamics: particle-loaded, bio-compatible hydrogels. Fig. 18 shows the power spectra measured from probe particles loaded into a polymer network for different averaging times. Briefly, the system consists of polystyrene particles with nominal diameter of 100 nm, loaded into a 1wt% chitosan hydrogel [145]. The thin curves show all the samples acquired during 20 min in all cases, and the thick curves show the resulting averaged spectra (averaged over all the curves).

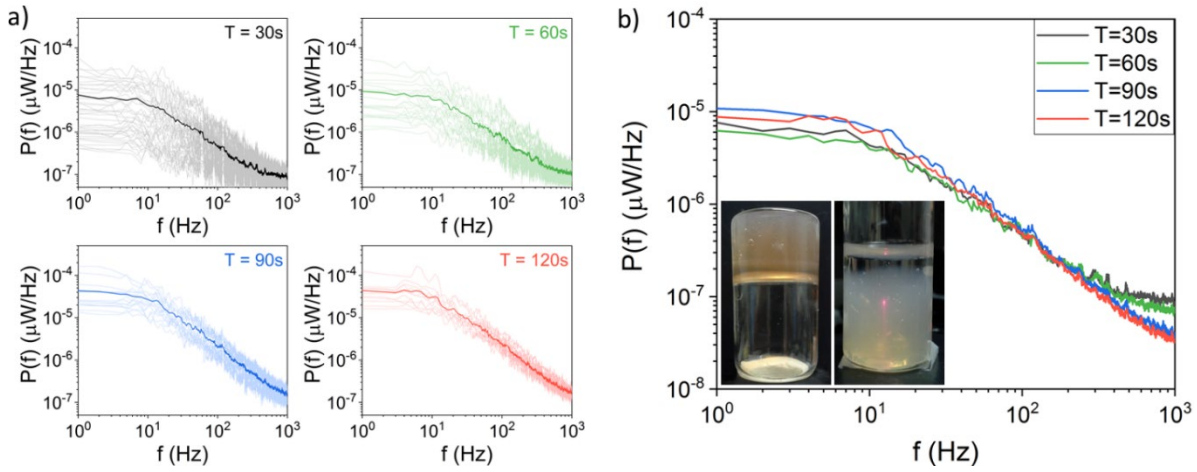

Figure 18. a) Raw power spectra measured from probe particles loaded into a hydrogel for different integration times (30 s, 60 s, 90 s, and 120 s), as indicated. b) Averaged power spectra for the different integration times. For visualization purposes the curves for 60 s, 90 s, and 120 s where divided by a factor of 1.5, 3.5, and 5, respectively. The system consists of polystyrene particles with nominal diameter of 100 nm, loaded into a 1wt% chitosan hydrogel.

It can be clearly appreciated that shorter integration time results in noisier measurements. This larger variation of the signal measured results in that the noise floor of the detection system is approached over a larger frequency range, as can be clearly seen in Fig. 18(a). Nevertheless, the shape of the power spectrum measured is similar irrespective of the integration time used to average, as shown in Fig. 18(b). This indicates that the spatial averaging provided by sampling at multiple locations was indeed effective and produced a proper ensemble averaging [144]. In other

words, that the parallelized spatial averaging allows overcoming the non-ergodic nature of the dynamic process. A more detailed discussion on non-ergodicity in light scattering-based measurements can be found in Ref. [36], and in the Appendix B.

Thus, the simultaneous implementation of spatial and temporal coherence gates, together with the heterodyne amplification of the scattered field, results in that long-term processes can be continuously followed over their entire duration, without changing neither the hardware nor the data processing, while the time-evolving structural dynamics and local mechanical properties of the medium can be reliably retrieved [44, 146]. In addition, the large collection area of the MMF results in a high sensitivity, which in turn allows performing these measurements based only on intrinsic scattering, i.e. without the need of auxiliary scattering centers [39], or with a very small concentration of probe particles, as in the present case. For instance, we were able to study in detail the swelling properties of the same hydrogels used in Section 3.1.2, at different experimental conditions including the polymer concentration, the amount of binding sites, and the particle network interactions [44].

3.3.2 Viscoelastic modulations in hydrogels

In the following we demonstrate that the unique features in our approach can be useful to disclose more complex dynamics, both structural and micro-rheological, that could not be measured otherwise. Specifically, we show the measurement of pH-driven viscoelastic modulation in chitosan-based biocompatible hydrogels [147].

In the experiments, the power spectra of light intensity fluctuations were recorded in the frequency range from 10^0 Hz to 10^4 Hz with a resolution of 1 Hz and integration time of 120 s (one power spectra every two mins). Fig. 19(a)-(b) shows the time-evolution of the raw spectra and the frequency-averaged loss tangent, $\overline{\gamma(t)} = \langle G''(\omega;t)/G'(\omega;t)\rangle_\omega$, respectively, during a full cycle of swelling, contraction, and recovery of the hydrogel in which the modulation of its viscoelastic properties is induced by varying the environmental pH. The blue arrow (Fig. 19(b)) indicates the time at which 2 mL water with pH 5.7 was added on the top of the 1wt% and 2wt% CS hydrogels, in order to induce their swelling. After swelling saturates, 0.5 mL of water with pH 2.0 was added on the top of the 1wt% and 2wt% swollen CS hydrogels, as indicated by the red arrow.

The initial and final states of these two hydrogels are similar, as indicated by the magnitude of $\bar{\gamma}$. However, the 1wt% CS hydrogel undergoes an additional contraction-expansion i.e., stiffening-softening, transition. It is important to note that this transition would have gone unnoticed if the process had not been followed continuously and the measurement had been performed only at static points where the hydrogel is at equilibrium, as it is commonly done in measurements of relative weight after adsorption or release [148, 149]. This transition reveals the capability of the 1wt% CS hydrogel to undergo viscoelastic modulations, which occur at a constant polymer mass content while the integrity of the hydrogel remains unaffected, as shown in the inset of Fig. 19(c).

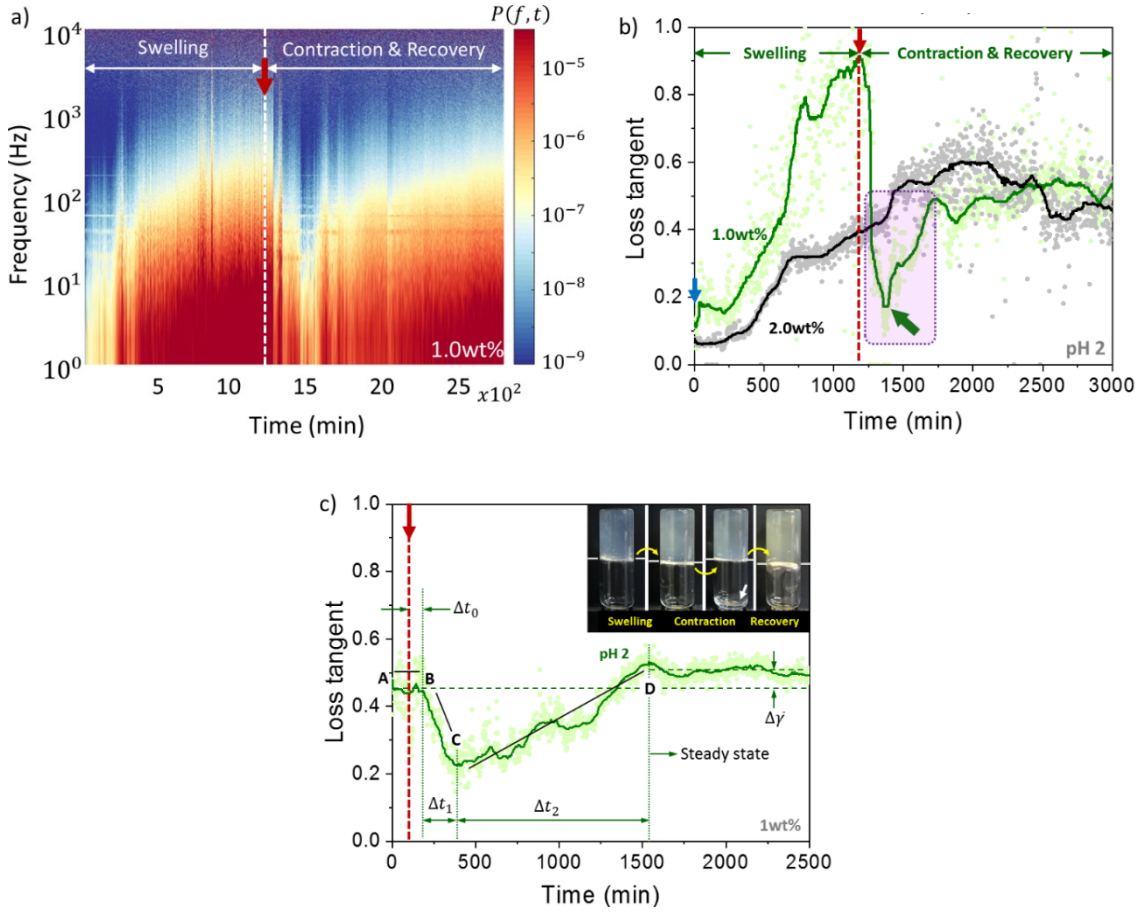

Figure 19. Time evolution of a) the power spectra and b) the loss tangent for a full swelling-recovery cycle for 1wt% and 2wt% CS hydrogels. The intermediate compression-expansion transition identified for the particular case of the 1wt% hydrogel is highlighted. c) Detailed characterization of the intermediate transition: time evolution of the loss tangent of swollen 1wt% CS hydrogel after the addition of water with pH 2 at the time indicated by the red arrow. The inset in c) shows photographs of the hydrogel at different stages where the process was temporarily interrupted

We were also able to study that intermediate stiffening-softening transition in more detail, by starting from swollen 1wt% CS hydrogels and inducing different pH-driven modulations. Fig. 19(c) shows the time evolution of the loss tangent of those swollen 1wt% CS hydrogels after the addition of HNO_3 solution with pH 2.0, at the time indicated by the red arrow.

Several stages of the process can be clearly identified, which also correspond to those shown in the inset of Fig. 19(c). First, there is a steady response (from point A to B), from which the delay

in the response of the hydrogel (at the particular depth where the fiber sits, 7mm in this case) can be measured, $\Delta t_0 \approx 180$ min. Then, the hydrogel undergoes the intermediate stiffening-softening transition from point B to C ($\Delta t_1 \approx 200$ min; stiffening), and then from C to D ($\Delta t_2 \approx 1{,}150$ min; recovery (softening) between by the re-absorption of the water previously released. Finally, the hydrogel reaches a steady state 23 hours after the addition of the addition of HNO_3 solution with pH 2.0 (point D). The steady state is slightly softer, as indicated by the value of the loss tangent at the end of the whole process. However, the similarity between those states suggests that the hydrogel goes back to a similar condition after a full cycle of viscoelastic modulations. Further details can be found in interactions [44, 147].

3.3.3 Blood: optically-dense, non-stationary, and non-ergodic medium

Up to this point, we addressed the issues of the optical density, the non-stationarity, and the non-ergodicity of the complex media separately. In this section we carry out studies of the structural dynamics and viscoelastic properties of the most prominent biological fluid – blood –, which is actually an optically-dense, non-stationary, and non-ergodic medium.

In a variety of clinical settings, inability to precisely and continuously measure and effectively manage the coagulation status can be cause of catastrophic thrombosis and hemorrhage, often leading to death, despite using “adequate anticoagulation therapies”. Such settings include, for instance, cardiovascular surgery requiring cardiopulmonary bypass (CPB), any major surgery in patients with coagulation disorders, extracorporeal life support, catheter-based interventional procedures, hemodialysis, and other acute medical conditions affecting clotting and coagulation, [150-152].

In this regard, optical methods have proved to capture some aspects of whole blood coagulation in the context of end-point measurements [153, 154]. Practical implementations, however, are restricted not only because of multiple scattering or strong attenuation typically encountered in optically dense media but also because of the inability to properly account for the non-ergodic nature of the slow dynamics in soft matter [115]. The main limitation of this and other recent approaches is that, even though these approaches can operate on whole blood, all of them are also based on end-point measurements. This requires a sample to be collected and sometimes prepared to induce coagulation under specific conditions and, after the measurement, the sample has to be disposed. Consequently, these approaches cannot provide real-time information hemostatic potential of the blood. A detailed discussion can be found in the Appendix E.

As a clinical problem, we chose to focus on CPB for several reasons. First, CPB results in coagulation activation that is reproducible and can be used to study the system regulation, Second, CPB is an important clinical tool used in the treatment of heart disease that has significant risk. Finally, new drugs and technologies are being developed to reduce coagulation activation however their measurement and precise mechanisms of action are still debated.

Among the number of different blood coagulation assays, some of which are conventional laboratory tests, only a few of them e.g., ACT and TEG, are well-stablished standards in the operation rooms. This is the case mainly due to the fact that most laboratory assays are in general labor intensive, expensive, and require repeated withdrawal of blood from the circuit. Moreover, the process of getting a readout from most laboratory assays can take a long time (several hours) which makes them impractical during surgical procedures. Even in the case of ACT and TEG, the tests are run only intermittently resulting in typical time gaps of at least 15-30 minutes. This time

gaps are determined by (i) the inherent end-point nature of the measurements (until full coagulation is reached) and (ii) the operation room logistics that aim at minimizing the exposure of the circuit to contamination due to sample withdrawal. During these time gaps, the precise status of blood coagulability is unknown. This is exactly what our approach can correct. By implementing mechanisms that prevent non-ergodic effects it is possible to keep the measurement time short such that a real-time feedback can be provided to the medical team during surgical procedures.

Specifically, we demonstrate that the coagulability condition of blood can be monitored in real-time, continuously, and directly in the operating room during a real clinical procedure. This is achieved without collecting samples, without special preparation procedures, without externally triggering the coagulation cascade. Thus, our procedure eliminates the time gaps associated with conventional technologies based on end-point measurements

In a first stage, a systematic study has been conducted in clinical setting as follows, in order to validate the use of our technique. Specifically, we demonstrate that different coagulations states can be clearly discriminated. Ten infants (mean age 4.08±1.64 months, all weighting <10 kg) were included in the study. Blood samples were obtained before and after CPB. Standard coagulation tests were performed according to clinical protocol. In all cases, full systemic anticoagulation before CPB was achieved by the administration of heparin and its effects reversed with protamine at CPB offset. The light scattering-based measurements were performed at four time-points: Pre-CPB before heparin administration, Pre-CPB after heparin administration, Post-CPB before protamine administration, and Post-CPB after protamine administration. These stages cover a full cycle of the coagulation status of blood, i.e. a “viscoelastic hysteresis”, that starts from a condition of normal coagulation (baseline), then is taken to a state of full anticoagulation that has to be

maintained at all times during the surgical procedure including CPB, and is finally reversed back to normal coagulation, as shown schematically in Fig. 20(a). These measurements were correlated with measurements of activated clotting time (ACT), which were performed simultaneously. This study was approved by both the UCF and the Orlando Health Institutional Review Boards. We obtained informed consent from all patients.

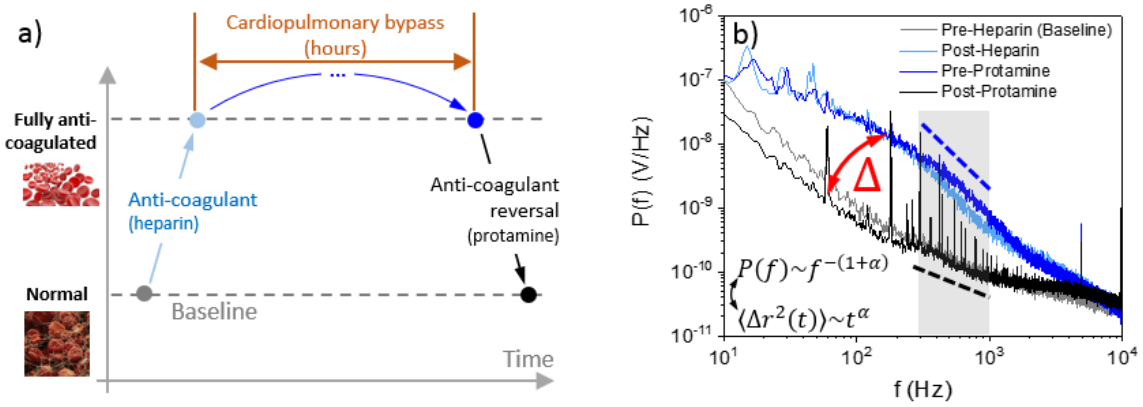

Figure 20. a) Schematic representation of the viscoelastic hysteresis of blood experienced during cardiovascular surgery. A safe level of anti-coagulation is to be maintained during the cardiopulmonary bypass. b) Typical power spectral densities of signal fluctuations corresponding to scattering from whole blood at different stages during cardiovascular surgery measured with spatio-temporal coherence-gated dynamic light scattering.

Fig. 20(b) illustrates typical power spectra corresponding to scattering from whole blood at different stages during the cardiovascular surgery. Those stages correspond to the data points shown schematically in Fig. 20(a). The effect of the anticoagulant is evident. The spectral amplitudes corresponding to heparinized blood are significantly larger indicating that the red blood cells are less impeded in their mechanical vibrations. It is also worth noting the time gap between the Pre-CPB and Post-CPB measurements (blue curves), which is the duration of the CPB (typically > 90 min). It is between these two stages where a tight, continuous assessment of the condition of blood is required in order to maintain a safe level of anti-coagulation to prevent

clotting. Having similar spectra before and after CPB is a good indication that the status of full anticoagulation was maintained throughout the procedure. Finally, the effect of the anticoagulant reversal can be verified as blood is brought back to the initial state of normal coagulation (black curve in Fig. 20(b)).

From a Brownian diffusion analysis, it can be estimated that a typical RBC explores <1% of its own size in the frequency range $>10^2$ Hz. Being limited at high frequencies by the noise floor in the detection system and by potential flow effects at the lower ones, we have restricted our analysis to the frequency range from 10^2 Hz to 10^3 Hz (shaded region in Fig. 20(b)). Linear regression analysis was used to assess the correlation of log-slope measurements with the standard tests at all time-points (as defined above). Within the frequency window of interest, the log-slope of $P(f)$ shows moderate, statistically significant correlation with the standard coagulation tests individually (PLT: $r = 0.53$, $p = 0.01$; ACT: $r = -0.39$, $p = 0.005$; TEG-CI: $r = 0.57$, $p = 0.009$). These values of the univariate correlations are acceptable from the medical standpoint as verified at Arnold Palmer Hospital for Children (APHC).

We have also determined the correlation between the incremental time-point differences of the log-slope and the ACT. We found that the incremental time-point differences of our measurement shows strong, statistically significant correlation (r=-0.76, p=0.0001), as can be seen in Fig. 21. Further details on both the statistical analysis of the data and how our correlation results compare to other studies can be found in the *Supplementary Materials* of Ref. [36].

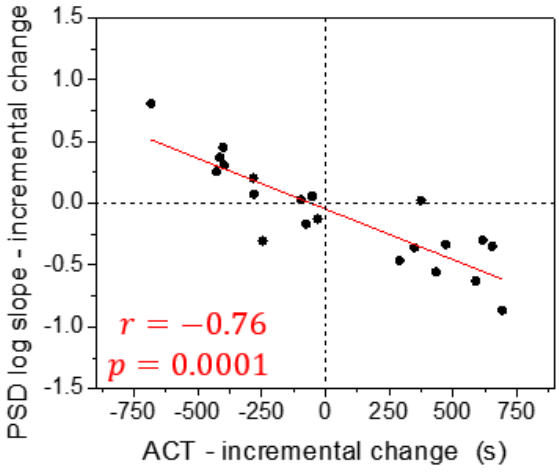

Figure 21. Linear regression of incremental time-point differences of the log-slope and the ACT showing the strong, statistically significant correlation between our measurement and the standard coagulation test ACT.

The all-fiber realization of the spatio-temporal coherence-gated dynamic light scattering technique presented here operates in a common path interferometer configuration in reflection. This constitutes a robust and reliable sensing technology with an endoscopic design that allows for direct incorporation into standard vascular access devices which, in turn, permits the instrumentation of blood circulation equipment used in the operation room for the in-line assessment of coagulation status during cardiovascular surgery, as shown in the Fig. 22.

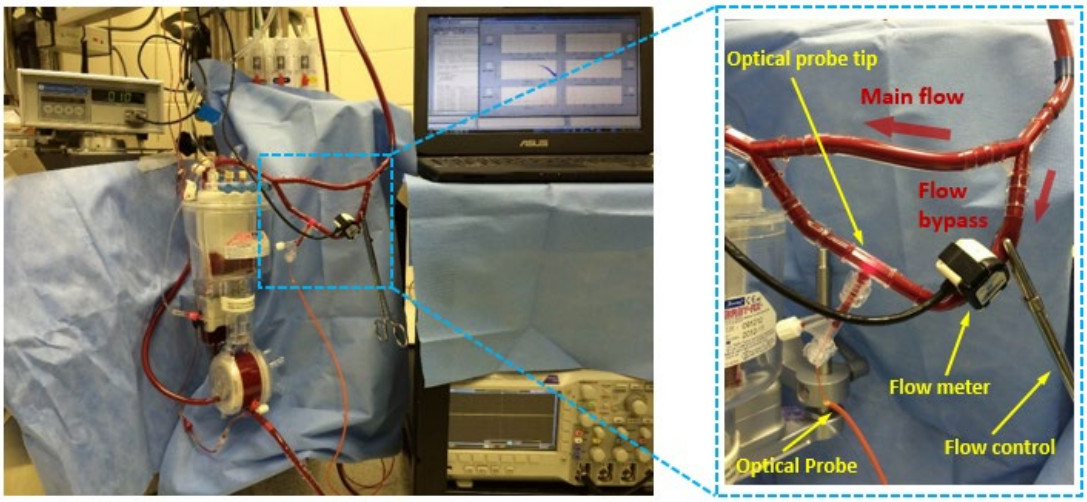

Figure 22. Instrumentation of blood circulation equipment for the in-line assessment of blood coagulability is possible thanks all-fiber realization of the spatio-temporal coherence-gated dynamic light scattering technique.

Fig. 23 illustrates some examples of typical collections of time-evolving power spectra acquired during CPB in cardiovascular surgery. The condition of whole blood is monitored continuously *in vivo, in situ* throughout the CPB without the need for sample collection or any other preparation. Important features such as heparin administration and variations at CPB offset are also captured by our technique.

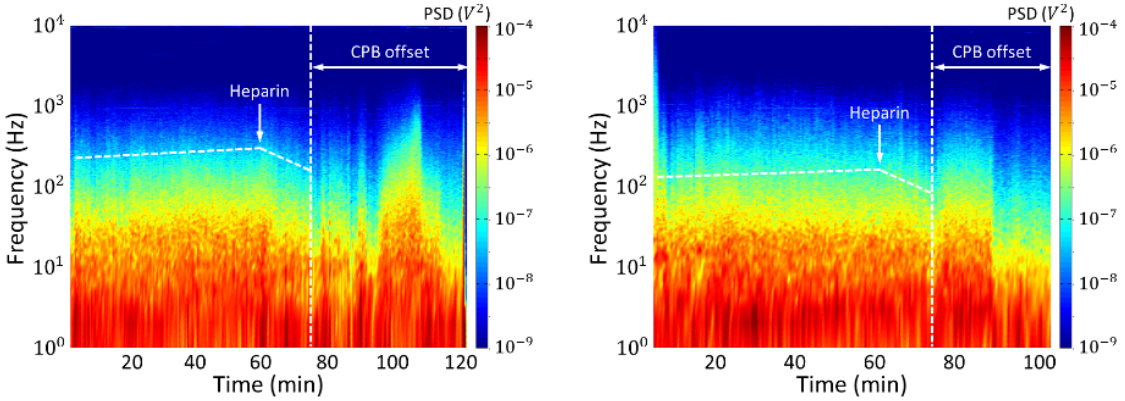

Figure 23. Typical example of the time-evolution of the power spectra measured continuously with spatio-temporal coherence-gated DLS during CPB (several hours), for different patients in the pilot study carried out at APHC.

In summarizing this Section, our spatio-temporal coherence-gated approach permits a clear discrimination between different conditions of blood during cardiovascular surgery and shows strong correlation with standard coagulation tests. Moreover, the all-fiber implementation allows direct incorporation into standard vascular access devices for the instrumentation of blood circulation equipment with minor modifications to the circulation equipment and minimal invasion to the operation room. The real-time measurement capabilities demonstrated here constitute a paradigm shift in blood monitoring as they provide real-time feedback and allow timely interventions and effective anticoagulation management during clinical procedures. Ongoing work addresses the development of suitable rheological models to describe the microscopic viscoelastic properties measured in our experiments and to identify relevant clinical events during CPB.

CHAPTER IV: CONCLUSIONS

In closing, we would like to comment on the versatility of our fiber-based implementation of the spatio-temporal coherence-gated DLS technique and to highlight some of the unique features that enable measurements that go beyond the capabilities of traditional DLS.

In our approach, the coherent scattering is collected at the distal end of an endoscopic-like probe from a picolitter-sized volume that is optically isolated by the use of low-coherence radiation. The single-scattering component of the signal that is coupled back to the fiber is amplified by the interference with a local oscillator that arises naturally at the end facet of the fiber due to inherent Fresnel reflections. This interferometric operation in a common-path geometry provides a high sensitivity in detecting to weak scattered fields. Additionally, the use of multimode fibers allows working with spatially partially coherent fields, which provides means for proper ensemble averaging.

Moreover, our technique offers access, in addition to diffusion dynamics, to optical parameters that are not available in traditional DLS. These parameters – the total time-averaged power and the total scattered power – provide information about the Fresnel reflection at the fiber-medium interface and the scattering density, respectively. As a result, one has access to a complete, mechanical and optical, characterization of the medium tested.

We presented several practical examples that rely on the unique features of our technique including (i) the effective isolation of single scattering, (ii) the large sensitivity and high collection efficiency, (iii) the capability to operate over a wide range of optical regimes, and (iv) the ability

to provide an efficient ensemble averaging. We have shown that these characteristics permit a detailed description of the local structural and micro-rheological properties of complex, inhomogeneous media in conditions of strong scattering and noisy backgrounds. The examples presented in this paper include applications of both statistically-stationary and time-evolving complex media and included particle sizing in optically dense systems, micro-rheology of gel-like materials, simultaneous measurement of diffusive and advective dynamics of colloids, diffusion and dissolving dynamics of liquid interfaces, the dynamics of non-ergodic colloids, and the viscoelastic evolution of bio-compatible hydrogels.

Finally, we would like to mention that the above-listed applications are examples where the unique characteristics of our technique can be clearly identified. Other applications may include the passive optical mapping of polymer assemblies [39], or the *in-situ*, *in-vivo* assessment of blood coagulability during cardiovascular surgery without the need of samples collection and end-point measurements [55] or any other scenarios that involve following the dynamics of optically inhomogeneous media.

APPENDIX A: DERIVATION OF THE INTER-CHANNEL COMMUNICATION IN SPECKLE FIELDS

Spatio-temporal coherence-gated dynamic light scattering can be thought as the (temporal) partially coherent interference of two (spatial partially coherent) speckle fields, one being the field reflected at the end facet of the multimode fiber $E^{(r)}(t)$ (reference) and the other the field scattered from the system under study $E^{(s)}(t)$.

The interaction between the reference and scattered field is three-dimensionally gated by the field distribution used for illumination i.e. spatial partially coherent speckle field, coherent only within the extent of each speckle (across the facet of the fiber), and the spectral properties of the light source. The interference between these two fields is controlled by the temporal coherence of the incident radiation i.e. partial temporal coherence leads to a finite depth in which the two fields maintain a phase relation, as illustrated in Fig. A1.

This situation is similar to the addition of correlated speckle fields for the particular case in which their correlation is limited to take place only within the extent of the coherence length [23] or, equivalently, as the heterodyne amplification of a scattered field, with a local oscillator of the same frequency, at multiple, independent spatial locations in parallel [24, 25].

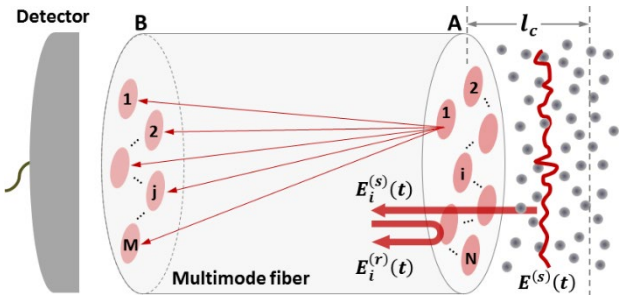

Figure A1. Fiber-based three-dimensional implementation of the spatio-temporal coherence-gated dynamic light scattering. Non-ergodicity is effectively overcome by sampling the scattered field at multiple, independent locations of self-reference illumination.

The scattered electric field can interfere with the reference field only at each location of independent illumination i.e. at each speckle. The total field at the end facet of the fiber (location A) is the coherent addition i.e. on a field or amplitude basis, of the reference and scattered field:

$$E^A(t) = \sum_i^N E_i^{(r)}(t) + E_i^{(s)}(t) \tag{A1}$$

In this context, it is well known that the coherent addition of speckle fields i.e. on an amplitude basis, does not reduce the contrast of speckle and has no effect on the signal-to-noise ratio i.e. the addition of two random fields on an amplitude basis simply results on a third random field distribution with statistics indistinguishable from the original ones [26, 27]. Based on this idea, the multimode fiber can be thought to be a black box that transfers the field distribution $E^A(t)$ into a new field distribution $E^B(t)$ on the other end.

For a loss-less system (same total power at both MMF ends) and without any special cross-channel interaction between the two ends, the inter-channel communication will lead to a uniform contribution from all the i-th locations on the A-side onto all the j-th locations on the B-side such that the total field at a single j location on the B-side is:

$$E_j^B(t) = \frac{1}{\sqrt{N}} \sum_i^N E_i^{(r)}(t) + E_i^{(s)}(t) \tag{A2}$$

In their more general form, the reference and scattered fields at the i-th location i.e. at each speckle, can be written as:

$$E_i^{(r)}(t) = \varepsilon_i^{(r)}(t) e^{-j\left[\omega_r t - \phi_i^{(r)}(t)\right]} \tag{A3a}$$

$$E_i^{(s)}(t) = \varepsilon_i^{(s)}(t) e^{-j\left[\omega_s t - \phi_i^{(s)}(t)\right]} \tag{A3b}$$

In this general form one can recognize the notation typically used for the heterodyne technique in radar applications in which the local oscillator has different frequency than the signal that is to be amplified [24, 25]. For our particular case the optical frequency of both the local oscillator and the scattered field are the same i.e. $\omega_r = \omega_s = \omega$.

The electric field cannot be measured at optical frequencies and only the slowly-varying envelope can be followed. Moreover, since it is only the relative phases what contain the information of the relation between the two fields, the rapidly-varying oscillations can be removed from the previous expressions:

$$E_i^{(r)}(t) = \varepsilon_i^{(r)}(t) \tag{A4a}$$

$$E_i^{(s)}(t) = \varepsilon_i^{(s)}(t)e^{-j\phi_i(t)} \tag{A4b}$$

where $\phi_i(t) = \phi_i^{(r)}(t) - \phi_i^{(s)}(t)$. If the field amplitudes are assumed to be approximately constant over time and only the time-varying phase $\phi_i(t)$ is considered, the previous definitions of the fields simplify to:

$$E_i^{(r)}(t) = E_i^{(r)} = \varepsilon_i^{(r)} \tag{A5a}$$

$$E_i^{(s)}(t) = \varepsilon_i^{(s)}e^{-j\phi_i(t)} \tag{A5b}$$

The total intensity right behind the end facet of the fiber on the A-side is the incoherent addition i.e. on an intensity basis, of the intensity contributions from at all i-locations. At each of this locations, the local intensity is the coherent addition i.e. on a field basis, of the reference and scattered field such that:

$$I^A(t) = \sum_i^N \left| \varepsilon_i^{(r)} + \varepsilon_i^{(s)} e^{-j\phi_i(t)} \right|^2 \tag{A6}$$

On the B-side the situation is similar in the sense that at this end the field distribution is also a spatially incoherent speckle field such that the total intensity is given by the intensity contribution from all j locations:

$$I^B(t) = \sum_j^M I_j^B(t) \tag{A7}$$

with the difference that now, as mentioned before, the local intensity at the j-th location contains contributions from all the i-locations on the A-side:

$$I_j^B(t) = \left| \frac{1}{\sqrt{N}} \sum_i^N \varepsilon_i^{(r)} + \varepsilon_i^{(r)} e^{-j\phi_i(t)} \right|^2 \tag{A8}$$

Such that the total intensity on the B-side is given by:

$$I^B(t) = \sum_j^M I_j^B(t) = \sum_j^M \left| \frac{1}{\sqrt{N}} \sum_i^N \varepsilon_i^{(r)} + \varepsilon_i^{(r)} e^{-j\phi_i(t)} \right|^2 \tag{A9}$$

Appealing to the above-mentioned energy conservation argument, the total integrated power should be the same at both ends of the multimode fiber. In other words, the total intensity at both ands A and B is the same i.e. $I^A(t) = I^B(t)$. This can be verified by expanding the sums as follows:

$$I^A(t) = \sum_i^N \left| \varepsilon_i^{(r)} + \varepsilon_i^{(s)} e^{-j\phi_i(t)} \right|^2 = \sum_i^N \varepsilon_i^{2\,(r)} + \varepsilon_i^{2\,(s)} + 2\varepsilon_i^{(r)} \varepsilon_i^{(s)} Re\left\{ e^{-j\phi_i(t)} \right\} \tag{A10}$$

If the amplitude of the electric fields is considered to be roughly the same at all locations i.e. $\varepsilon_i^{(r)} = \varepsilon^{(r)}$ and $\varepsilon_i^{(s)} = \varepsilon^{(s)}$, the expression above simplifies to:

$$I^A(t) = N\left(\varepsilon^{2\,(r)} + \varepsilon^{2\,(s)} \right) + 2\varepsilon^{(r)} \varepsilon^{(r)} \sum_i^N Re\left\{ e^{-j\phi_i(t)} \right\} \tag{A11}$$

Doing the same on the B-side, the intensity at a single j-location (see Eq. (8)) is:

$$I_j^B(t) = \frac{1}{N}\sum_{i,k}^{N} \varepsilon_i^{(r)}\varepsilon_k^{(r)} + \varepsilon_i^{(r)}\varepsilon_k^{(s)}e^{+j\phi_k(t)} + \varepsilon_k^{(r)}\varepsilon_i^{(s)}e^{-j\phi_i(t)} + \varepsilon_i^{(s)}\varepsilon_k^{(s)}e^{-j[\phi_i(t)-\phi_k(t)]} \quad \text{(A12)}$$

Which can be expressed in terms of two sums representing the interactions at the same location and the cross-interactions between two spatial locations:

$$I_j^B(t) = \frac{1}{N}\sum_{i}^{N} \varepsilon_i^{2\,(r)} + \varepsilon_i^{2\,(s)} + 2\varepsilon_i^{(r)}\varepsilon_i^{(s)}Re\{e^{-j\phi_i(t)}\} + \frac{1}{N}\sum_{i\neq k}^{N} \varepsilon_i^{(r)}\varepsilon_k^{(r)} + \varepsilon_i^{(r)}\varepsilon_k^{(s)}e^{+j\phi_k(t)} +$$
$$\varepsilon_k^{(r)}\varepsilon_i^{(s)}e^{-j\phi_i(t)} + \varepsilon_i^{(s)}\varepsilon_k^{(s)}e^{-j[\phi_i(t)-\phi_k(t)]} \quad \text{(A13)}$$

From this expression it can be seen that the first term is already the same obtained for the intensity on the A side.

The second term contains different contributions. The first contribution, $\varepsilon_i^{(r)}\varepsilon_k^{(r)}$, represents the self-interaction of the reference field at two different spatial locations. This interaction is forbidden simply due to the spatial partially coherent nature of the reference field i.e. self-interaction takes place only within the extent of a single speckle.

The second and third contribution, $\varepsilon_i^{(r)}\varepsilon_k^{(s)}e^{+j\phi_k(t)}$ and $\varepsilon_k^{(r)}\varepsilon_i^{(s)}e^{-j\phi_i(t)}$, represent the interaction between the reference field at certain location and the scattered field at a different location. This interaction can also be forbidden if the scattered field is locked to interact only with its corresponding reference field at the same location. This implies that, given a short coherence length, the scattered field from each discrete location does not diffract enough to contribute to several speckles simultaneously such that each speckle 'sees' only what is front of it i.e. back scattering within a relatively narrow angle.

The last contribution, $\varepsilon_i^{(s)}\varepsilon_k^{(s)}e^{-j[\phi_i(t)-\phi_k(t)]}$, represents the self-interaction of the scattered field at two different spatial locations. This interaction could be thought to be forbidden if one considers the scattered field to be also spatial partially coherent due to the nature of illumination. However, in general, this term cannot be neglected due to possible spatial correlations in the wavefront of the scattered field. The fact that the scattered field comes from an optically isolated picolitter-sized volume leads to the assumption that the amplitude of the reference field is much larger than the amplitude of the scattered field i.e. $\varepsilon_i^{(r)} \gg \varepsilon_i^{(s)}$, such that this last contribution can also be neglected.

Summarizing the above-listed observations, the whole second sum can be neglected:

$$I_j^B(t) = \frac{1}{N}\sum_i^N \varepsilon_i^{2\,(r)} + \varepsilon_i^{2\,(s)} + 2\varepsilon_i^{(r)}\varepsilon_i^{(s)} Re\left\{e^{-j\phi_i(t)}\right\} \tag{A14}$$

If again the amplitude of the electric fields is considered to be roughly the same at all locations i.e. $\varepsilon_i^{(r)} = \varepsilon^{(r)}$ and $\varepsilon_i^{(s)} = \varepsilon^{(s)}$, the expression above simplifies to:

$$I_j^B(t) = \left(\varepsilon^{2\,(r)} + \varepsilon^{2\,(s)}\right) + \frac{1}{N}2\varepsilon^{(r)}\varepsilon^{(r)}\sum_i^N Re\left\{e^{-j\phi_i(t)}\right\} \tag{A15}$$

The total intensity on the B-side is

$$I^B(t) = \sum_j^M I_j^B(t) = M\left(\varepsilon^{2\,(r)} + \varepsilon^{2\,(s)}\right) + \frac{M}{N}2\varepsilon^{(r)}\varepsilon^{(r)}\sum_i^N Re\left\{e^{-j\phi_i(t)}\right\} \tag{A16}$$

Moreover, the scattered field $E^{(s)}(t)$ can be assumed to fill uniformly the acceptance cone of the multimode fiber i.e. backscattering containing a large number of k-vectors, sufficient to cover the numerical aperture of the multimode fiber uniformly.

This leads to the consequence that both sides A and B have the same number of speckles i.e. M=N. Actually, by this assumption, the number of speckles remains the same at any location along the multimode fiber. In other words, this means that the random field distributions at both ends are connected only by a phase relation. The final result is that, indeed, the intensity at both sides is exactly the same, $I^B(t) = I^A(t)$, since the number of speckles is the same at both ends i.e. M=N:

$$I^B(t) = M\left(\varepsilon^{2\,(r)} + \varepsilon^{2\,(s)}\right) + \frac{M}{N} 2\varepsilon^{(r)}\varepsilon^{(r)} \sum_i^N Re\left\{e^{-j\phi_i(t)}\right\}$$

$$= N\left(\varepsilon^{2\,(r)} + \varepsilon^{2\,(s)}\right) + 2\varepsilon^{(r)}\varepsilon^{(r)} \sum_i^N Re\left\{e^{-j\phi_i(t)}\right\} = I^A(t) \qquad \text{(A17)}$$

This conclusion has deeper implications. If the field distributions at both ends are connected only by a phase relation it means that the intensity statistics are conserved. In other words, the intensity autocorrelation function gives the same result regardless of the location at which it is calculated along the fiber.

From the same definitions of the reference, scattered, and total fields used before (Eq. A5):

$$E_i^{(r)}(t) = \varepsilon_i^{(r)}$$

$$E_i^{(s)}(t) = \varepsilon_i^{(s)} e^{-j\phi_i(t)}$$

$$E_i(t) = E_i^{(r)}(t) + E_i^{(s)}(t) = \varepsilon_i^{(r)} + \varepsilon_i^{(s)} e^{-j\phi_i(t)}$$

The electric field autocorrelation function (ACF) of the scattered field can be calculated as:

$$G^{1\,(s)}(\tau) = \langle E^{(s)}(t) E^{*(s)}(t+\tau) \rangle = \left\langle \left[\sum_i^N \varepsilon_i^{(s)} e^{-j\phi_i(t)} \right] \left[\sum_j^N \varepsilon_j^{(s)} e^{+j\phi_j(t+\tau)} \right] \right\rangle$$

$$= \langle \sum_{i,j}^{N} \varepsilon_i^{(s)} \varepsilon_j^{(s)} e^{-j[\phi_i(t)-\phi_j(t+\tau)]} \rangle$$

$$= \langle \sum_i^N \varepsilon_i^{2\,(s)} e^{-j[\phi_i(t)-\phi_i(t+\tau)]} \; + \; \sum_{i\neq j}^N \varepsilon_i^{(s)} \varepsilon_j^{(s)} e^{-j[\phi_i(t)-\phi_j(t+\tau)]} \rangle \tag{A18}$$

If cross-interactions at different locations are forbidden, Eq. (A18) becomes:

$$G^{1\,(s)}(\tau) = \langle \sum_i^N \varepsilon_i^{2\,(s)} e^{-j[\phi_i(t)-\phi_i(t+\tau)]} \rangle \tag{A19}$$

If the amplitude of the electric fields is considered to be roughly the same at all locations i.e. $\varepsilon_i^{(s)} = \varepsilon^{(s)}$, the expression above simplifies to

$$G^{1\,(s)}(\tau) = \varepsilon^{2\,(s)} \sum_i^N \langle e^{-j[\phi_i(t)-\phi_i(t+\tau)]} \rangle \tag{A20}$$

The normalized ACF of the scattered field is therefore:

$$g^{1\,(s)}(\tau) = \frac{\langle E^{(s)}(t) E^{*(s)}(t+\tau) \rangle}{\langle E^{(s)}(t) \rangle \langle E^{(s)}(t+\tau) \rangle} = \sum_i^N \langle e^{-j[\phi_i(t)-\phi_i(t+\tau)]} \rangle \tag{A21}$$

From this expression, it can be seen that $\left| g^{1\,(s)}(\tau) \right|^2 = 1$

Similarly, for the electric field autocorrelation function of the total field:

$$G^1(\tau) = \langle E(t) E^*(t+\tau) \rangle = \langle \left[\sum_i^N \varepsilon_i^{(r)} + \varepsilon_i^{(s)} e^{-j\phi_i(t)} \right] \left[\sum_j^N \varepsilon_j^{(r)} + \varepsilon_j^{(s)} e^{+j\phi_j(t+\tau)} \right] \rangle$$

$$= \langle \sum_{i,j}^{N} \varepsilon_i^{(r)} \varepsilon_j^{(r)} + \varepsilon_i^{(r)} \varepsilon_j^{(s)} e^{+j\phi_j(t+\tau)} + \varepsilon_j^{(r)} \varepsilon_i^{(s)} e^{-j\phi_i(t)} + \varepsilon_i^{(s)} \varepsilon_j^{(s)} e^{-j[\phi_i(t)-\phi_j(t+\tau)]} \rangle$$

$$= \langle \sum_i^N \varepsilon_i^{2\,(r)} + \varepsilon_i^{(r)}\varepsilon_i^{(s)}\left[e^{-j\phi_i(t)} + e^{+j\phi_i(t+\tau)}\right] + \varepsilon_i^{2\,(s)} e^{-j[\phi_i(t)-\phi_i(t+\tau)]} \quad + \quad \sum_{i\neq j}^N \varepsilon_i^{(r)}\varepsilon_j^{(r)} +$$

$$\varepsilon_i^{(r)}\varepsilon_j^{(s)} e^{+j\phi_j(t+\tau)} + \varepsilon_j^{(r)}\varepsilon_i^{(s)} e^{-j\phi_i(t)} + \varepsilon_i^{(s)}\varepsilon_j^{(s)} e^{-j[\phi_i(t)-\phi_j(t+\tau)]}\rangle \tag{A22}$$

If cross-interactions at different locations are forbidden:

$$G^1(\tau) = \langle \sum_i^N \varepsilon_i^{2\,(r)} + \varepsilon_i^{(r)}\varepsilon_i^{(s)}\left[e^{-j\phi_i(t)} + e^{+j\phi_i(t+\tau)}\right] + \varepsilon_i^{2\,(s)} e^{-j[\phi_i(t)-\phi_i(t+\tau)]}\rangle \tag{A23}$$

If the amplitude of the electric fields is considered to be roughly the same at all locations i.e. $\varepsilon_i^{(r)} = \varepsilon^{(r)}$ and $\varepsilon_i^{(s)} = \varepsilon^{(s)}$, the expression above simplifies to:

$$G^1(\tau) = N\varepsilon^{2\,(r)} + \varepsilon^{(r)}\varepsilon^{(s)} \sum_i^N \langle e^{-j\phi_i(t)} + e^{+j\phi_i(t+\tau)}\rangle + \varepsilon^{2\,(s)} \sum_i^N \langle e^{-j[\phi_i(t)-\phi_i(t+\tau)]}\rangle$$

$$= N\varepsilon^{2\,(r)} + \varepsilon^{(r)}\varepsilon^{(s)} \sum_i^N \left[\langle e^{-j\phi_i(t)}\rangle + \langle e^{+j\phi_i(t+\tau)}\rangle\right] + \varepsilon^{2\,(s)} g^{1\,(s)}(\tau) \tag{A24}$$

Assuming the process is statistically stationary i.e. $\langle e^{-j\phi_i(t)}\rangle = \langle e^{+j\phi_i(t+\tau)}\rangle$:

$$G^1(\tau) = N\varepsilon^{2\,(r)} + 2\varepsilon^{(r)}\varepsilon^{(s)} \sum_i^N \langle e^{-j\phi_i(t)}\rangle + \varepsilon^{2\,(s)} g^{1\,(s)}(\tau) \tag{A25}$$

If the random variable ϕ_i is assumed to be uniformly distributed over all possible angles, the quantity $e^{-j\phi_i(t)}$will be uniformly distributed over the complex plane with zero average:

$$G^1(\tau) = N\varepsilon^{2\,(r)} + \varepsilon^{2\,(s)} g^{1\,(s)}(\tau) \tag{A26}$$

The intensity autocorrelation function of the total intensity is given by:

$$G^2(\tau) = \langle I(t)I(t+\tau)\rangle \quad \text{, where:} \quad I(t) = \sum_i^N \left|\varepsilon_i^{(r)} + \varepsilon_i^{(s)} e^{-j\phi_i(t)}\right|^2$$

$$= \langle \sum_{i}^{N} \left| \varepsilon_i^{(r)} + \varepsilon_i^{(s)} e^{-j\phi_i(t)} \right|^2 \sum_{i}^{N} \left| \varepsilon_i^{(r)} + \varepsilon_i^{(s)} e^{-j\phi_i(t+\tau)} \right|^2 \rangle$$

$$= \langle \sum_{i,j}^{N} \left[\varepsilon_i^{(r)} + \varepsilon_i^{(s)} e^{-j\phi_i(t)} \right] \left[\varepsilon_i^{(r)} + \varepsilon_i^{(s)} e^{+j\phi_i(t)} \right] \left[\varepsilon_j^{(r)} + \varepsilon_j^{(s)} e^{-j\phi_j(t+\tau)} \right] \left[\varepsilon_j^{(r)} + \varepsilon_j^{(s)} e^{+j\phi_j(t+\tau)} \right] \rangle$$

$$= \langle \sum_{i,j}^{N} \left(\varepsilon_i^{2\,(r)} + \varepsilon_i^{2\,(s)} + \varepsilon_i^{(r)} \varepsilon_i^{(s)} \left[e^{+j\phi_i(t)} + e^{-j\phi_i(t)} \right] \right) \left(\varepsilon_j^{2\,(r)} + \varepsilon_j^{2\,(s)} \right.$$

$$\left. + \varepsilon_j^{(r)} \varepsilon_j^{(s)} \left[e^{+j\phi_j(t+\tau)} + e^{-j\phi_j(t+\tau)} \right] \right) \rangle$$

$$= \langle \sum_{i,j}^{N} \begin{array}{c} \varepsilon_i^{2\,(r)} \varepsilon_j^{2\,(r)} + \varepsilon_i^{2\,(r)} \varepsilon_j^{2\,(s)} + 2\varepsilon_i^{2\,(r)} \varepsilon_j^{(r)} \varepsilon_j^{(s)} Re\left\{ e^{-j\phi_j(t)} \right\} \\ + \ \varepsilon_i^{2\,(s)} \varepsilon_j^{2\,(r)} + \varepsilon_i^{2\,(s)} \varepsilon_j^{2\,(s)} + 2\varepsilon_i^{2\,(s)} \varepsilon_j^{(r)} \varepsilon_j^{(s)} Re\left\{ e^{-j\phi_j(t+\tau)} \right\} \\ + \ 2\varepsilon_i^{(r)} \varepsilon_i^{(s)} \varepsilon_j^{2\,(r)} Re\left\{ e^{-j\phi_i(t)} \right\} + 2\varepsilon_i^{(r)} \varepsilon_i^{(s)} \varepsilon_j^{2\,(s)} Re\left\{ e^{-j\phi_i(t)} \right\} \\ + 2\varepsilon_i^{(r)} \varepsilon_i^{(s)} \varepsilon_j^{(r)} \varepsilon_j^{(s)} \left[Re\left\{ e^{-j[\phi_i(t) - \phi_j(t+\tau)]} \right\} + Re\left\{ e^{-j[\phi_i(t) + \phi_j(t+\tau)]} \right\} \right] \end{array} \rangle$$

$$= \langle \sum_{i}^{N} \varepsilon_i^{4\,(r)} + \varepsilon_i^{4\,(s)} + 2\varepsilon_i^{3\,(r)} \varepsilon_i^{(s)} \left[Re\left\{ e^{-j\phi_j(t)} \right\} + Re\left\{ e^{-j\phi_j(t+\tau)} \right\} \right] + 2\varepsilon_i^{(r)} \varepsilon_i^{3\,(s)} \left[Re\left\{ e^{-j\phi_j(t)} \right\} + \right.$$

$$\left. Re\left\{ e^{-j\phi_j(t+\tau)} \right\} \right] + 2\varepsilon_i^{2\,(r)} \varepsilon_i^{2\,(s)} \left[1 + Re\left\{ e^{-j[\phi_i(t) - \phi_j(t+\tau)]} \right\} + Re\left\{ e^{-j[\phi_i(t) + \phi_j(t+\tau)]} \right\} \right] +$$

$$\sum_{i \neq j}^{N} \begin{array}{c} \varepsilon_i^{2\,(r)} \varepsilon_j^{2\,(r)} + \varepsilon_i^{2\,(r)} \varepsilon_j^{2\,(s)} + 2\varepsilon_i^{2\,(r)} \varepsilon_j^{(r)} \varepsilon_j^{(s)} Re\left\{ e^{-j\phi_j(t)} \right\} \\ + \ \varepsilon_i^{2\,(s)} \varepsilon_j^{2\,(r)} + \varepsilon_i^{2\,(s)} \varepsilon_j^{2\,(s)} + 2\varepsilon_i^{2\,(s)} \varepsilon_j^{(r)} \varepsilon_j^{(s)} Re\left\{ e^{-j\phi_j(t+\tau)} \right\} \\ + \ 2\varepsilon_i^{(r)} \varepsilon_i^{(s)} \varepsilon_j^{2\,(r)} Re\left\{ e^{-j\phi_i(t)} \right\} + 2\varepsilon_i^{(r)} \varepsilon_i^{(s)} \varepsilon_j^{2\,(s)} Re\left\{ e^{-j\phi_i(t)} \right\} \\ + 2\varepsilon_i^{(r)} \varepsilon_i^{(s)} \varepsilon_j^{(r)} \varepsilon_j^{(s)} \left[Re\left\{ e^{-j[\phi_i(t) - \phi_j(t+\tau)]} \right\} + Re\left\{ e^{-j[\phi_i(t) + \phi_j(t+\tau)]} \right\} \right] \end{array} \rangle \qquad \text{(A27)}$$

If cross-interactions are forbidden, Eq. (A27) becomes:

$$G^2(\tau) = \langle \sum_i^N \varepsilon_i^{4\,(r)} + \varepsilon_i^{4\,(s)} + 2\varepsilon_i^{3\,(r)}\varepsilon_i^{(s)}\left[Re\left\{e^{-j\phi_j(t)}\right\} + Re\left\{e^{-j\phi_j(t+\tau)}\right\}\right] +$$

$$2\varepsilon_i^{(r)}\varepsilon_i^{3\,(s)}\left[Re\left\{e^{-j\phi_j(t)}\right\} + Re\left\{e^{-j\phi_j(t+\tau)}\right\}\right] + 2\varepsilon_i^{2\,(r)}\varepsilon_i^{2\,(s)}\left[1 + Re\left\{e^{-j[\phi_i(t)-\phi_j(t+\tau)]}\right\} +\right.$$

$$\left. Re\left\{e^{-j[\phi_i(t)+\phi_j(t+\tau)]}\right\}\right]\rangle \tag{A28}$$

This simplifies dramatically if the random variable ϕ_i is assumed to be uniformly distributed over all possible angles, the amplitude of the electric fields is considered to be roughly the same at all locations, and the process is statistically stationary:

$$G^2(\tau) = N\left[\varepsilon^{4\,(r)} + \varepsilon^{4\,(s)}\right]$$

$$+ 2\varepsilon^{2\,(r)}\varepsilon^{2\,(s)}\sum_i^N\left[1 + \langle Re\left\{e^{-j[\phi_i(t)-\phi_j(t+\tau)]}\right\}\rangle + \langle Re\left\{e^{-j[\phi_i(t)+\phi_j(t+\tau)]}\right\}\rangle\right]$$

$$= N\left[\varepsilon^{4\,(r)} + 2\varepsilon^{2\,(r)}\varepsilon^{2\,(s)} + \varepsilon^{4\,(s)}\right]$$

$$+ 2\varepsilon^{2\,(r)}\varepsilon^{2\,(s)}Re\left\{\sum_i^N\langle e^{-j[\phi_i(t)-\phi_j(t+\tau)]}\rangle + \sum_i^N\langle e^{-j[\phi_i(t)+\phi_j(t+\tau)]}\rangle\right\}$$

$$= N\left(\varepsilon^{2\,(r)} + \varepsilon^{2\,(s)}\right)^2 + 2\varepsilon^{2\,(r)}\varepsilon^{2\,(s)}Re\left\{\sum_i^N\langle e^{-j[\phi_i(t)-\phi_j(t+\tau)]}\rangle + \sum_i^N\langle e^{-j[\phi_i(t)+\phi_j(t+\tau)]}\rangle\right\} \tag{A29}$$

Recall the ACF of the scattered field was calculated to be:

$$g^{1\,(s)}(\tau) = \frac{\langle E_i^{(s)}(t)E_i^{*(s)}(t+\tau)\rangle}{\langle E_i^{(s)}(t)\rangle\langle E_i^{(s)}(t+\tau)\rangle} = \sum_i^N\langle e^{-j[\phi_i(t)-\phi_i(t+\tau)]}\rangle \tag{A30}$$

Since the real part of the complex exponential is symmetric (cosine) i.e. $\langle e^{-j[\phi_i(t)-\phi_j(t+\tau)]}\rangle = \langle e^{-j[\phi_i(t)=\phi_j(t+\tau)]}\rangle$:

$$G^2(\tau) = N\left(\varepsilon^{2\,(r)} + \varepsilon^{2\,(s)}\right)^2 + 4\varepsilon^{2\,(r)}\varepsilon^{2\,(s)}Re\left\{g^{1\,(s)}(\tau)\right\} \tag{A31}$$

Note: the term $\varepsilon^{4\,(s)}$implicitly contains the contribution $\left|g^{1\,(s)}(\tau)\right|^2 = 1$.

The normalized intensity autocorrelation function is:

$$g^2(\tau) = \frac{\langle I(t)I(t+\tau)\rangle}{\langle I(t)\rangle\langle I(t+\tau)\rangle} = \frac{G^2(\tau)}{\langle I(t)\rangle\langle I(t+\tau)\rangle} \tag{A32}$$

From the expression of the total intensity:

$$I(t) = \sum_i^N \left|\varepsilon_i^{(r)} + \varepsilon_i^{(s)} e^{-j\phi_i(t)}\right|^2 \tag{A33}$$

It can be seen that $\langle I(t)\rangle = \langle I(t+\tau)\rangle = N\left(\varepsilon^{2\,(r)} + \varepsilon^{2\,(s)}\right)$. Thus, the normalized ACF of the total intensity is:

$$g^2(\tau) = \frac{G^2(\tau)}{\langle I(t)\rangle\langle I(t+\tau)\rangle} = \frac{N\left(\varepsilon^{2\,(r)} + \varepsilon^{2\,(s)}\right)^2 + 4\varepsilon^{2\,(r)}\varepsilon^{2\,(s)} Re\left\{g^{1\,(s)}(\tau)\right\}}{N^2(\varepsilon^{2\,(r)} + \varepsilon^{2\,(s)})^2}$$

$$= \frac{1}{N} + \left(\frac{2\varepsilon^{(r)}\varepsilon^{(s)}}{N\left(\varepsilon^{2\,(r)}+\varepsilon^{2\,(s)}\right)}\right)^2 Re\left\{g^{1\,(s)}(\tau)\right\} \tag{A34}$$

If the reference field is defined to be proportional to the scattered field i.e. $\varepsilon^{(r)} = \alpha\varepsilon^{(s)}$, an expression of the normalized intensity ACF in terms of normalized quantities can be obtained:

$$g^2(\tau) = \frac{1}{N} + \left(\frac{2\alpha}{N(\alpha^2+1)}\right)^2 Re\left\{g^{1\,(s)}(\tau)\right\} \tag{A35}$$

From this expression it follows that $\lim_{N\to\infty} g^2(\tau) = 0$ and $\lim_{\alpha\to\infty} g^2(\tau) = \frac{1}{N}$. These conclusions are consistent with the fact that for a very large number of speckles i.e. large N, the dynamic information is screened and there is no correlation between the contributions. On the other hand, very large amplitude of the reference field ends up decreasing the contrast of the fluctuations until

they cannot be distinguished anymore and a constant value is obtained for the normalized intensity autocorrelation function.

Working out the expression above a single coefficient for the ACF can be obtained:

$$g^2(\tau) = \left(\frac{N(\alpha^2+1)^2+4\alpha^2}{[N(\alpha^2+1)]^2}\right) Re\{g^{1\,(s)}(\tau)\} \tag{A36}$$

The ACF function of the scattered field is what contains information about the correlated motion of the scattering centers and, therefore, about the properties of the suspending medium. It can be seen that the best condition for recovering $g^{1\,(s)}(\tau)$ is for a single point of illumination (N = 1), similarly to the case in which a single-mode receiver is used in DLS [34]. It can also be seen that for large N the coefficient practically does not change anymore with increasing ratio between the field amplitudes. This probes that, at the expense of a sacrifice in its amplitude, the dynamic information of the system contained in the ACF of the scattered field, $g^{1\,(s)}(\tau)$, can be recovered from the intensity autocorrelation function, $g^2(\tau)$, which is actually the experimental observable. Thus, there must be a balance between the quality of the optical signal and the quality of the electrical signal from where the optical contribution containing the dynamic information of the system under study is extracted.

On one hand, using a single, small location of coherent illumination e.g., single-mode fiber, provides the best quality in the optical signal for the calculation of the ACF since the contrast of the fluctuations is large i.e., the fluctuations represent a large variation in the overall small average amplitude. The limitation in this case is the low signal level due to the small aperture which makes it vulnerable to other sources of noise. If one increases the size of the illumination spot i.e., of the

aperture (larger fiber core, still single-mode), the optical contribution will be more significant than the inherent noise at the expense of losing some contrast in the light intensity fluctuations.

On the other hand, using multiple, independent locations of coherent illumination e.g. illuminating with a speckle field through a multimode fiber, provides an optical contribution much stronger than the intrinsic electrical noise of the detection system. The drawback in this case is that the amplitude of the ACF reduces with increasing number of illumination spots, which could compromise the accuracy of the dynamic information retrieved.

SMFs would definitely be the best option if the noise at the detection system is extremely low or if the optical contribution is strong enough to overcome the intrinsic noise. The reality is that these conditions are unlikely to be achieved and that is why the use of MMFs exhibit a better performance in terms of overcoming the electrical noise. This becomes even more evident when a temporal gate is implemented since the signals involved are weaker.

When illuminating with a speckle field through a MMF the contrast of the intensity fluctuations remains unaffected. Thus, the problem reduces to the task of isolating single scattering in order to reliably retrieve the dynamic information. If one could dynamically control both the number of spots (spatial coherence) and the spectral properties of the source (temporal coherence), for instance by tuning the spectral properties of the light source (central wavelength and bandwidth), then the quality of both the optical and the electrical signal can be optimized.

Finally, using a speckle field as the illumination gives an additional advantage. Due to the multiple, independent illumination locations that simultaneously sample the volume of observation at different spatial locations, non-ergodicity within the volume of observation can be mitigated since

a much larger range of the system's phase-space can be explored. It is worth noting that this approach could be implemented with single-mode fibers only by using a large number of them. Here, we are performing this parallel sampling by using a single optical fiber.

One could take the present derivation one step further and include the finite size of the detector in order to calculate the optimum number of speckles N [35]. Here it was assumed that the area of the detector is large enough to integrate the total intensity of the light coming out from the MMF.

APPENDIX B: NON-ERGODICITY IN LIGHT SCATTERING-BASED DYNAMIC MEASUREMENTS

In brief, non-ergodicity, that is the non-equivalence between time and ensemble averages, in the context of a DLS experiment means that the intensity correlation function (ICF) measured cannot be interpreted in terms of ensemble-averaged properties of the medium [115]. Typical examples of errors when non-ergodicity is not effectively mitigated are summarized here:

- Different samples, although similarly prepared, will contain scattering centers in different average positions and will be described by different sub-ensembles. Thus, the time-averaged ICF obtained from a single DLS measurement on a particular sample will constitute an average over a sub-ensemble of configurations. The form of this time or sub-ensemble-averaged ICF will depend on the particular sample under study.

- If one analyzes the ICF measured on a non-ergodic medium as if it was that of an ergodic medium, one would not obtain the diffusion coefficient characteristic of the particles' motions, but rather an apparent diffusion coefficient that may lead to wrong decision regarding the system's dynamics. For instance, obtaining a large diffusion constant in the presence of non-ergodicity does not imply rapid particle motions, as it would be the interpretation if ergodicity is assumed; instead, a large diffusion constant results simply from incorrect analysis of the data.

- The micro-rheological (viscoelastic) properties of the medium, estimated form the diffusion characteristics of the scattering centers, which are in turn retrieved from the ICF or equivalently the power spectral density, will be erroneous. Thus, any diagnosis pursued in terms of the mechanical properties of the medium will be compromised.

In our experiments, a direct signature of non-ergodicity would be that the shape of the power spectrum reported in Fig. 13 in the main text would be different for different integration times. The fact that the shape of the power spectrum measured is similar irrespective of the integration time used to average is a clear, quantitative indicative that the spatial averaging provided by sampling at multiple locations is indeed effective and produced a proper ensemble averaging. In other words, that non-ergodicity is effectively mitigated.

The problem is that there is not a clear and sharp threshold for when these effects start affecting the measurement. In fact, both the time scales for integration and the number of different spatial locations required to mitigate non-ergodicity largely differs depending not only on the dynamic characteristics of the sample but also on the specific mechanism implemented to work in the ergodic regime.

Table C1 below summarizes the integration time and number of measurements averaged for the proper calculation of the ICF in light scattering-based measurements (both DLS and DWS) performed on systems exhibiting non-ergodic dynamics. In these works different spatial averaging mechanisms have been implemented e.g. static light scattering (SLS) plus DLS [115], direct averaging (translational/rotational motion of the sample) [140], temporal evolution of multiple speckles [141], or non-ergodic to ergodic conversion [144].

Ref	System	Averaging time for the calculation of the ICF and some important notes
[T1]	Particles in gel	In linear mode: ten runs, each a length of **60 s**. In multiple mode: three runs, each a length of **15 min**. 37 ensembles averaged.
[T2]	Colloidal glass or crystal	Averaging time **10^3 s**. 10 different spatial locations.
[T3]	Colloidal glass or crystal	Averaging time **10^3 s**. 1000 independent speckles at the detector.
[T4]	Polymer gel (no particles)	Averaging time **10^3 s**. 100 ensembles averaged.
[T5]	Particles in gel	Averaging time **30 min**. Number of spatial locations not specified.
[T6]	Highly concentrated suspensions of PS–microgel lattices	Averaging time over multiple speckles: **50 000 s** (833 min; 13.8 hours). Averaging time, DLS: **200 000 s** (3333 min; 55.6 hours). 50 speckles per picture.
[T7]	Highly concentrated suspensions of PS–microgel lattices	Averaging time over multiple speckles: no data available (measurement not possible). Averaging time, DLS: **200 000 s** (3333 min; 55.6 hours) to resolve a characteristic time of 10^3 s. 50 speckles per picture.
[T8]	Particles in Laponite suspensions	No averaging is performed; ICF is calculated directly from 2 acquired images separated by 40 ms. 5000 speckles per picture.
[T9]	Particles in gel	Averaging time **10 000 s** (167 min; 2.8 hours). 1000 different ICF, 10 s acquisition time for each.
[T10]	Particles in Maxwellian fluid	Averaging time **18 000 s** (300 min; 5 hours). Number of speckles on the camera not specified.
[T11]	Particles in (slightly interconnected) polymer network	Averaging time **2-3 min**. Number of speckles on the camera not specified.

[T1] Joosten *et al.* Phys. Rev. A, **42**(4), pp. 2161 (1990).
[T2] Van Megen *et al.* Phys. Rev. A, **43**(10), pp. 5429 (1991).
[T3] Van Megen, et al. Phys. Rev. Lett., **67**(12), pp. 1586 (1991).
[T4] Xue, *et al.* Phys. Rev. A, **46**(10), pp. 6550 (1992).
[T5] Joosten, J., Dynamic light scattering by non-ergodic media, in *Application of Scattering Methods to the Dynamics of Polymer Systems*. Springer. p. 149-152 (1993).
[T6] Kirsch *et al.*, J. Chem. Phys., **104**(4), pp. 1758-1761 (1996).
[T7] Bartsch *et al.*, J. Chem. Phys., **106**(9), pp. 3743-3756 (1997).
[T8] Knaebel *et al.*, Europhys. Lett., **52**(1), pp. 73 (2000).
[T9] Nisato *et al.*, Phys. Rev. E, **61**(3), pp. 2879 (2000).
[T10] Galvan-Miyoshi et al., Eur. Phys. J. E, **26**(4), pp. 369-377 (2008).
[T11] Sarmiento-Gomez et al., J. Phys. Chem. B, **118**(4), pp. 1146-1158 (2014).

Table B1. Average and standard deviation of the different metrics at different stages of the surgery and their corresponding incremental time-point differences. The average and standard deviation are calculated between all the subjects included in the pilot study.

As it can be seen, the issue of non-ergodicity can seriously impact both the measurement and the interpretation of the data. The integration time can increase rapidly even if the measurement is performed at several spatial locations. Our cases, where non-stationary are to be followed as accurately as possible, the integration time must be kept as short as possible. Therefore, the only option for proper ensemble-averaging is the evaluation of the system's dynamics at multiple locations. In this regard, the parallelization of our measurement at multiple spatial locations permits having a 'preventive' mechanism to reliably retrieve dynamic information fast and over a broad range of dynamical regimes without the need of empiric corrections.

APPENDIX C: MOLECULAR ABSORPTION COEFFICIENT OF BLACK INK

Independent measurements of the absorption coefficient, μ_a, and the extinction coefficient, μ_e, of aqueous solutions of ink and light-absorbing colloids, respectively, were carried out by performing transmittance measurements using the experimental setup shown in Fig. C1. In general, $\mu_e = \mu_a + \mu_s$, where μ_s is the scattering coefficient. In the case of the aqueous solutions of black ink used in our experiments $\mu_e = \mu_a$, since the sample is practically absorbing-only (scattering-less) i.e., the composition is closer to a dye than to an ink. This was verified by the absence of a detectable power spectrum in measurements of coherence-gated DLS.

As shown in Fig. C1, the illumination was restricted to be single-mode in order to measure the attenuation along a single k-vector i.e., along a single direction, as shown in Fig. C1. From this perspective (single-direction attenuation), one can easily understand why scattering and absorption are inherently intertwined and, in general, cannot be decoupled. More specifically, from the viewpoint of a fixed detector, attenuation would be equally perceived either because the light is directed away from the direction in which the measurement is performed, as in the case of scattering; or, because the light is absorbed.

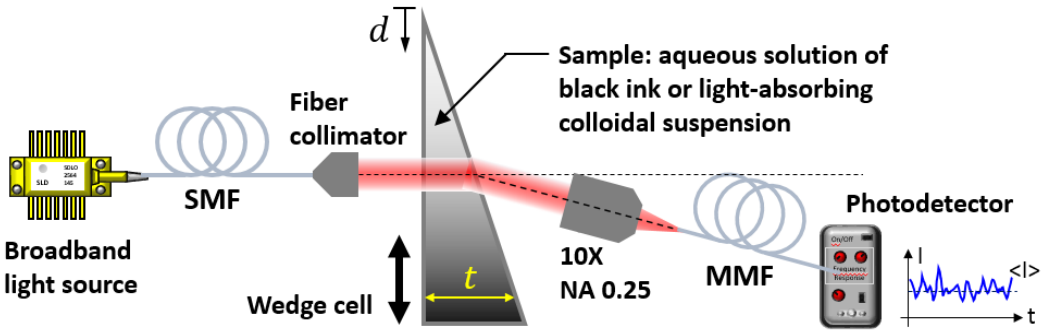

Figure C1. Schematic of the experimental setup used for the measurement of extinction coefficient of liquid samples which are in general both light-scattering and light-absorbing. The setup was constructed to measure along a single k-vector and uses a triangular (wedge) cell that allows measuring directly the extinction coefficient without having to modify the setup or replace the sample.

Ensuring a single-direction measurement allows using the formalism of the Beer-Lambert law, $I = I_0 e^{-(\mu_s+\mu_a)x}$, which predicts an exponential decay of the intensity as the light propagates in a medium with a constant extinction coefficient. Nevertheless, our goal is to actually measure the extinction coefficient.

In order to do so, one needs to be able to measure the transmitted intensity for different thicknesses, from where the value of $\mu_e = \mu_s + \mu_a$, can be extracted. This could be done, for instance, by using multiple samples consisting of slabs of different thickness which contain the same medium under study. In that case, the number of different samples required would be determined by the number of data points that are necessary to fit an exponentially decaying function with sufficient accuracy.

In our case, on the other hand, a triangular (wedge) cell was used instead, which can simply be displaced in order to adjust the thickness of the sample, as indicated in Fig. C1. In this way, a collection of data points of transmittance versus the sample's thickness can be acquired for each sample in a simple manner, from where the extinction coefficient can be extracted without having to modify the setup or use multiple samples.

Moreover, by performing measurements on samples with different μ_e, one can actually measure a more fundamental dependence of the extinction coefficient on the actual composition of the sample which is responsible for the attenuation.

For example, in the case of aqueous solutions of black ink, μ_a changes with the concentration of ink i.e., μ_a increases with the concentration of ink. Thus, one needs to also measure μ_a at different concentrations in order to stablish a more general relationship which can tell the corresponding μ_a for an arbitrary concentration of ink. This information is more fundamental since it refers to the

inherent light-absorbing properties of the absorbers i.e., ink molecules. Sometimes, such relationship is referred to as the molecular extinction function.

Fig. C2 shows the results of our measurements on aqueous solutions of black ink. Specifically, Fig. C2(a) shows the transmittance measurements for aqueous solutions of commercial-grade black ink (Royal talens Ecoline) with different concentration, as indicated, as a function of the increasing thickness of the sample. The markers indicate the experimental data points while the solid lines are the fits to the Beer-Lambert law (note the logarithmic scale in the vertical axis). Prior to the transmittance measurements, the relationship between the distance from the reference edge, d, and the thickness of the sample, t, was measured (see schematic in Fig. C1). In this way, the wedge cell was simply displaced, as indicated in the schematic, and then each position was associated to its corresponding thickness, as indicated in Fig. C2(a).

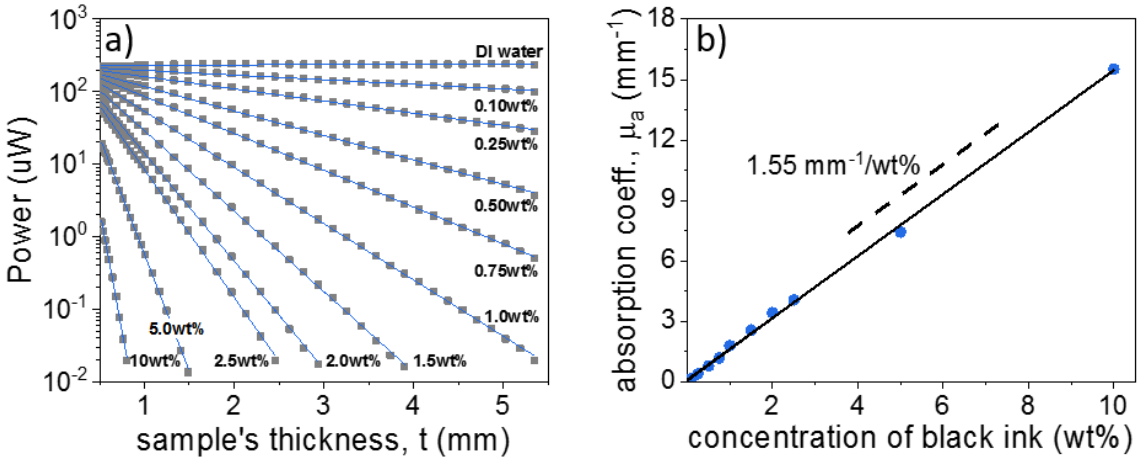

Figure C2. a) Transmittance measurements for aqueous solutions of black ink with different concentration, as indicated, as a function of the increasing thickness of the simple. The solid lines indicate the fits to the logarithmic version of the Beer-Lambert law; μ_a is encoded in the slope of the straight lines. b) Linear dependence of μ_a on the concentration of black ink and the corresponding molecular absorption coefficient.

In Fig. C2(a) μ_a for each concentration is encoded in the slope of the straight line (note the logarithmic scale in the vertical axis). Fig. C2(b) summarizes the value of μ_a as a function of the concentration of black ink (slopes in Fig. C2(a)). It was found that the dependence of μ_a on the concentration i.e., the molecular absorption function, is linear with the concentration of ink (Fig. C2(b)). Therefore, a molecular absorption coefficient can be defined as $\mu_a^{(mol)}(C) = 1.55\ mm^{-1}/wt\%$, as indicated. The meaning of this value is that, for instance, at a concentration of ink of C=10wt% the characteristic attenuation length is only of $l_a = \mu_a^{-1} \approx 60\ \mu m$.

Finally, we would like to note some of the practical complications that arise in a measurement of the absorption coefficient and, more generally, of the molecular absorption function. We thoroughly reviewed the literature and noted, for instance, that both samples from different brands of commercial inks and even samples from different batches of the same brand can have significantly different values. Normally, only samples from the same batch have almost identical optical properties. Also, in spite of this large brand-to-brand and batch-to-batch variations observed for the specific extinction and absorption coefficients, very similar values have been obtained for the ratio between the molecular absorption and extinction coefficients, $\mu_a^{(mol)}/\mu_{ext}^{(mol)}$, and for the albedo. Finally, we also noticed that the optical properties of diluted ink remain stable for a long time as opposed to those with higher concentrations. In Ref. [155], for instance, $\mu_a^{(mol)}$ of a diluted sample of Higgins ink was monitored for about one year without observing significant variations.

In order to put our results in perspective, we compared them with those from a number of different reports. The table below shows the molecular absorption coefficient, $\mu_a^{(mol)}$, which was either explicitly reported or estimated from the experimental results in the corresponding reference.

Ref	Ink	Commercial brand	λ_0 (nm)	$\mu_a^{(mol)}$ (mm^{-1}/wt%)	Notes
[156]	Black	Regal 1	594	7.72 ± 0.05	
		Regal 2		34.5 ± 1.0	
		Higgins		12.3 ± 0.2	
[54]	Black	Royal talens Ecoline	827	---	μ_a = 50.47 and 0.94 mm^{-1} are reported for two different concentrations. The actual values of these concentrations is not given. But, this is the same ink that we used.
[55]	Black	Unknown	850	0.072	Unknown black ink. The reported volume fractions of ink were taken to be the same as the weight concentration for the estimation.
[56]	Green	Royal talens Ecoline	680	0.15	This is an ink from the same brand that we used. For red light, the absorption coefficient should be comparable to that of black ink i.e., green ink is a strong absorber at these wavelengths.
[157]	Black	Unknown	570-590	2.5	The plot reported is actually very similar to our measurements – the original black ink is simply diluted with DI water (original black ink is taken explicitly as 100% concentration).
[155]	Black	Higgins 1	632.8	3.7	Values estimated from the data points in a plot.
		Higgins 2		4.5	
		Pelikan 1		5.1	
		Pelikan 2		5.2	
		Pelikan 3		4.9	
		Rotring 1		7.8	
		Rotring 2		9.6	
		Koh l Noor		5.0	
		Staedtler		8.2	
[158]	Black	Higgins	633	3.84	The measurements were carried out on samples at different labs where different characterization techniques were used for the measurement of the optical properties.
				3.55	
				3.93	
				3.75	
				3.86	
			687	3.4	
Us	Black	Royal talens Ecoline	670	1.55	Measured experimentally in the wedge configuration.

Table C1. Average and standard deviation of the different metrics at different stages of the surgery and their corresponding incremental time-point differences. The average and standard deviation are calculated between all the subjects included in the pilot study

APPENDIX D: BRIEF REVIEW OF DIFFUSING WAVE SPECTROCOPY

In a typical DWS experiment [3, 14], one obtains quantitative dynamic information on the basis of the theory of diffusion of light. Specifically, this implies knowing the probability density of the distribution of photon paths through the medium, $p(s)$, and the associated parameters such as the photon transport mean free path, l^*, and the photon absorption length, l_a.

A number of limitations arise in applying this procedure:

- Many dynamic systems of practical interest, although they are multiply scattering, are not optically diffusive. These media, in general, cannot be characterized by a DWS treatment [159, 160] (although some corrections to the diffusive models may exist for special cases). In this context, it has also been shown that sometimes complete diffusion is not fully achieved even for longer paths [161, 162]. Naturally, in geometries involving light transport in the low-order multiple-scattering regime, such as backscattering, the diffusion approximation often breaks down and the outcome is quite sensitive to the shape of $p(s)$ [159].

- l^* cannot always be calculated and an independent measurement is required, often subject of specific boundary conditions. In this regard, the boundary conditions become critical to describe scattering processes close to boundaries or interfaces. In those cases, the interpretation of a DWS-like signal is far from trivial because the diffusion process in proximity to a boundary introduces new length scales due to the re-injection of light, which is forced to travel along new paths inside the scattering medium [163]. This dependence on the boundary can be removed by performing so-called ‘monostatic’ and ‘bistatic’ optical path length spectroscopic measurements [164].

- The dynamics measured is in fact averaged over a range of time scales (the detected signal is integrated over all photon path lengths).

Some of the above-listed limitations can be overcome by time-gating techniques i.e., pulsed-DWS [165], where the dependence on $p(s)$ is removed (by selectively isolating a single path length) while providing means to simultaneously measure l^*. This approach can be refined by alternating measurements of the system's dynamics and the background signals for *in situ* background subtraction [166-168].

More recent DWS-based implementations target a different problem: non-ergodicity and the validity of so-called Siegert relation. These newer approaches, i.e., interferometric near-infrared spectroscopy, utilize interferometric schemes that allow measuring not only l^* and intensity correlations [169], but also field correlations directly [170].

Some of these implementations have also attempted to remove some of the geometry dependence of traditional DWS, by operating in the so-called "reflectance" mode, both interferometrically [171, 172], and non-interferometrically [173], which allows injecting and collecting light on the same side of the complex medium, albeit at different locations.

Unlike the above-listed limitations e.g., the dependence on $p(s)$, which are pertinent to situations involving multiple scattering, these latter issues (ergodicity and Siegert relation) actually pertain to any light scattering-based dynamic measurement.

Nevertheless, it is important to note that in the newer DWS-based implementations both ergodicity and the validity of the Siegert relation can be compromised due to the measurement being

performed over photon paths that are static or slowly-varying during the time of the measurement, which is inherent to the time-gating required to remove the dependence on $p(s)$.

As discussed in detail in the Appendix B, in other scenarios, where time gating is not involved, ergodicity can be easily forced by means of different approaches including, for instance, the combination of static and dynamic light scattering [115], direct averaging by translating or rotating the sample [140], temporal evolution of multiple speckles [141], or the implementation of a non-ergodic to ergodic conversion [144].

Finally, we would like to note that in some recent reports DWS has been claimed to be 'geometry independent', in the context of implementations where the source of light and the detector are located on the same side of a complex medium, thus making it look like a reflection-like situation.

However, it is worth clarifying that, in the context of light scattering-based dynamic measurements, the term 'geometry independence' refers to the capability to perform the measurements at any angle, with containers of arbitrary shape, and irrespective of the scattering characteristics of the sample, among others. In this respect DWS cannot be 'geometry independent' because one has to ensure that the light scattering regime can be appropriately described as a photon diffusion (which allows assuming the Gaussian shape of on $p(s)$ and, consequently, an analytical form of the correlation function; see Section 1.3).

It is well known that in certain important geometries, such as backscattering, the diffusion approximation breaks down, and interpretation of the autocorrelation function measured in a DWS experiment is complicated since a more complete understanding of the crossover from ballistic to

diffusive propagation is required [165, 174]. Furthermore, it has been demonstrated that sometimes the transition to a complete diffusion regime is not fully achieved even for long paths [161].

If the source and the detector happen to be on the same side of a material, as in the so-called "reflectance-mode" interferometric DWS [171, 172], this does not necessarily mean that the measurement is operated in reflection! Moreover, the outcome of such measurement depends on the geometry i.e., the separation distance between the locations of light injection and collection, as well as the scattering properties of the medium and, therefore, the conditions for the diffusion approximation must be enforced at all times.

In the references [171, 172] it can be clearly seen that the light is launched at one location, propagates inside the medium, and then it is collected at a different spatial location. For light that is multiply scattered, this is actually representative for a *transmission* rather than *reflection* geometry. A technically unambiguous terminology refers to the measurement as being *"monostatic"*, when the point source and point detector are collocated, and *"bi-static"* when the emitter and receiver are physically separated (see for instance [164]).

APPENDIX E: OTHER ATTEMPTS FOR MEASURING BLOOD COAGULABILITY

In laser speckle rheology (LSR) [153, 175, 176], more recently named as optical thromboelastography (OTEG) [154], a sample of blood (of about 100 μL, typically) is collected and prepared with anticoagulants prior to the measurement. Later, at the beginning of the measurement, the anticoagulation reversed (by the addition of kaolin) and backscattered speckle patterns are recorded on a CCD camera [153]. This technique has been demonstrated *in vivo* in animal models where both vessel occlusion and micro-injuries are purposely induced to promote clot formation [176].

The idea is the following: during coagulation, platelet-fibrin clot formation progressively restricts the mean square displacement (MSD) of the scattering centers (RBCs) thus increasing the characteristic decorrelation time due to the reduction of speckle fluctuations i.e., the recorded frames exhibit lower variability as coagulation progresses due to the constrained motion in the sample. Correlation analysis of the speckle frames provides the characteristic decorrelation time, which can be used as a direct indicator of the coagulation process [153], and allows estimating both the MSD and the viscoelastic modulus of blood. The increase in the decorrelation time also reflects in the increased magnitude of the elastic moduli, which relates to a 'solid-like' behavior and is sometimes used as figure of merit to retrieve an evolution curve similar to than obtained from TEG [154]. In some cases, additional statistical descriptors such as the variance of the fluctuations (speckle contrast) are also complementary used [175].

Blood coagulation assessment based on the continuous measurement of the complex electrical impedance is well-stablished since long time ago [177-179], and it is widely used to evaluate the quality of stored blood. In this approach, similarly to the above-described techniques, a sample of whole blood is collected and coagulation is activated. During coagulation, the electrical impedance

(magnitude and phase angle) of the sample is continuously measured between two electrodes that are in contact with the blood. In this measurement, the magnitude of the blood's impedance is typically correlated to the concentration of fibrin (the larger the concentration the larger the impedance magnitude).

More recently, these technique has been incorporated into more sophisticated measurement platforms using micro-fluidic channels and high-tech electronics that allow for an accurate monitoring of the coagulation process in more compact platforms where one requires micro-litter-sized samples and multiple samples can be evaluated simultaneously [180, 181]. By following the magnitude of the impedance at certain relevant frequency one can retrieve a curve similar to that of TEG where the value of the impedance magnitude eventually saturates when the clot has been completely formed [180, 181].

In a recent report, a big step was made as compared to the above-described techniques and all the gold standards: the measurement of blood coagulation under relevant flow conditions that can resemble those from micro-vasculature in vivo [182]. This allows having a more realistic picture of the coagulation process since it allows incorporating effects of hemodynamic forces (pressure, flow and shear stress), platelet function, and related cellular interactions that are known to significantly impact whole blood thrombosis in the living vasculature.

In this approach, blood is flowed through a microfluidic device that, by means of cascaded regions of accelerating, constant, and deceleration flows, mimics a network arteriolar vessels, and permits evaluating blood clotting within small sample volumes under pathophysiological flow. In this case, coagulation is mechanically induced through platelet aggregation due to the fluid shear gradients

produced in the circuit. This technique can be integrated directly into vascular access lines and blood-contacting medical devices for the real-time, but *ex vivo* coagulation monitoring. Experimentally, the rise of pressure in the channels over time is recorded as occlusion progresses. The formation of clots is verified by fluorescence microscopy images in which platelets and fibrin were tagged with different fluorophores.

Indeed, these approaches operate on whole blood, however, all of them are also based on end-point measurements. This requires a sample to be collected and sometimes prepared to induce coagulation under specific conditions and, after the measurement, the sample has to be disposed. Consequently, these approaches cannot provide real-time information hemostatic potential of the blood.

Other techniques, recently reported, include, for instance, a miniaturized acoustic resonator that uses a zinc oxide film bulk to measure viscoelasticity changes with coagulation [183]. Wang et al integrated acoustic radiation force and optical imaging to measure plasma elasticity changes during clot formation [184]. Lakshmanan et al used a quartz crystal microbalance to study the changes in viscoelasticity during clot formation [185]. All of these techniques, however, were developed as intermittent, *in vitro* measures. Another notable development is a continuous assay for the measurement of tissue factor procoagulant activity on intact cells, but for clinical laboratory usage [186]. A continuous droplet microfluidic system was developed to measure thrombin generation but was not tested in the real-time clinical setting [187]. Sakota et al have used the observation that RBCs aggregate locally in the presence of fibrinogen to suggest that clotting status during ECLS can be assessed by using optical aggregometry of RBCs [188]. The technique as described, however, requires pulsatile flow, which is not typically present in either ECLS or CPB.

A critical limitation to the above mentioned newer technologies is also their inability to monitor continuously and dynamically the of blood coagulation abnormalities especially in the setting of rapidly changing coagulation status.

PUBLICATIONS AND PRESENTATIONS

Refereed Journal Papers

[10] Guzman-Sepulveda, J. R., Wu R., and Dogariu, Continuous optical measurement of internal dynamics in drying colloidal droplets (under review in *Journal of Colloid and Interface Science*).

[9] Guzman-Sepulveda, J. R., Wu, R., Kalra, A. P., Aminpour, M., Tuszynski, J.A., and Dogariu, A. Tubulin polarizability in aqueous suspensions, *ACS Omeg*a, 4(5), 9144-9149 (2019).

[8] Guzman-Sepulveda, J. R. and Dogariu, A. Probing complex dynamics with spatiotemporal coherence-gated DLS, *Applied Optics*, 58 (13), D76-D90, (2019).

[7] Guzman-Sepulveda, J. R. and Dogariu, A., Multimode interference dynamic light scattering, *Optics Letters*, 43(17), 4232-4235 (2018).

[6] Guzman-Sepulveda, J. R., Deng, J., Fang, J., and Dogariu, A. (2017) Characterizing viscoelastic modulations in biopolymer hydrogels by coherence-gated light scattering. *The Journal of Physical Chemistry B*, 121(39), 9234–9238.

[5] Guzman-Sepulveda, J. R., Argueta-Morales, R., DeCampli, W. M., & Dogariu, A. (2017). Real-time intraoperative monitoring of blood coagulability via coherence-gated light scattering. *Nature Biomedical Engineering*, 1, 0028.

[4] Guzman-Sepulveda, J.R., Deng, J., Fang, J., & Dogariu, A. (2016). In-situ characterization of structural dynamics in swelling hydrogels. *Soft Matter,* 12, 5986-5994.

[3] Guzman-Sepulveda, J. R., Amin, S., Lewis, E. N., & Dogariu, A. (2015). Full characterization of colloidal dynamics at low-Péclet numbers. *Langmuir*, 31 (38), pp 10351–10357.

[2] Liang, W., Guzman-Sepulveda, J. R., He, S., Dogariu, A., & Fang, J. Y. (2015). Microrheology and Release Behaviors of Self-Assembled Steroid Hydrogels. *Journal of Materials Science and Chemical Engineering*, 3(8), 6.

[1] Guzman-Sepulveda, J. R., Douglass, K. M., Amin, S., Lewis, N. E., & Dogariu, A. (2015). Passive optical mapping of structural evolution in complex fluids. *RSC Advances*, 5(7), 5357-5362.

Conference Proceedings

[C14] J. R. Guzman-Sepulveda, R. Wu, and A. Dogariu. Continuous Optical Measurement of Dynamic Colloidal Droplets. Applications & Technology section in Conference on Lasers and Electro-Optics (CLEO), OSA Technical Digest (Optical Society of America, 2019), paper ATh4K.3.

[C13] C. H. Acevedo, J. R. Guzman-Sepulveda, and A. Dogariu. Brownian Dynamics Controlled by Phase Gradients. QELS Fundamental Science section in Conference on Lasers and Electro-Optics (CLEO), OSA Technical Digest (Optical Society of America, 2019), paper FTh1C.8.

[C12] J. R. Guzman-Sepulveda and A. Dogariu (2018, May). Multimode interference dynamic light scattering. Applications & Technology section in CLEO (pp. AF1M.5).

[C11] J. R. Guzman-Sepulveda, W. M. DeCampli, and A. Dogariu (2018, Apr). Intraoperative Assessment of Blood Coagulability using Coherence-gated Light Scattering. Clinical and Translational Biophotonics section in the OSA Biophotonics Congress: Biomedical Optics (pp. CW4B.5).

[C10] Guzman-Sepulveda, J.R., Deng, J., Fang, J., & Dogariu, A. (2017, Oct). Light scattering characterization of viscoelastic modulations in biopolymer hydrogels. In IEEE Photonics Conference (pp. TuE2.1).

[C9] Guzman-Sepulveda, J.R., Deng, J., Fang, J., & Dogariu, A. (2017, May). Continuous characterization of viscoelasticity-modulated biopolymer hydrogels. In CLEO: Applications and Technology (pp. ATu1A-5). Optical Society of America.

[C8] Guzman-Sepulveda, J. R., Argueta-Morales, R., Pourmoghadam, K., DeCampli, W. M., and Dogariu, A (2016, Jun). Optical rheology of blood during cardiovascular surgery. In CLEO: Science and Innovations. Optical Society of America.

[C7] Argueta-Morales, R., Guzman-Sepulveda, J. R., DeCampli, W. M., and Dogariu, A (2016, Jun). Pilot study of optical rheology as a method to assess coagulation status in pediatric patients before and after undergoing cardiopulmonary bypass for open heart surgery – Progress towards continuous real-time coagulation monitoring. In 5th International Conference on Engineering Frontiers in Pediatric and Congenital Heart Disease.

[C6] Guzman-Sepulveda, J. R. and Dogariu, A. (2016, Mar). Continuous monitoring of structural dynamics in polymer assemblies. In APS March Meeting. American Physics Society.

[C5] Guzman-Sepulveda, J. R. and Dogariu, A. (2016, Mar). Continuous characterization of structural dynamics in complex systems. In FLAVS Annual Joint Symposium and Exhibition Symposium. American Vacuum Society – Science and Technology of Materials, Interfaces, and Processing.

[C4] Guzman-Sepulveda, J. R., Hurtado-Gimenez, D. E., and Dogariu, A. (2015, October). Measurement of Diffusive Transport at Liquid-Liquid Interfaces. In Frontiers in Optics (pp. FW5E-3). Optical Society of America.

[C3] Guzman-Sepulveda, J. R., Hurtado-Gimenez, D. E., and Dogariu, A. (2015, Aug). Measuring local diffusion properties in colloidal systems. In International Conference in Speckle Metrology.

[C2] Guzman-Sepulveda, J. R. and Dogariu, A. (2015, May). Real-time Full Characterization of Colloidal Dynamics. In CLEO: Science and Innovations (pp. AF1J2). Optical Society of America.

[C1] Guzman-Sepulveda, J. R., Falusi, C. K., Douglass, K. M., and Dogariu, A. (2014, August). Active and passive measurements of local properties of complex fluids using low-coherence dynamic light scattering. In Biological and Pharmaceutical Complex Fluids II: Novel Trends in Characterizing Interactions, Microstructure and Rheology. ECI Conference Series.

REFERENCES

1. B. J. Berne and R. Pecora, *Dynamic light scattering: with applications to chemistry, biology, and physics* (Courier Corporation, 1976).
2. E. R. Pike, "The theory of light scattering," in *NATO Advanced Study Institutes Series (Series B: Physics, v.3). Photon correlation and light beating spectroscopy.*, H. Z. Cummins and E. R. Pike, eds. (Springer Science & Business Media, New York, 1974), pp. 9-40.
3. D. J. Pine, D. A. Weitz, P. M. Chaikin, and E. Herbolzheimer, "Diffusing wave spectroscopy," Physical Review Letters **60**, 1134-1137 (1988).
4. P. N. Pusey, "The study of Brownian motion by intensity fluctuation spectroscopy," Philosophical Transactions of the Royal Society of London A: Mathematical, Physical and Engineering Sciences **293**, 429-439 (1979).
5. G. L. Paul and P. N. Pusey, "Observation of a long-time tail in Brownian motion," Journal of Physics A: Mathematical and General **14**, 3301-3327 (1981).
6. H. Z. Cummins and P. N. Pusey, "Dynamics of macromolecular motion," in *NATO Advanced Study Institutes Series (Series B: Physics, v.23). Photon correlation spectroscopy and velocimetry.*, H. Z. Cummins and P. N. Pusey, eds. (Springer Science & Business Media, New York, 1977), pp. 164-199.
7. H. C. v. d. Hulst, *Light scattering by small particles* (Dover Publications Inc., 1981).
8. P. M. Chaikin and T. C. Lubensky, *Principles of condensed matter physics* (Cambridge university press, 2000).
9. D. E. Koppel, "Analysis of macromolecular polydispersity in intensity correlation spectroscopy: the method of cumulants," The Journal of Chemical Physics **57**, 4814-4820 (1972).
10. B. J. Frisken, "Revisiting the method of cumulants for the analysis of dynamic light-scattering data," Applied Optics **40**, 4087-4091 (2001).

11. P. A. Hassan and S. K. Kulshreshtha, "Modification to the cumulant analysis of polydispersity in quasielastic light scattering data," Journal of colloid and interface science **300**, 744-748 (2006).
12. S. W. Provencher, "CONTIN: a general purpose constrained regularization program for inverting noisy linear algebraic and integral equations," Computer Physics Communications **27**, 229-242 (1982).
13. S. W. Provencher, "A constrained regularization method for inverting data represented by linear algebraic or integral equations," Computer Physics Communications **27**, 213-227 (1982).
14. G. Maret and P. E. Wolf, "Multiple light scattering from disordered media. The effect of Brownian motion of scatterers," Zeitschrift für Physik B Condensed Matter **65**, 409-413 (1987).
15. D. A. Weitz and D. J. Pine, "Diffusing wave spectroscopy," in *Dynamic Light Scattering*, W. Brown, ed. (Oxford University Press, New York, 1993), pp. 652-720.
16. D. J. Pine, D. A. Weitz, G. Maret, P. E. Wolf, H. Herbolzheimer, and P. W. Chaikin, "Dynamical correlations of multiply scattered light," in *Scattering and localization of classical waves in random media*, P. Sheng, ed. (World Scientific, Singapore, 1990), pp. 312-372.
17. D. A. Weitz, J. X. Zhu, D. J. Durian, H. Gang, and D. J. Pine, "Diffusing-wave spectroscopy: The technique and some applications," Physica Scripta **T49**, 610-621 (1993).
18. G. Maret, "Diffusing-wave spectroscopy," Current opinion in colloid & interface science **2**, 251-257 (1997).
19. T. G. Mason, H. Gang, and D. A. Weitz, "Diffusing-wave-spectroscopy measurements of viscoelasticity of complex fluids," JOSA A **14**, 139-149 (1997).
20. J. L. Harden and V. Viasnoff, "Recent advances in DWS-based micro-rheology," Current opinion in colloid & interface science **6**, 438-445 (2001).

21. I. Meglinski and V. V. Tuchin, "Diffusing Wave Spectroscopy: Application for Blood Diagnostics," in *Handbook of Coherent-Domain Optical Methods: Biomedical Diagnostics, Environmental Monitoring, and Materials Science*, V. V. Tuchin, ed. (Springer, New York, 2013), pp. 149-166.
22. Z. Fahimi, F. Aangenendt, P. Voudouris, J. Mattson, and H. M. Wyss, "Diffusing-wave spectroscopy in a standard dynamic light scattering setup," arXiv preprint arXiv:1509.03454 (2015).
23. J. W. Goodman, *Speckle phenomena in optics: theory and applications* (Roberts and Company Publishers, 2007).
24. H. Cummins and H. Swinney, "Light beating spectroscopy," in *Progress in Optics*, E. Wolf, ed. (North-Holland, Amsterdam, The Netherlands, 1970), pp. 146-150.
25. E. Jakeman, "Photon correlation," in *Photon correlation and light beating spectroscopy* (Springer, 1974), pp. 75-149.
26. J. W. Goodman, "Some fundamental properties of speckle*," JOSA **66**, 1145-1150 (1976).
27. J. Schmitt, "Array detection for speckle reduction in optical coherence microscopy," Physics in Medicine and Biology **42**, 1427 (1997).
28. D. Gloge, "Optical power flow in multimode fibers," Bell System Technical Journal **51**, 1767-1783 (1972).
29. R. Olshansky, "Mode coupling effects in graded-index optical fibers," Applied optics **14**, 935-945 (1975).
30. D. Gloge and E. Marcatili, "Multimode Theory of Graded-Core Fibers," Bell System Technical Journal **52**, 1563-1578 (1973).
31. S. Fan and J. M. Kahn, "Principal modes in multimode waveguides," Optics letters **30**, 135-137 (2005).
32. M. B. Shemirani, W. Mao, R. A. Panicker, and J. M. Kahn, "Principal modes in graded-index multimode fiber in presence of spatial-and polarization-mode coupling," Journal of lightwave technology **27**, 1248-1261 (2009).

33. K.-P. Ho and J. M. Kahn, "Statistics of group delays in multimode fiber with strong mode coupling," Lightwave Technology, Journal of **29**, 3119-3128 (2011).

34. J. Rička, "Dynamic light scattering with single-mode and multimode receivers," Applied Optics **32**, 2860-2875 (1993).

35. M. Salem and A. Dogariu, "Optical heterodyne detection of random electromagnetic beams," Journal of Modern Optics **51**, 2305-2313 (2004).

36. J. Guzman-Sepulveda, R. Argueta-Morales, W. DeCampli, and A. Dogariu, "Real-time intraoperative monitoring of blood coagulability via coherence-gated light scattering," Nature Biomedical Engineering **1**, 0028 (2017).

37. S. Torquato, *Random heterogeneous materials: microstructure and macroscopic properties* (Springer Science & Business Media, 2013), Vol. 16.

38. I. Sohn, R. Rajagopalan, and A. Dogariu, "Spatially resolved microrheology through a liquid/liquid interface," Journal of colloid and interface science **269**, 503-513 (2004).

39. J. R. Guzman-Sepulveda, K. M. Douglass, S. Amin, N. E. Lewis, and A. Dogariu, "Passive optical mapping of structural evolution in complex fluids," RSC Advances **5**, 5357-5362 (2015).

40. T. G. Mason, "Estimating the viscoelastic moduli of complex fluids using the generalized Stokes–Einstein equation," Rheologica Acta **39**, 371-378 (2000).

41. T. G. Mason and D. Weitz, "Optical measurements of frequency-dependent linear viscoelastic moduli of complex fluids," Physical review letters **74**, 1250 (1995).

42. A. Maggs, "Micro-bead mechanics with actin filaments," Physical Review E **57**, 2091 (1998).

43. F. MacKintosh and C. Schmidt, "Microrheology," Current opinion in colloid & interface science **4**, 300-307 (1999).

44. J. Guzman-Sepulveda, J. Deng, J. Fang, and A. Dogariu, "In-situ characterization of structural dynamics in swelling hydrogels," Soft Matter **12**, 5986-5994 (2016).

45. G. Popescu and A. Dogariu, "Dynamic light scattering in localized coherence volumes," Optics letters **26**, 551-553 (2001).
46. G. Popescu and A. Dogariu, "Scattering of low coherence radiation and applications," The European Physical Journal-Applied Physics **32**, 73-93 (2005).
47. H. Wiese and D. Horn, "Single-mode fibers in fiber-optic quasielastic light scattering: A study of the dynamics of concentrated latex dispersions," The Journal of chemical physics **94**, 6429-6443 (1991).
48. F. Stieber and W. Richtering, "Fiber-optic-dynamic-light-scattering and two-color-cross-correlation studies of turbid, concentrated, sterically stabilized polystyrene latex," Langmuir **11**, 4724-4727 (1995).
49. S. L. Elliott, R. J. Butera, L. H. Hanus, and N. J. Wagner, "Fundamentals of aggregation in concentrated dispersions: Fiber-optic quasielastic light scattering and linear viscoelastic measurements," Faraday discussions **123**, 369-383 (2003).
50. H. Wiese and D. Horn, "Fiber-Optic Quasielastic Light Scattering in Concentrated Latex Dispersions: The Performance of Single-Mode vs. Multimode Fibers," Berichte der Bunsengesellschaft für physikalische Chemie **96**, 1818-1828 (1992).
51. P. N. Pusey and W. Van Megen, "Dynamic light scattering by non-ergodic media," Physica A: Statistical Mechanics and its Applications **157**, 705-741 (1989).
52. W. Liang, J. R. Guzman-Sepulveda, S. He, A. Dogariu, and J. Y. Fang, "Microrheology and Release Behaviors of Self-Assembled Steroid Hydrogels," ournal of Materials Science and Chemical Engineering **3**, 6-15 (2015).
53. M. Bellour, M. Skouri, J. P. Munch, and P. Hébraud, "Brownian motion of particles embedded in a solution of giant micelles," The European Physical Journal E **8**, 431-436 (2002).

54. A. L. Petoukhova, W. Steenbergen, T. G. van Leeuwen, and F. F. de Mul, "Effects of absorption on coherence domain path length resolved dynamic light scattering in the diffuse regime," Applied physics letters **81**, 595-597 (2002).

55. H. Xia, H. Li, B. Yang, K. Ishii, and T. Iwai, "Measurement of optical constants for dense media by low-coherence dynamic light scattering," Optics Communications **281**, 1331-1336 (2008).

56. N. Bosschaart, M. C. Aalders, D. J. Faber, J. J. Weda, M. J. van Gemert, and T. G. van Leeuwen, "Quantitative measurements of absorption spectra in scattering media by low-coherence spectroscopy," Optics letters **34**, 3746-3748 (2009).

57. J. R. Guzman-Sepulveda, S. Amin, E. N. Lewis, and A. Dogariu, "Full characterization of colloidal dynamics at low-Péclet numbers," Langmuir **31**, 10351–10357 (2015).

58. M. Mason and W. Weaver, "The settling of small particles in a fluid," Physical Review **23**, 412-426 (1924).

59. E. Guazzelli and J. Hinch, "Fluctuations and instability in sedimentation," Annual review of fluid mechanics **43**, 97-116 (2011).

60. R. Piazza, S. Buzzaccaro, and E. Secchi, "The unbearable heaviness of colloids: facts, surprises, and puzzles in sedimentation," Journal of Physics: Condensed Matter **24**, 284109 (2012).

61. R. Piazza, "Settled and unsettled issues in particle settling," Reports on Progress in Physics **77**, 056602 (2014).

62. R. Govindarajan and K. C. Sahu, "Instabilities in viscosity-stratified flow," Annual review of fluid mechanics **46**, 331-353 (2014).

63. A. Doostmohammadi and A. Ardekani, "Suspension of solid particles in a density stratified fluid," Physics of Fluids **27**, 023302 (2015).

64. D. W. Rankin, "CRC handbook of chemistry and physics, edited by David R. Lide," (Taylor & Francis, 2009).

65. A. Vailati and M. Giglio, "Nonequilibrium fluctuations in time-dependent diffusion processes," Physical Review E **58**, 4361 (1998).
66. C. Kittel, *Introduction to solid state physics* (Wiley New York, 1976), Vol. 8.
67. D. Brutin, B. Sobac, B. Loquet, and J. Sampol, "Pattern formation in drying drops of blood," Journal of fluid mechanics **667**, 85-95 (2011).
68. R. Chen, L. Zhang, D. Zang, and W. Shen, "Blood drop patterns: Formation and applications," Advances in colloid and interface science **231**, 1-14 (2016).
69. T.-S. Wong, T.-H. Chen, X. Shen, and C.-M. Ho, "Nanochromatography driven by the coffee ring effect," Analytical chemistry **83**, 1871-1873 (2011).
70. J. Zhang, Z. Sun, and B. Yang, "Self-assembly of photonic crystals from polymer colloids," Current Opinion in Colloid & Interface Science **14**, 103-114 (2009).
71. S. Khapli, I. Rianasari, T. Blanton, J. Weston, R. Gilardetti, R. Neiva, N. Tovar, P. G. Coelho, and R. Jagannathan, "Fabrication of hierarchically porous materials and nanowires through coffee ring effect," ACS applied materials & interfaces **6**, 20643-20653 (2014).
72. S. Khapli, I. Rianasari, S. Sharma, T. Blanton, and R. Jagannathan, "Fabrication of hierarchically structured porous films of metal oxides and carbonates through coffee ring effect," Materials Today: Proceedings **3**, 362-368 (2016).
73. P. Keblinski, J. A. Eastman, and D. G. Cahill, "Nanofluids for thermal transport," Materials today **8**, 36-44 (2005).
74. R. Hernandez-Perez, Z. H. Fan, and J. L. Garcia-Cordero, "Evaporation-driven bioassays in suspended droplets," Analytical chemistry **88**, 7312-7317 (2016).
75. J. L. Garcia-Cordero and Z. H. Fan, "Sessile droplets for chemical and biological assays," Lab on a Chip **17**, 2150-2166 (2017).

76. D. K. Devendiran and V. A. Amirtham, "A review on preparation, characterization, properties and applications of nanofluids," Renewable and Sustainable Energy Reviews **60**, 21-40 (2016).
77. X. Zhong, A. Crivoi, and F. Duan, "Sessile nanofluid droplet drying," Advances in colloid and interface science **217**, 13-30 (2015).
78. P. Dak, A. Ebrahimi, and M. A. Alam, "Non-faradaic impedance characterization of an evaporating droplet for microfluidic and biosensing applications," Lab on a Chip **14**, 2469-2479 (2014).
79. Y. Serfert, J. Schröder, A. Mescher, J. Laackmann, M. Shaikh, K. Rätzke, V. Gaukel, H. Schuchmann, P. Walzel, and H.-U. Moritz, "Characterization of the spray drying behaviour of emulsions containing oil droplets with a structured interface," Journal of microencapsulation **30**, 325-334 (2013).
80. B. Al Zaitone and A. Lamprecht, "Single droplet drying step characterization in microsphere preparation," Colloids and Surfaces B: Biointerfaces **105**, 328-334 (2013).
81. F. Girard, M. l. Antoni, and K. Sefiane, "Infrared thermography investigation of an evaporating sessile water droplet on heated substrates," Langmuir **26**, 4576-4580 (2010).
82. P. Innocenzi, L. Malfatti, S. Costacurta, T. Kidchob, M. Piccinini, and A. Marcelli, "Evaporation of ethanol and ethanol− water mixtures studied by time-resolved infrared spectroscopy," The Journal of Physical Chemistry A **112**, 6512-6516 (2008).
83. R. J. Hopkins and J. P. Reid, "Evaporation of ethanol/water droplets: examining the temporal evolution of droplet size, composition and temperature," The Journal of Physical Chemistry A **109**, 7923-7931 (2005).
84. J. D. Smith, C. D. Cappa, W. S. Drisdell, R. C. Cohen, and R. J. Saykally, "Raman thermometry measurements of free evaporation from liquid water droplets," Journal of the American Chemical Society **128**, 12892-12898 (2006).

85. V. Deprédurand, P. Miron, A. Labergue, M. Wolff, G. Castanet, and F. Lemoine, "A temperature-sensitive tracer suitable for two-colour laser-induced fluorescence thermometry applied to evaporating fuel droplets," Measurement Science and Technology **19**, 105403 (2008).
86. P. Strizhak, R. Volkov, G. Castanet, F. Lemoine, O. Rybdylova, and S. Sazhin, "Heating and evaporation of suspended water droplets: Experimental studies and modelling," International Journal of Heat and Mass Transfer **127**, 92-106 (2018).
87. A. Bilsky, Y. A. Lozhkin, and D. Markovich, "Interferometric technique for measurement of droplet diameter," Thermophysics and aeromechanics **18**, 1 (2011).
88. Y. Wu, C. Crua, H. Li, S. Saengkaew, L. Mädler, X. Wu, and G. Gréhan, "Simultaneous measurement of monocomponent droplet temperature/refractive index, size and evaporation rate with phase rainbow refractometry," Journal of Quantitative Spectroscopy and Radiative Transfer **214**, 146-157 (2018).
89. L. Perrin, G. Castanet, and F. Lemoine, "Characterization of the evaporation of interacting droplets using combined optical techniques," Experiments in Fluids **56**, 29 (2015).
90. N. Liu, W. Wang, J. Han, M. Zhang, P. Angeli, C. Wu, and J. Gong, "A PIV investigation of the effect of disperse phase fraction on the turbulence characteristics of liquid–liquid mixing in a stirred tank," Chemical Engineering Science **152**, 528-546 (2016).
91. E. Y. Stepanov, V. Maslov, and D. Zakharov, "A stereo PIV system for measuring the velocity vector in complex gas flows," Measurement Techniques **52**, 626-631 (2009).
92. H. Bodiguel and J. Leng, "Imaging the drying of a colloidal suspension," Soft Matter **6**, 5451-5460 (2010).
93. H. Bodiguel and J. Leng, "Imaging the drying of a colloidal suspension: Velocity field," Chemical Engineering and Processing: Process Intensification **68**, 60-63 (2013).

94. I. Ghaeli, Z. Hosseinidoust, H. Zolfagharnasab, and F. Jorge Monteiro, "A New Label-Free Technique for Analysing Evaporation Induced Self-Assembly of Viral Nanoparticles Based on Enhanced Dark-Field Optical Imaging," Nanomaterials **8**, 1 (2017).
95. H. Fan and A. Striolo, "Nanoparticle effects on the water-oil interfacial tension," Physical Review E **86**, 051610 (2012).
96. C. N. Kaplan and L. Mahadevan, "Evaporation-driven ring and film deposition from colloidal droplets," Journal of Fluid Mechanics **781**(2015).
97. R. G. Larson, "Transport and deposition patterns in drying sessile droplets," AIChE Journal **60**, 1538-1571 (2014).
98. J. R. Moffat, "Experimental investigation into the evaporating behaviour of pure and nanofluid droplets," (2011).
99. A. Munshi, V. Singh, M. Kumar, and J. Singh, "Effect of nanoparticle size on sessile droplet contact angle," Journal of Applied Physics **103**, 084315 (2008).
100. L. P. Faucheux and A. J. Libchaber, "Confined brownian motion," Physical Review E **49**, 5158 (1994).
101. L. Lobry and N. Ostrowsky, "Diffusion of Brownian particles trapped between two walls: Theory and dynamic-light-scattering measurements," Physical Review B **53**, 12050 (1996).
102. B. Lin, J. Yu, and S. A. Rice, "Direct measurements of constrained Brownian motion of an isolated sphere between two walls," Physical Review E **62**, 3909 (2000).
103. J. R. Guzman-Sepulveda, S. Amin, E. N. Lewis, and A. Dogariu, "Full Characterization of Colloidal Dynamics at Low Péclet Numbers," Langmuir **31**, 10351-10357 (2015).
104. C. Nguyen, F. Desgranges, G. Roy, N. Galanis, T. Maré, S. Boucher, and H. A. Mintsa, "Temperature and particle-size dependent viscosity data for water-based nanofluids–hysteresis phenomenon," International Journal of Heat and Fluid Flow **28**, 1492-1506 (2007).

105. B. Wang, L. Zhou, and X. Peng, "Viscosity, thermal diffusivity and Prandtl number of nanoparticle suspensions," Progress in Natural Science **14**, 922-926 (2004).

106. H. Chen, Y. Ding, Y. He, and C. Tan, "Rheological behaviour of ethylene glycol based titania nanofluids," Chemical physics letters **444**, 333-337 (2007).

107. P. K. Namburu, D. K. Das, K. M. Tanguturi, and R. S. Vajjha, "Numerical study of turbulent flow and heat transfer characteristics of nanofluids considering variable properties," International Journal of Thermal Sciences **48**, 290-302 (2009).

108. J. Joanny and P.-G. De Gennes, "A model for contact angle hysteresis," The journal of chemical physics **81**, 552-562 (1984).

109. G. Batchelor, "Sedimentation in a dilute dispersion of spheres," Journal of fluid mechanics **52**, 245-268 (1972).

110. G. Batchelor, "Brownian diffusion of particles with hydrodynamic interaction," Journal of Fluid Mechanics **74**, 1-29 (1976).

111. B. Felderhof, "Diffusion of interacting Brownian particles," Journal of Physics A: Mathematical and General **11**, 929 (1978).

112. P. Pusey, "The dynamics of interacting Brownian particles," Journal of Physics A: Mathematical and General **8**, 1433 (1975).

113. M. Watzlawek and G. Nägele, "Sedimentation of strongly and weakly charged colloidal particles: Prediction of fractional density dependence," Journal of colloid and interface science **214**, 170-179 (1999).

114. D. Brutin, *Droplet wetting and evaporation: from pure to complex fluids* (Academic Press, 2015).

115. P. Pusey and W. Van Megen, "Dynamic light scattering by non-ergodic media," Physica A: Statistical Mechanics and its Applications **157**, 705-741 (1989).

116. J. Bergenholtz, M. Fuchs, and T. Voigtmann, "Colloidal gelation and non-ergodicity transitions," Journal of Physics: Condensed Matter **12**, 6575 (2000).

117. J. Bergenholtz and M. Fuchs, "Nonergodicity transitions in colloidal suspensions with attractive interactions," Physical Review E **59**, 5706 (1999).

118. W. Härtl, "Colloidal glasses," Current opinion in colloid & interface science **6**, 479-483 (2001).

119. L. Cipelletti and L. Ramos, "Slow dynamics in glasses, gels and foams," Current opinion in colloid & interface science **7**, 228-234 (2002).

120. K. A. Dawson, "The glass paradigm for colloidal glasses, gels, and other arrested states driven by attractive interactions," Current opinion in colloid & interface science **7**, 218-227 (2002).

121. H. Tanaka, J. Meunier, and D. Bonn, "Nonergodic states of charged colloidal suspensions: repulsive and attractive glasses and gels," Physical Review E **69**, 031404 (2004).

122. V. Trappe and P. Sandkühler, "Colloidal gels—low-density disordered solid-like states," Current opinion in colloid & interface science **8**, 494-500 (2004).

123. A. G. Cherstvy, A. V. Chechkin, and R. Metzler, "Anomalous diffusion and ergodicity breaking in heterogeneous diffusion processes," New Journal of Physics **15**, 083039 (2013).

124. A. G. Cherstvy, A. V. Chechkin, and R. Metzler, "Particle invasion, survival, and non-ergodicity in 2D diffusion processes with space-dependent diffusivity," Soft Matter **10**, 1591-1601 (2014).

125. A. G. Cherstvy and R. Metzler, "Nonergodicity, fluctuations, and criticality in heterogeneous diffusion processes," Physical Review E **90**, 012134 (2014).

126. J.-H. Jeon, A. V. Chechkin, and R. Metzler, "Scaled Brownian motion: a paradoxical process with a time dependent diffusivity for the description of anomalous diffusion," Physical Chemistry Chemical Physics **16**, 15811-15817 (2014).

127. P. Massignan, C. Manzo, J. Torreno-Pina, M. García-Parajo, M. Lewenstein, and G. Lapeyre Jr, "Nonergodic subdiffusion from Brownian motion in an inhomogeneous medium," Physical review letters **112**, 150603 (2014).

128. R. Metzler, J.-H. Jeon, A. G. Cherstvy, and E. Barkai, "Anomalous diffusion models and their properties: non-stationarity, non-ergodicity, and ageing at the centenary of single particle tracking," Physical Chemistry Chemical Physics **16**, 24128-24164 (2014).

129. A. G. Cherstvy and R. Metzler, "Ergodicity breaking and particle spreading in noisy heterogeneous diffusion processes," The Journal of chemical physics **142**, 144105 (2015).

130. A. G. Cherstvy and R. Metzler, "Ergodicity breaking, ageing, and confinement in generalized diffusion processes with position and time dependent diffusivity," Journal of Statistical Mechanics: Theory and Experiment **2015**, P05010 (2015).

131. I. M. Tolić-Nørrelykke, E.-L. Munteanu, G. Thon, L. Oddershede, and K. Berg-Sørensen, "Anomalous diffusion in living yeast cells," Physical Review Letters **93**, 078102 (2004).

132. L. Deng, X. Trepat, J. P. Butler, E. Millet, K. G. Morgan, D. A. Weitz, and J. J. Fredberg, "Fast and slow dynamics of the cytoskeleton," Nature materials **5**, 636-640 (2006).

133. I. Golding and E. C. Cox, "Physical nature of bacterial cytoplasm," Physical review letters **96**, 098102 (2006).

134. I. Bronstein, Y. Israel, E. Kepten, S. Mai, Y. Shav-Tal, E. Barkai, and Y. Garini, "Transient anomalous diffusion of telomeres in the nucleus of mammalian cells," Physical review letters **103**, 018102 (2009).

135. J.-H. Jeon, V. Tejedor, S. Burov, E. Barkai, C. Selhuber-Unkel, K. Berg-Sørensen, L. Oddershede, and R. Metzler, "In vivo anomalous diffusion and weak ergodicity breaking of lipid granules," Physical review letters **106**, 048103 (2011).

136. A. V. Weigel, B. Simon, M. M. Tamkun, and D. Krapf, "Ergodic and nonergodic processes coexist in the plasma membrane as observed by single-molecule tracking," Proceedings of the National Academy of Sciences **108**, 6438-6443 (2011).

137. F. Höfling and T. Franosch, "Anomalous transport in the crowded world of biological cells," Reports on Progress in Physics **76**, 046602 (2013).

138. S. A. Tabei, S. Burov, H. Y. Kim, A. Kuznetsov, T. Huynh, J. Jureller, L. H. Philipson, A. R. Dinner, and N. F. Scherer, "Intracellular transport of insulin granules is a subordinated random walk," Proceedings of the National Academy of Sciences **110**, 4911-4916 (2013).

139. C. Manzo, J. A. Torreno-Pina, P. Massignan, G. J. Lapeyre Jr, M. Lewenstein, and M. F. G. Parajo, "Weak ergodicity breaking of receptor motion in living cells stemming from random diffusivity," Physical Review X **5**, 011021 (2015).

140. J.-Z. Xue, D. Pine, S. Milner, X.-l. Wu, and P. Chaikin, "Nonergodicity and light scattering from polymer gels," Physical Review A **46**, 6550 (1992).

141. S. Kirsch, V. Frenz, W. Schärtl, E. Bartsch, and H. Sillescu, "Multispeckle autocorrelation spectroscopy and its application to the investigation of ultraslow dynamical processes," The Journal of chemical physics **104**, 1758-1761 (1996).

142. E. Bartsch, V. Frenz, J. Baschnagel, W. Schärtl, and H. Sillescu, "The glass transition dynamics of polymer micronetwork colloids. A mode coupling analysis," The Journal of chemical physics **106**, 3743-3756 (1997).

143. A. Knaebel, M. Bellour, J.-P. Munch, V. Viasnoff, F. Lequeux, and J. Harden, "Aging behavior of laponite clay particle suspensions," EPL (Europhysics Letters) **52**, 73 (2000).

144. F. Scheffold, S. Skipetrov, S. Romer, and P. Schurtenberger, "Diffusing-wave spectroscopy of nonergodic media," Physical Review E **63**, 061404 (2001).

145. J. Guzman-Sepulveda, J. Deng, J. Fang, and A. Dogariu, "In-situ characterization of structural dynamics in swelling hydrogels," Soft Matter **12**, 5986-5994 (2016).

146. W. Liang, J. Guzman-Sepulveda, S. He, A. Dogariu, and J. Fang, "Microrheology and release behaviors of self-assembled steroid hydrogels," Journal of Materials Science and Chemical Engineering **3**, 6 (2015).

147. J. Guzman-Sepulveda, J. Deng, J. Fang, and A. Dogariu, "Characterizing Viscoelastic Modulations in Biopolymer Hydrogels by Coherence-Gated Light Scattering," The Journal of Physical Chemistry B **121**, 9234-9238 (2017).

148. A. Gutowska, J. Seok Bark, I. Chan Kwon, Y. Han Bae, Y. Cha, and S. Wan Kim, "Squeezing hydrogels for controlled oral drug delivery," J. Controlled Release **48**, 141-148 (1997).

149. M. Falamarzian and J. Varshosaz, "The Effect of Structural Changes on Swelling Kinetics of Polybasic/ Hydrophobic pH-Sensitive Hydrogels," Drug Dev. Ind. Pharm. **24**, 667-669 (1998).

150. H. J. Dalton, R. Reeder, P. Garcia-Filion, R. Holubkov, R. A. Berg, A. Zuppa, F. W. Moler, T. Shanley, M. M. Pollack, and C. Newth, "Factors associated with bleeding and thrombosis in children receiving extracorporeal membrane oxygenation," American journal of respiratory and critical care medicine **196**, 762-771 (2017).

151. S. M. Hastings, D. N. Ku, S. Wagoner, K. O. Maher, and S. Deshpande, "Sources of circuit thrombosis in pediatric extracorporeal membrane oxygenation," Asaio Journal **63**, 86-92 (2017).

152. J. R. Neal, E. Quintana, R. B. Pike, J. D. Hoyer, L. D. Joyce, and G. Schears, "Using daily plasma-free hemoglobin levels for diagnosis of critical pump thrombus in patients undergoing ECMO or VAD support," The journal of extra-corporeal technology **47**, 103 (2015).

153. M. M. Tripathi, Z. Hajjarian, E. M. Van Cott, and S. K. Nadkarni, "Assessing blood coagulation status with laser speckle rheology," Biomedical optics express **5**, 817-831 (2014).

154. Z. Hajjarian, M. M. Tripathi, and S. K. Nadkarni, "Optical Thromboelastography to evaluate whole blood coagulation," Journal of biophotonics **8**, 372-381 (2015).

155. P. Di Ninni, F. Martelli, and G. Zaccanti, "The use of India ink in tissue-simulating phantoms," Optics express **18**, 26854-26865 (2010).

156. S. J. Madsen, M. S. Patterson, and B. C. Wilson, "The use of India ink as an optical absorber in tissue-simulating phantoms," Physics in medicine and biology **37**, 985 (1992).

157. Z. Guo, S. Hu, and L. V. Wang, "Calibration-free absolute quantification of optical absorption coefficients using acoustic spectra in 3D photoacoustic microscopy of biological tissue," Optics letters **35**, 2067-2069 (2010).

158. L. Spinelli, M. Botwicz, N. Zolek, M. Kacprzak, D. Milej, P. Sawosz, A. Liebert, U. Weigel, T. Durduran, and F. Foschum, "Determination of reference values for optical properties of liquid phantoms based on Intralipid and India ink," Biomedical optics express **5**, 2037-2053 (2014).

159. G. Popescu and A. Dogariu, "Dynamic light scattering in subdiffusive regimes," Applied optics **40**, 4215-4221 (2001).

160. K. Yoo, F. Liu, and R. Alfano, "When does the diffusion approximation fail to describe photon transport in random media?," Physical review letters **64**, 2647 (1990).

161. K. K. Bizheva, A. M. Siegel, and D. A. Boas, "Path-length-resolved dynamic light scattering in highly scattering random media: The transition to diffusing wave spectroscopy," Physical Review E **58**, 7664 (1998).

162. M. F. Clapper, J. S. Collura, D. Harrison, and M. R. Fisch, "Transition from diffusing to dynamic light scattering in solutions of monodisperse polystyrene spheres," Physical Review E **59**, 3631 (1999).

163. G. Popescu, C. Mujat, and A. Dogariu, "Evidence of scattering anisotropy effects on boundary conditions of the diffusion equation," Physical Review E **61**, 4523 (2000).

164. K. M. Douglass and A. Dogariu, "Measuring diffusion coefficients independently of boundary conditions," Optics letters **34**, 3379-3381 (2009).

165. A. Yodh, P. Kaplan, and D. Pine, "Pulsed diffusing-wave spectroscopy: High resolution through nonlinear optical gating," Physical review B **42**, 4744 (1990).

166. J.-M. Tualle, E. Tinet, and S. Avrillier, "A new and easy way to perform time-resolved measurements of the light scattered by a turbid medium," Optics communications **189**, 211-220 (2001).

167. J.-M. Tualle, H. L. Nghiem, C. Schäfauer, P. Berthaud, E. Tinet, D. Ettori, and S. Avrillier, "Time-resolved measurements from speckle interferometry," Optics letters **30**, 50-52 (2005).

168. J.-M. Tualle, H. L. Nghiem, M. Cheikh, D. Ettori, E. Tinet, and S. Avrillier, "Time-resolved diffusing wave spectroscopy beyond 300 transport mean free paths," JOSA A **23**, 1452-1457 (2006).

169. D. Borycki, O. Kholiqov, S. P. Chong, and V. J. Srinivasan, "Interferometric Near-Infrared Spectroscopy (iNIRS) for determination of optical and dynamical properties of turbid media," Optics express **24**, 329-354 (2016).

170. D. Borycki, O. Kholiqov, and V. J. Srinivasan, "Interferometric near-infrared spectroscopy directly quantifies optical field dynamics in turbid media," Optica **3**, 1471-1476 (2016).

171. D. Borycki, O. Kholiqov, and V. J. Srinivasan, "Reflectance-mode interferometric near-infrared spectroscopy quantifies brain absorption, scattering, and blood flow index in vivo," Optics letters **42**, 591-594 (2017).

172. W. Zhou, O. Kholiqov, S. P. Chong, and V. J. Srinivasan, "Highly parallel, interferometric diffusing wave spectroscopy for monitoring cerebral blood flow dynamics," Optica **5**, 518-527 (2018).

173. J. Sutin, B. Zimmerman, D. Tyulmankov, D. Tamborini, K. C. Wu, J. Selb, A. Gulinatti, I. Rech, A. Tosi, and D. A. Boas, "Time-domain diffuse correlation spectroscopy," Optica **3**, 1006-1013 (2016).

174. F. MacKintosh and S. John, "Diffusing-wave spectroscopy and multiple scattering of light in correlated random media," Physical Review B **40**, 2383 (1989).

175. Y. Piederriere, J. Cariou, Y. Guern, G. Le Brun, B. Le Jeune, J. Lotrian, and J. Franc, "Evaluation of blood plasma coagulation dynamics by speckle analysis," Journal of biomedical optics **9**, 408-412 (2004).

176. V. Kalchenko, A. Brill, M. Bayewitch, I. Fine, V. Zharov, E. Galanzha, V. Tuchin, and A. Harmelin, "In vivo dynamic light scattering imaging of blood coagulation," Journal of biomedical optics **12**, 052002-052002-052004 (2007).

177. R. L. Rosenthal and C. W. Tobias, "Measurement of the electric resistance of human blood; use in coagulation studies and cell volume determinations," J. Lab. Clin. Med **33**, 1110-1122 (1948).

178. A. Ur, "Changes in the electrical impedance of blood during coagulation," Nature **226**, 269-270 (1970).

179. A. Ur, "Determination of blood coagulation using impedance measurements," Biomedical engineering **5**, 342 (1970).

180. H. Berney and J. O'Riordan, "Impedance measurement monitors blood coagulation," Analog Dialogue **42**, 42-08 (2008).

181. K. F. Lei, K.-H. Chen, P.-H. Tsui, and N.-M. Tsang, "Real-time electrical impedimetric monitoring of blood coagulation process under temperature and hematocrit variations conducted in a microfluidic chip," PloS one **8**, e76243 (2013).

182. A. Jain, A. Graveline, A. Waterhouse, A. Vernet, R. Flaumenhaft, and D. E. Ingber, "A shear gradient-activated microfluidic device for automated monitoring of whole blood haemostasis and platelet function," Nature communications **7**(2016).

183. D. Chen, Z. Zhang, J. Ma, and W. Wang, "ZnO film bulk acoustic resonator for the kinetics study of human blood coagulation," Sensors **17**, 1015 (2017).

184. C. W. Wang, M. J. Perez, B. P. Helmke, F. Viola, and M. B. Lawrence, "Integration of acoustic radiation force and optical imaging for blood plasma clot stiffness measurement," PloS one **10**, e0128799 (2015).

185. R. S. Lakshmanan, V. Efremov, J. S. O'Donnell, and A. J. Killard, "Measurement of the viscoelastic properties of blood plasma clot formation in response to tissue factor concentration-dependent activation," Analytical and bioanalytical chemistry **408**, 6581-6588 (2016).

186. J. A. Caldwell, J. G. Dickhout, A. A. Al-Hashimi, and R. C. Austin, "Development of a continuous assay for the measurement of tissue factor procoagulant activity on intact cells," Laboratory Investigation **90**, 953 (2010).

187. J. Yu, D. Tao, E. X. Ng, C. L. Drum, A. Q. Liu, and C.-H. Chen, "Real-time measurement of thrombin generation using continuous droplet microfluidics," Biomicrofluidics **8**, 052108 (2014).

188. D. Sakota, R. Kosaka, M. Nishida, and O. Maruyama, "Optical aggregometry of red blood cells associated with the blood-clotting reaction in extracorporeal circulation support," Journal of Artificial Organs **19**, 241-248 (2016).